CHARACTERISTICS AND APPLICATIONS OF AIR-COUPLED MICROMACHINED ULTRASONIC TRANSDUCERS

BY

ANDREW GRAHAM BASHFORD

Submitted for a Ph.D in Engineering
University of Warwick
October 1993 -September 1997

Submitted: March 1998

TEXT BOUND CLOSE TO THE SPINE IN THE ORIGINAL THESIS

TABLE OF CONTENTS PAGE NO.

Summary

This thesis describes the characteristics of a micromachined air-coupled ultrasonic capacitance transducer, using backplates made from chemical etching, ion-beam and laser machining in copper, steel, aluminium and silicon. A series of backplates were produced with micromachined holes on the surface of different depths, diameters and pitch. The resultant characteristics were found to be consistent with previous work. Peak pressure field variations of the capacitance transducers were measured by scanning a detector throughout the radiated field in both air and water. The resulting field compared favourably to a theoretically-generated peak pressure field variation for a plane piston (a FORTRAN program was written which convolved the simulated motion of the membrane with an impulse response for the transducer). Experimental and theoretical peak pressure field variations were measured for an annulus and zoneplate apertures with single and toneburst driving signals. In all cases the experimental field agreed well with the computed theoretical field in air and water. Additionally, with the increase in bandwidth when operated in water, the transducers were used for a pulse-echo C-scan of an artificial defect. Furthermore, the transducers were used to determine the elastic constants in air for glass-epoxy, ceramic and paper card, where the results for glass-epoxy were in good agreement for the values obtained using immersion technique. The transducers were modified by use of a Mica membrane for high temperature use, and were successfully used to monitor the burnout rate of the polymer binder from an injection moulded ceramic.

Declaration

The work presented in this thesis was the work of the author, although specialist equipment was used in other laboratories of the University of Bordeaux, France and UMIST).

A.G. Bashford 26th March 1998.

Acknowledgement

I would like thank Prof. D.A. Hutchins for his excellent supervision, encouragement and giving me the opportunity to travel to such wonderful places!. Also, I would like to thank Lawerence Scudder, Duncan Billson, Bill Wright and David Schindel for sharing their extensive knowledge, guidance and companionship throughout my Ph.D.

I would also like to thank to the staff of the Engineering Department for their time and help when needed, especially Frank Courtney for his guidance on chemical etching photolithography, Viola Kading for her guidance in polishing the backplates. Also, Steve Wallice and Dave Robinson and all the technicians in the INRG workshop who manufactured the transducer casings and components.

Finally, I would like to thank Mum, Dad, Samantha, James and Laura for their support, and Edward, Helen, Kevin, Cristina and Rebekah for their friendship and encouragement.

List of Figures

Chapter 1

Chapter 2

.Chapter 3

Chapter 4

Chapter 5

Chapter 6

Chapter 7

CHAPTER 1

INTRODUCTION

1.1 Introduction

Sound is a sensation detected by our ears, and is often produced from structures which are vibrating. As the material vibrates it sets the medium surrounding it (i.e. air) into oscillation and causes the sound wave to travel outwards. On reaching the ear, the ear-drums vibrate thus reproducing the oscillations of the source. Sound may be divided into many categories, two of which are noise and musical notes [1]. Noise is produced when the motion of the body is irregular, whereas a musical note is produced when a vibrating body performs a type of motion which is regularly repeated. Typically, the human ear can detect sound from 40Hz to about 20kHz, and above this upper limit the sound is not audible and becomes ultrasonic. In addition to being used for communication, sound has been used by animals for a long time for navigation, location, and to disable prey and predators [2]. The same techniques have been adopted by scientist for a range of applications including using SONAR for locating objects [3], and ultrasound for medical [4] and non-destructive imaging applications (e.g. thickness and defect detection) [5].

1.2 Types of sound waves

When sound propagates through a medium, the particles of the medium vibrate in directions which are characteristics of the propagating wave. Sound can travel through isotropic solids, liquid and gases, at frequencies given by:

$$f = \frac{c}{\lambda} \tag{1.1}$$

where f is the frequency (Hz), c is the velocity of sound in the medium, and λ is the wavelength.

There are several types of sound waves [6,7]. If the particles vibrate in the same direction as the wave, then the wave is said to be longitudinal or compressional. Longitudinal waves can be supported in solids, liquids and gases. A diagram of the mechanism of a longitudinal wave is shown in Figure 1.1. For propagation in a solid, the velocity of a longitudinal wave c_L is a dependent on the material properties, and is given by:

$$c_L = \sqrt{\frac{E(1-\sigma)}{\rho(1+\sigma)(1-2\sigma)}} \tag{1.2}$$

where E is Young's modulus, σ is Poisson's ratio and ρ is the density.

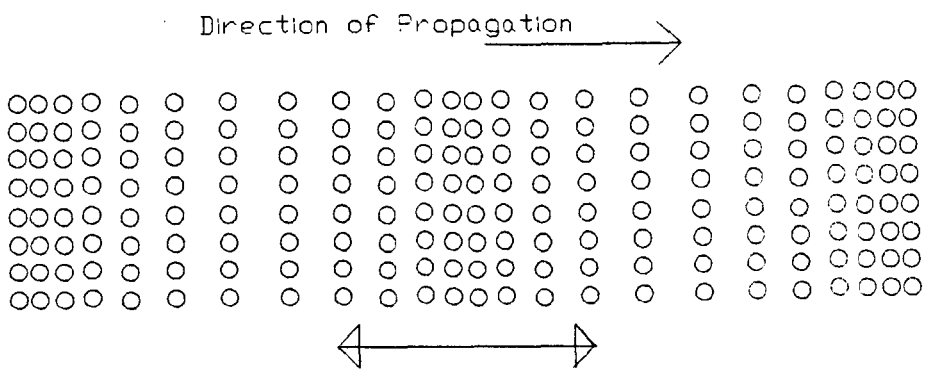

Figure 1.1. Diagram of the mechanism of a longitudinal wave.

When the motion of the particles is perpendicular to the direction of the wave, then the wave is known as a shear wave. Only solid materials and a few viscous liquids can support a shear wave, and a diagram of the mechanism is shown in Figure 1.2. The velocity of a shear wave in a solid c_S is given by:

$$c_S = \sqrt{\frac{E}{2\rho(1+\sigma)}} \tag{1.3}$$

Again, E is Young's modulus, σ is Poisson's ratio and ρ is the density. The two velocities are linked together by:

$$c_S = c_L \sqrt{\frac{1-3\sigma}{2(1-\sigma)}} \tag{1.4}$$

Other modes of vibration exists, such as Rayleigh (or surface) waves [8], where the particles move in an elliptical motion on the surface of the material and the motion becomes more circular and the amplitude decreases as the depth increases. Additionally, Lamb (or plate) surface waves exist [9] when the two surfaces of a plate are close together for propagation of a pure surface wave to occur. Surface waves are very complex and are outside the scope of the thesis to or use.

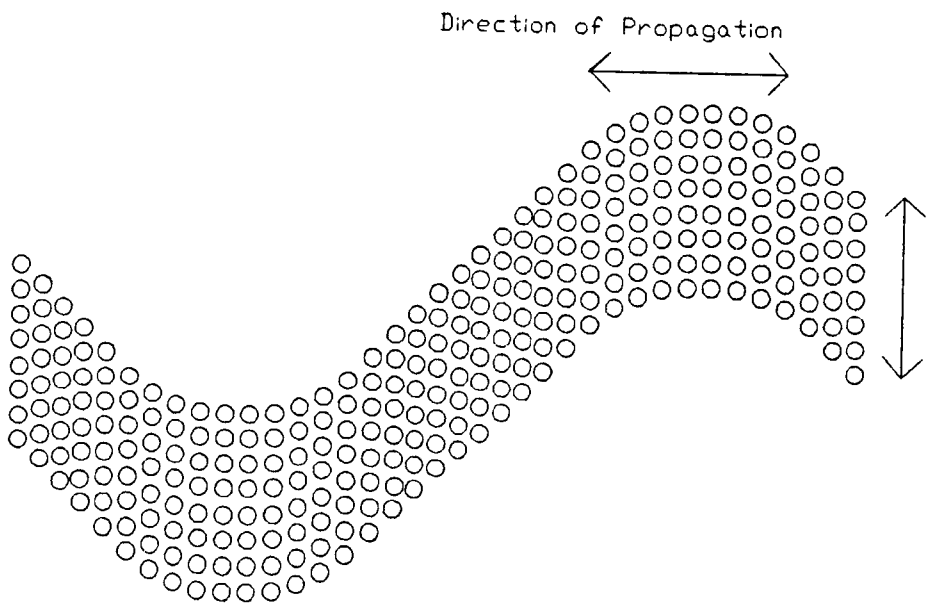

Figure 1.2. Diagram of the mechanism of a shear wave.

1.3 Wave propagation in a medium

When a sound wave meets a boundary between two materials, some of the acoustic energy will be transmitted across the boundary and the rest will be reflected. The amount of energy transmitted through the boundary is dependent on the difference of the acoustic impedance of the material either side of the boundary. The acoustic impedance Z is given by:

$$Z=\rho\ C \qquad (1.5)$$

where ρ is the density and C is the acoustic velocity in the material. The transmission coefficient (T) (i.e. the amount of energy transmitted through the boundary) is dependent on the impedance of the two materials (i.e. Z_1 and Z_2) and is given by:

$$T = \frac{4Z_1Z_2}{(Z_1+Z_2)^2} \qquad (1.6)$$

Similarly, the reflection coefficient (R) is given by:

$$R=\left(\frac{Z_1-Z_2}{Z_1+Z_2}\right)^2 \qquad (1.7)$$

Typically, when a sound wave in one medium meets a boundary of a second medium of different impedance the direction of propagation is affected [6-8,10]. If the wave is travelling at an angle α to the normal in medium 1, through the boundary, the wave is refracted due to a change in the propagation velocity. The waves travels through the second medium at an angle β to the normal, as shown in Figure 1.3. The relationship between the angle and the velocity is known as Snell's law and is given by:

$$\frac{\sin\alpha}{\sin\beta} = \frac{C_1}{C_2} \tag{1.8}$$

where C_1 and C_2 are the velocities in medium 1 and 2 respectively.

1.4 Attenuation of sound waves

When an acoustic wave travels through a medium it loses energy. The attenuation is dependent on the microstructure of the medium, temperature and pressure. In the case of propagation in a gas, the absorption is due to two basic mechanisms: classical absorption and relaxation losses [11,12]. Typically, classical losses are when the acoustic energy is transferred to heat by viscosity and thermal conductivity, and relaxation losses are when the transitional energy is redistributed into the rotational and vibrational energy states. Attenuation is typically denoted by α and is measured in decibels, using the ratio of acoustic powers or amplitude. Attenuation is defined as:

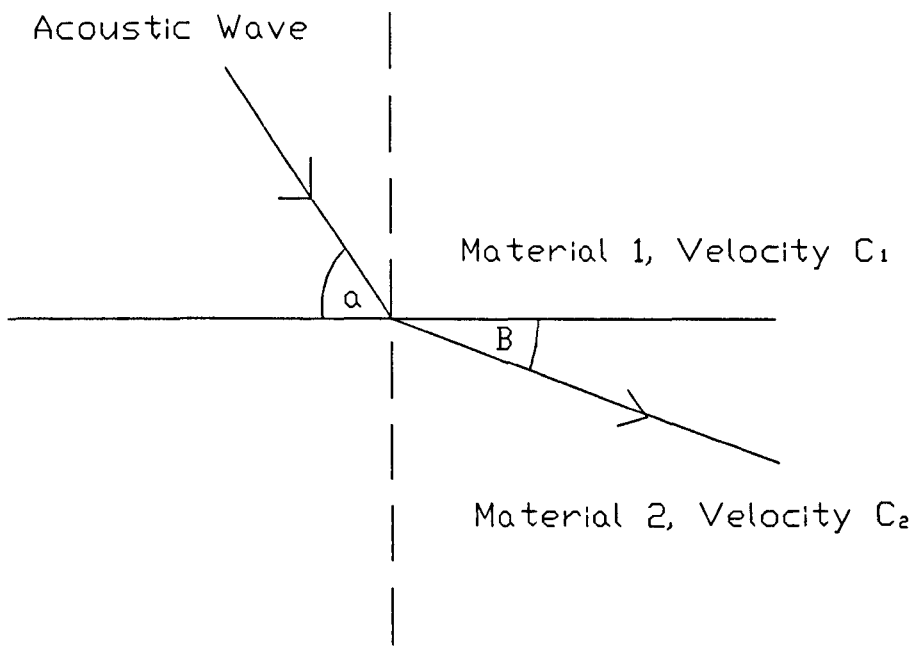

Figure 1.3. Snell's law for a wave travelling across an interface (C_2 is greater then C_1).

$$\alpha = 10 \log_{10}\left(\frac{P_1}{P_2}\right) \tag{1.9}$$

or

$$\alpha = 20 \log_{10}\left(\frac{A_1}{A_2}\right) \tag{1.10}$$

where P_1 and P_2 are the powers and A_1 and A_2 are the amplitudes.

The study of attenuation in the atmosphere has been of interest for a long time [12]. An empirically derived measurement of the attenuation in air at ultrasonic frequencies has been the subject of research [13]. Typically, in air the attenuation is dependent on the temperature, pressure, and frequency of the acoustic wave. The empirical formula gives a value of the attenuation in dB/m and is given by:

$$\alpha = 15.895X10^{-11} (T/T_0)^{1/2} f^2 (P_0/P), \tag{1.11}$$

where α is the attenuation in dB/m, T is the temperature (K), T_0 is the reference temperature (293.15 K), P is the pressure kPa and P_0 is the reference pressure (101.325 kPa). This expression is only valid in dry air over a range of 0-40°C and pressures below $2X10^2$ kPa. Additionally, attenuation in air is also dependent on the humidity, the expression above assumes dry air. This expression is incorporated in the study of the radiated fields presented in chapter 4 of this thesis.

1.5 References

[1] R.C. Brown, *Sound*, Longmans, ed 3, 1962.

[2] S. Schmidt, "Evidence for a spectral basis of texture preception in bat sonar", *Nature*, **331**, 617-619 (1988).

[3] M. Lach, H. Embert, "An acoustic sensor for object recognition", *Sensors and Actuators*, **25-27**, 541-547 (1991).

[4] C.R. Hill (ed.), Physical principles of medical ultrasonics, Ellis Horwood Ltd., Chichester, 1986.

[5] R. Halmshaw, *Non-destructive testing*, (Edward Arnold, London, 1987).

[6] J.D. Achenbach, *Wave propagation in elasic solids*, Elsevier Science, Netherlands 1990.

[7] J. Krautktamer and H Krautkramer, Ultrasonic testing of materials, 4th ed, Springer-Verlag, Berlin, 1990).

[8] B.A. Auld, *Acoustic fields and waves in solids: Vol* **2**, John Wiley & Sons New York, 1973.

[9] I.A. Viktorov, *Rayleigh and Lamb waves - Physical theory and applications*, Plenum, New York, 1967.

[10] G.S. Kino, *Acoustic waves*, Prentice Hall, Englewood Cliffs, New Jersey, 1987.

[11] L.E. Kinsler, A.R. Frey, A.B. Coppens, and J.V. Saunders, *Fundamentals of Acoustics*, 3rd ed., Wiley, New York, 1982.

[12] L.B. Evans, H.E. Bass, and L.C. Sutherland, *J Acoust. Soc. Am.* **51**, 1565-1575, 1972.

[13] L.J. Bond, C.H. Chiang, and C.M. Fortunko, "Absorption of ultrasonic waves in air at high frequencies (10-20 MHz)". *J. Acoust. Soc. Am.* **92** (4) Pt. 1, 1992.

CHAPTER 2

BACKGROUND OF THE DIFFERENT TRANSDUCERS USED FOR NON-DESTRUCTIVE TESTING OF MATERIALS

2.1 Introduction

This chapter gives a brief description of the different types of transducers and techniques used for non-destructive testing applications. Additionally, the chapter concentrates on the advantages and disadvantages of different types of transducers for generation and reception of air-coupled ultrasonic signals for NDT applications.

2.2 Contact techniques

Typically, the majority of non-destructive testing applications use piezoelectric material to generate and receive ultrasound, and by far the most common transducer is the piezoelectric contact probe. These consist of a thin disk of piezoelectric material, such as lead-zirconium-titanate (PZT) or quartz which has a metallised electrode on each face and is attached to a backing material [1-3]. To generate an ultrasonic wave in a sample, a time varying voltage is applied across the electrode which causes the piezoelectric material to vibrate in a direction depending on the material orientation. A viscous couplant is normally placed between the transducer face and the sample, which ensures full contact over the surface area and aids in transmitting longitudinal waves (viscous couplants can also support shear waves). To work as a receiver, the ultrasonic wave causes the surface of the sample to move, which in turn causes the piezo-material

to change its dimension, thus, producing a voltage on the electrodes. A schematic diagram of a typical piezoelectric contact transducer is shown in Figure 2.1.

The transducers can be employed in a range of configurations for generation and receiving ultrasound in the material under test. Firstly, the transducers can be arranged in a through-transmission configuration, where the transducers are placed on opposite sides of a sample. If they are on the same side then a pitch-catch arrangement occurs. Conversely, a pulse-echo arrangement is where a single transducer acts as both generator and a receiver of ultrasound. The transducers themselves can be sources of longitudinal or shear waves, depending on the PZT orientation, they can be inclined at some angle via a wedge to provide angled beams, which are ideal for generating Rayleigh and Lamb surface waves.

2.3 Non Contact techniques

2.3.1 Electro Magnetic Acoustic Transducer (EMAT)

These devices have been used extensively in systems where non-contact ultrasonic transduction is required [4-6], but can only be used at an electrically-conducting surface. The devices consist of a radio frequency coil placed in a static magnetic field, supplied by a magnet. In generation of ultrasound, a time varying current is passed through the coil. This induces an eddy-current in the surface of the sample, which is situated in the magnetic field. Thus, Lorentz forces exist which act on the electrons on the surface of the sample and this vibration is transmitted through the sample. As a

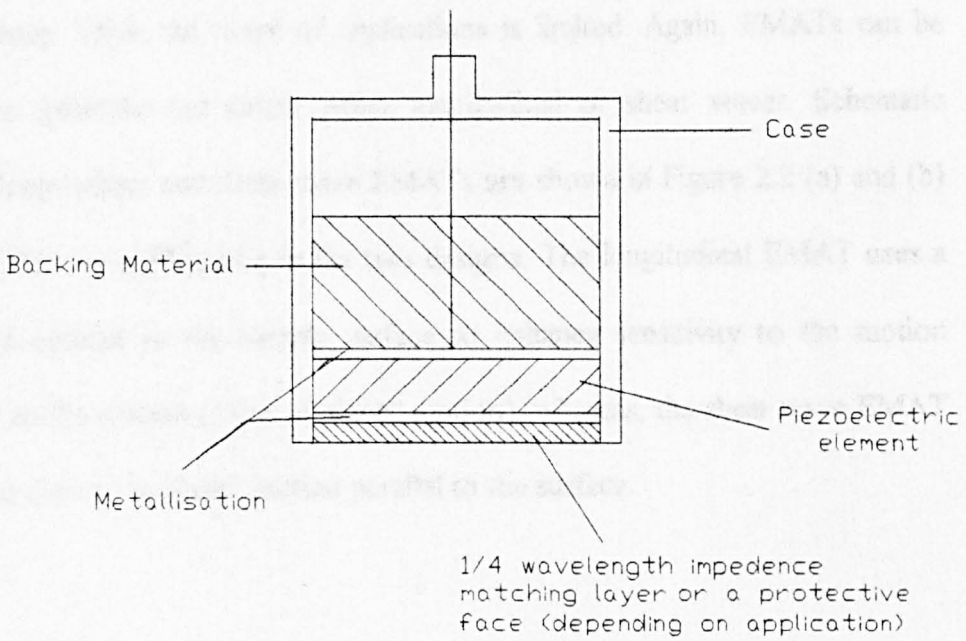

Figure 2.1. Schematic diagram of a typical piezoelectric transducer

receiver, the magnetic field from the magnet passes through the sample, and as the ultrasonic wave in the sample reaches the surface, the motion generates an eddy current at the sample surface which in turn induces a current in the coil. EMATs need the sample under test to have a conducting surface and work at a maximum distance of a few millimetres. Thus, the range of applications is limited. Again, EMATs can be constructed to generate and detect either longitudinal or shear waves. Schematic diagrams of longitudinal and shear wave EMATs are shown in Figure 2.2 (a) and (b) respectively. There is a difference in the two designs. The longitudinal EMAT uses a magnetic field parallel to the sample surface to enhance sensitivity to the motion perpendicular to the surface ("out of plane" motion), whereas, the shear wave EMAT is optimised to detect "in-plane" motion parallel to the surface.

2.3.2 Laser generation and detection of ultrasound

(a) Generation of ultrasound

The use of lasers to generate and receive ultrasound has been extensively researched [12-14]. Pulsed lasers can generate ultrasound in materials by one of three different methods [15], which is dependent on the power density of the beam. If the power density is less than 10^7 W/cm^2, then the incident laser pulse causes localised rapid heating on the surface, which expands and produces a stress wave which is naturally transverse to the direction of propagation, thus tending to produce predominately shear waves.

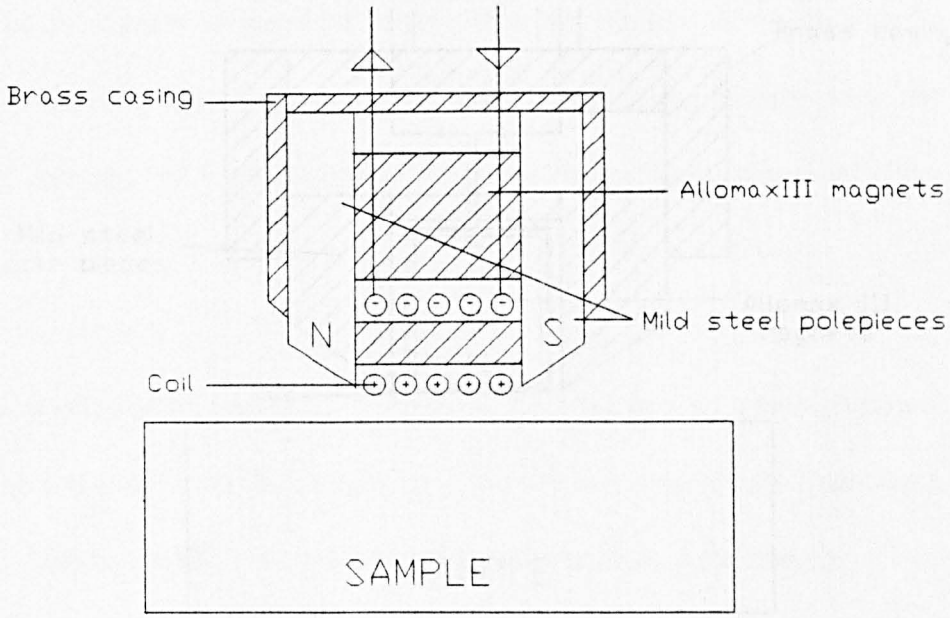

Figure 2.2 (a) Schematic diagram of a longitudinal wave EMAT

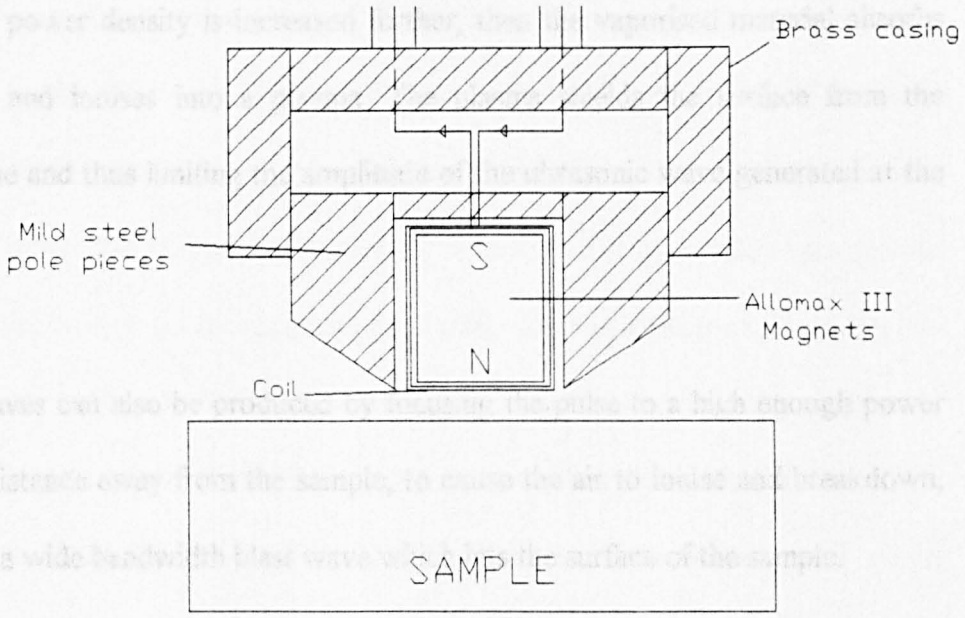

Figure 2.2 (b). Schematic diagram of a shear wave EMAT

With an increase in the power density between 10^7 W/cm^2 and 10^9 W/cm^2 , abilation occurs which causes the material at the surface to vaporise and produce stresses normal to the surface by momentum transfer, which tends to produce longitudinal waves. If the power density is increased further, then the vaporised material absorbs more energy and ionises into a plasma. The plasma shields the surface from the incoming pulse and thus limiting the amplitude of the ultrasonic wave generated at the surface.

Ultrasonic waves can also be produced by focusing the pulse to a high enough power density at a distance away from the sample, to cause the air to ionise and breakdown, thus, causing a wide bandwidth blast wave which hits the surface of the sample.

(b) Detection of ultrasound

Lasers have been used to study the movement of surfaces for many years. Suitable techniques include interferometers, and knife-edge beam detection. Interferometers are available in many forms, two of the most common being the Michelson and Confocal Fabry-Perot. Typically, interferometers rely on good optical reflection from the surface, a good degree of alignment and stable working conditions. Additionally, interferometers tend to be fairly expensive due to the high precision optics used.

(i) Michelson interferometer

This is the most common type of interferometer used [16]. The principle of operation is shown in Figure 2.3(a). Here, a laser source (usually argon-ion, or helium-neon) passes through a beam splitter, where one beam is focused onto the moving surface and the reflection is passed into a photo detector. The other beam is reflected into the same photo detector and this beam is called the reference. The phase shift between the reference and the beam from the sample is measured, either as a change in intensity for small displacements or the number of complete wavelengths that the surface is displaced for larger motion. During operation, long term in stabilities are difficult to achieve because of the changes in the ambient temperature, air turbulence, and room vibrations. Typically, an electronic signal is fed back to an electro-mechanical drive in order to position the reference mirrors so the static path length can be kept at an optimum distance. This type of instrument is known as a displacement interferometer.

(ii) Confocal Fabry-Perot interferometers.

This type of interferometer uses a reflected beam from the surface of the sample to detect small changes in the frequency of the beam due to the Doppler shift [16-19]. Within the device are two partially reflecting mirrors separated by their radius of curvature. This forms a resonance cavity, which will transmit the most light when all of the reflections are in phase. Any change in the frequency will cause the light intensity

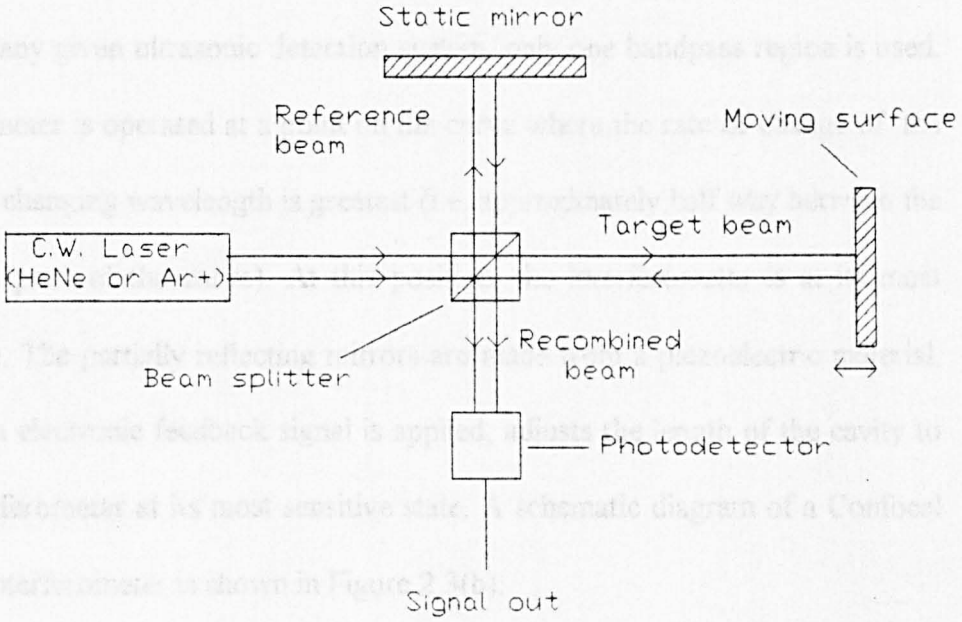

Figure 2.3 (a). Schematic diagram of a Michelson interferometer

from the cavity to change proportionally to the velocity of the surface. Also, for the Fabry-Perot interferometer, stabilisation is required to maintain optimum sensitivity. When the intensity of the light through the interferometer is plotted as a function of wavelength, a transmission curve occurs which acts as a wavelength filter, which is periodic. For any given ultrasonic detection system, only one bandpass region is used. The interferometer is operated at a point on the curve where the rate of change of the intensity with changing wavelength is greatest (i.e. approximately half way between the minimum and peak of the curve). At this position, the interferometer is at its most sensitive state. The partially reflecting mirrors are made from a piezoelectric material, which, when a electronic feedback signal is applied, adjusts the length of the cavity to keep the interferometer at its most sensitive state. A schematic diagram of a Confocal Fabry-Perot interferometer is shown in Figure 2.3(b).

(iii) Knife edge detection

The motion of the sample causes the reflected light to change its position, and thus changing the amount of light detected on the edge (knife edge) of the detector. These devices are very sensitive to alignment and external vibrations. A schematic diagram of a knife edge detector is shown in Figure 2.3(c).

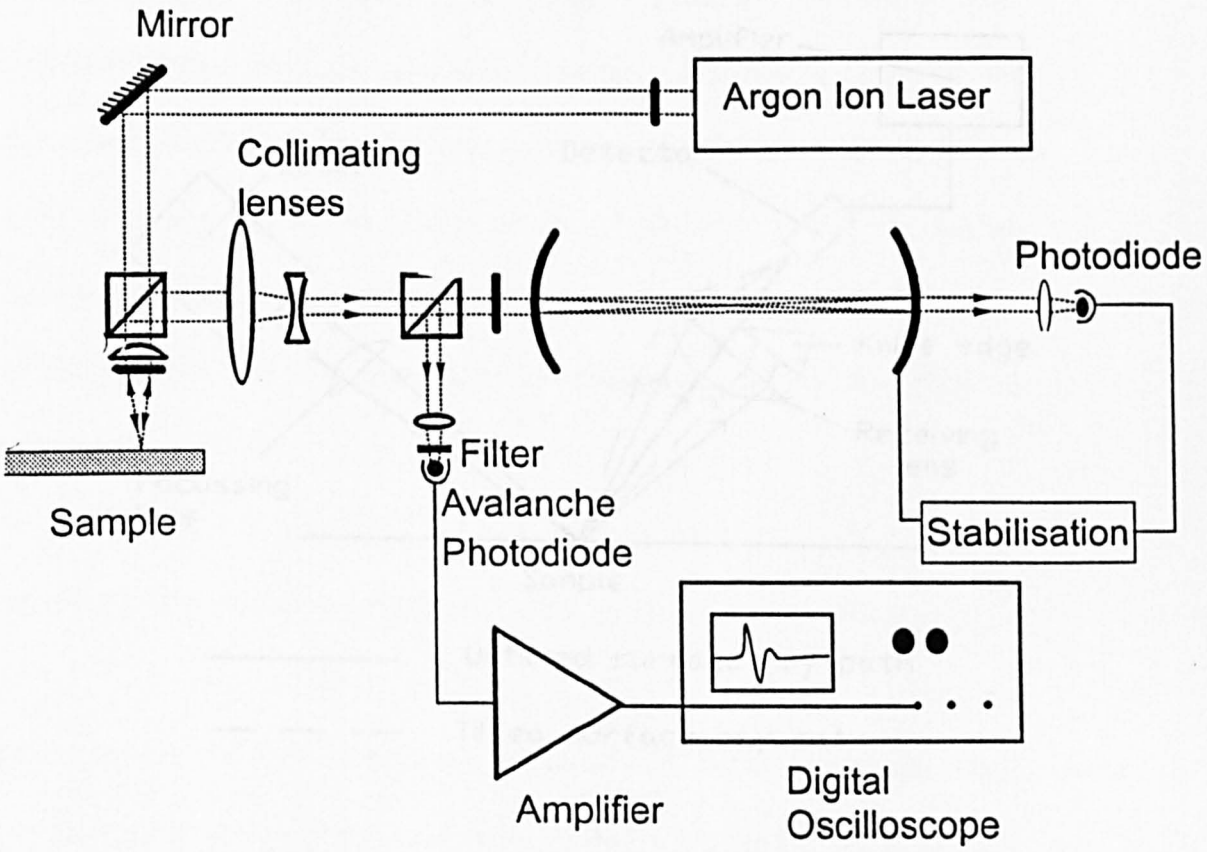

Figure 2.3 (b). Schematic diagram of a typical Confocal Fabry-Perot interferometer (supplied by Prof. R. Dewhurst, DIAS, UMIST).

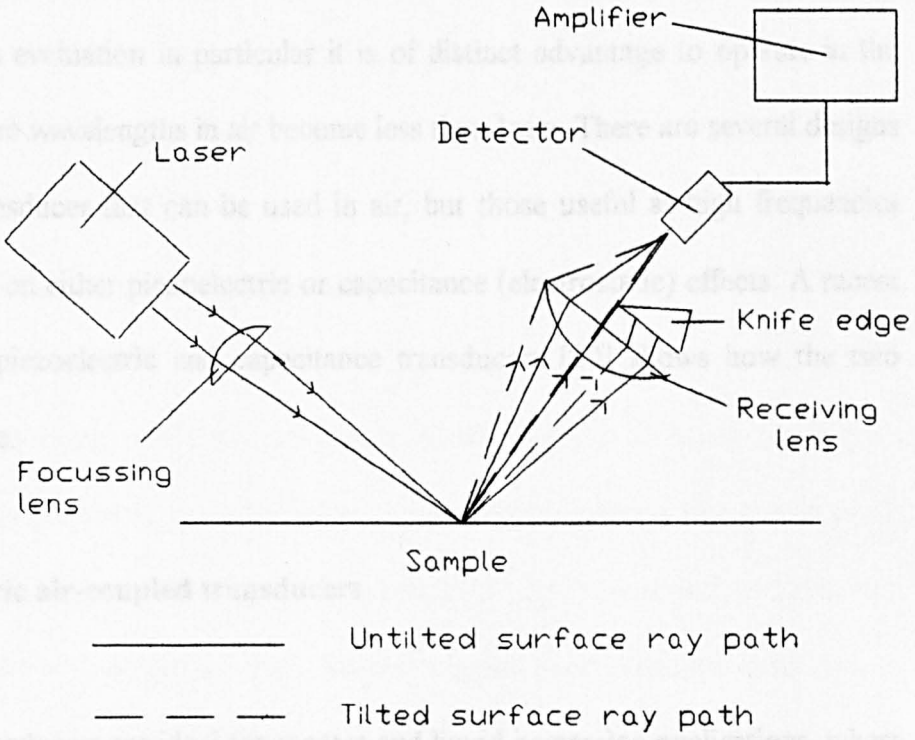

Figure 2.3(c). Schematic diagram of a knife edge detector.

2.4 Air-coupled ultrasonic transducers

The transduction of ultrasonic signals in air has gained increased interest recently, due to applications such as non-contact imaging for materials evaluation, distance ranging and robotics. Such applications require a wide range of ultrasonic frequencies in air, and for materials evaluation in particular it is of distinct advantage to operate in the MHz range, where wavelengths in air become less than 1mm. There are several designs of ultrasonic transducer that can be used in air, but those useful at high frequencies tend to be based on either piezoelectric or capacitance (electrostatic) effects. A recent review of both piezoelectric and capacitance transducers [20] shows how the two methods compare.

2.4.1 Piezoelectric air-coupled transducers

Piezoelectric transducers are ideal for contact and liquid immersion applications, where the devices have good sensitivity and bandwidth, but for use in air the major problem with conventional piezoelectric ceramic elements (such as PZT) is the large impedance mismatch at the boundary between the piezoelectric element and the surrounding air. The efficiency of these devices for coupling into air can be increased by several methods, such as using a metal diaphragm [21] to act as a vibrating membrane, or by attaching a quarter wavelength impedance matching layer to the front face. These impedance matching layers need to have a much lower acoustic impedance than the piezoelectric element, and only a small selection of materials can be used, such as silicon rubber [22], epoxy resin-quartz [23], and aerogels [24]. Further developments

have reduced the impedance mismatch with the use of a 1-3 connectivity piezocomposite active element containing piezoceramic pillars in a polymer matrix [25]. The performance can be optimised for any particular application by changing the piezoceramic pillar fraction, shape, and distribution. In general, however, it is found that such devices are optimised for narrow bandwidth operation, and recent applications have used them in such a mode [26]. Other work has been reported in thick aerospace structures [27].

2.4.2 Capacitance air-coupled transducers

The alternative method, which is used widely in this thesis, is to use a capacitance design, which was derived from earlier microphone designs, where a thin membrane is attached to a contoured, conducting rigid backplate [28,29] . Such devices have been studied extensively in past work, which has investigated their response in relation to the backplate topography for metal backplates. Some recent research has produced backplates by either depositing polyamide ridges [30], machining, or etching to form regular patterns such as grooves and holes on or into a polished backplate. The results shown by references [31-33] for V-grooved transducers suggest that the resonant frequency can quantitatively be predicted from the dimensions of a V-groove with a 90% confidence limit. It was also shown that a lumped parameter approximation could be used to describe the transducer by an equivalent electrical circuit. Both the resonant frequency and sensitivity could accurately be predicted [33,34]. Additionally, laser-induced, wide bandwidth sound from a laser beam which is focused by a lens to cause dielectric breakdown (acoustic impulse) has been used to determine the receiving

sensitivity and bandwidth of capacitance transducers [35]. A more in depth study of the response of air-coupled transducers with varying backplate topology is presented in chapter 5.

Although such devices are useful, a more extended frequency response is available from new designs of transducer, based on silicon micromachining technology [36]. Various configurations have been described, including devices machined with an *in-situ* front membrane [37].

The design to be used in this thesis uses backplates from various types of materials into which miniature cylindrical pits have been etched chemically, leading to a typical construction as shown in Figure 2.4. The details of how such devices are constructed and characterised is presented in [38], and some applications are described in [39-42]. Briefly, the backplate contains a series of uniformly-spaced holes, etched into the top surface of a flat rigid wafer. If the material is non conducting, gold is then evaporated onto the etched surface to produce a conducting backplate. A 5μm Mylar polymer membrane (with a conducting top surface) is placed on top of the etched silicon backplate for both the source and receiver, trapping pockets of air. Applying a transient voltage between the backplate and the grounded front metallized surface of the membrane forces the membrane into motion, thus generating ultrasound in air. Detection can be achieved using an identical device, but a d.c. polarisation voltage is required so that dynamic charges are induced on the backplate by motion of the membrane. Advantages of the above devices include the ease of manufacture, and the ability to reproduce field characteristics by introducing controlled surface roughness.

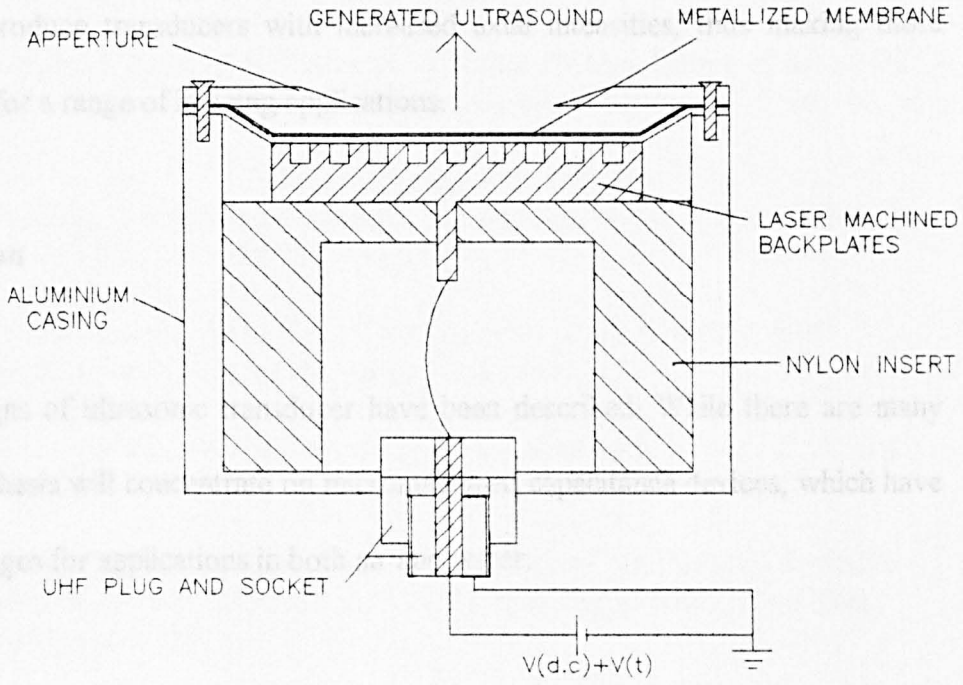

Figure 2.4. Schematic diagram of an air-coupled capacitance ultrasonic transducer.

Using the construction of the backplate outlined above, the transducer is found to have a good response into the MHz region, well-damped and with excellent sensitivity. As will be shown, in later chapters, with additional modifications to the aperture it is possible to produce transducers with increased axial intensities, thus making these devices ideal for a range of imaging applications.

2.5 Conclusion

Various designs of ultrasonic transducer have been described: While there are many designs, this thesis will concentrate on micromachined capacitance devices, which have many advantages for applications in both air and water.

2.6 References

[1] J. Krautkramer and H. Krautkramer, *Ultrasonic testing of materials*, 4th edition, (Springer-Verlag, Berlin, 1990).

[2] R. Halmshaw, *Non-destructive testing*, (Edward Arnold, London, 1987).

[3] W. Sachse, N.N. Hsu, "Ultrasonic transducers for materials testing and their characterisation", in *Physical Acoustics - Principles and Methods*, eds. W.P. Mason, R.N. Thurston, (Academic, New York, 1979), Vol XIV, pp 277-406.

[4] H.M. Frost, "Electromagnetic ultrasonic transducers: Principles, Practice and application", in *Physical Acoustics --Principles and Methods*, eds. W.P. Mason, R.N. Thurston, (Academic, New York, 1979), Vol XIV, pp 179-276.

[5] R. B. Thompson, "Physical properties of measurements with EMAT transducers", in *Physical Acoustics - Principles and Methods*, eds. R.N. Thurston, A.D. Pierce, (Academic, New York, 1990), Vol XIX, pp 157-200.

[6] J.P. Komorowski, D.L. Simpson, R.W. Gould, "A technique for rapid impact damage detection with implication for composite aircraft structures", *Composites*, **21**, pp 169-173 (1990).

[7] R.H. Fassbender, D.J. Hagemir, "Low voltage radiography of composites", *Mat Eval*, **41**, pp 831-838 (1983).

[8] T. DeKalbermatten, R. Jaggi, P. Fluiler, H.H. Kausch, P. Davies "Microfocus radiography studies during mode I interlaminar fracture tests on composites, *J. Mater. Sci Lett.*, **11**, pp 543-546 (1992).

[9] D.P Almond, P.M. Patel, I.M. Pickup, H.M. Reiter, "An evaluation of the sutability of thermal interferometry for the testing of plasma sprayed coatings, *NDT Int.*, **18**, pp 17-24 (1985).

[10] W.N. Reynolds, "Inspection of laminates and adhesive bonds by pulse-video thermography", *NDT Int.*, **21**, 229-232 (1988).

[11] S.K. Lau, D.P Almond, J.M Milne, "Quantitative analysis of pulsed video thermography", *NDT and Eval. Int*, **24**, pp 195-202 (1991).

[12] R.M White, "Generation of elastic waves by transient surface heating", *J. Appl. Phys*, **34**, pp 3559-3567 (1963).

[13] D.A. Hutchins, "Ultrasonic generation by pulsed lasers", in *Physical Acoustics-Principles and methods*, eds. W.P Mason, R.N. Thurston, (Academic, New York, 1988), Vol XVIII, pp21-123.

[14] C. Edwards, G.S. Taylor, S.B. Palmer, "Ultrasonic generation with a pulsed TEA CO_2 Laser", *J.Phys. D: Appl. Phys.*, **22**, pp1266-1270 (1989).

[15] W.M.D. Wright, "Air-coupled ultrasonic testing of materials", PhD thesis, Dept. Of Engineering, University of Warwick, Coventry, UK, CV4 7AL. (1996).

[16] J.W. Wagner, "Optical detection of ultrasound", in *Physical Acoustics - Principles and methods*, eds. W.P. Mason and R.N. Thurston, (Academic, New York, 1990) Vol XIX, pp 201 - 266

[17] C. Fabry, A. Perot., *Ann Chim. Phys.*, 16, pp 115 (1899).

[18] J.P Monchalin., "Optical detection of ultrasound at a distance using - confocal Fabry - Perot - Interferometer", *Appl. Phys. Letts.* **47**(1), pp14-16 (1985).

[19] J.P Monchalin., "Detection at a distance of laser - generated ultrasound using a confocal Fabry - Perot - Interferometer", *Can J. Phys.* **64**, pp1320-1323 (1986).

[20] C. Wykes "Advances in air-coupled ultrasonic transducers" (1995).

[21] M.Babic, " A 200-kHz Ultrasonic transducer coupled to the air with a radiating membrane," *IEEE Transactions (UFFC)*, **38 (3)**, 252-255 (1990).

[22] J.D.Fox, B.T.Khuri-Yakub, "High frequency wave measurements in air," *Proc. IEEE Ultrasonics Symposium*, 581-592 (1983).

[23] P.Kleinschmidt, V.Magori, "Ultrasonic remote sensors for non-contact object direction," *Siemens Forschung und Entwicklungs Be-richt*, **10 (2)**, (1981).

[24] O.Krauß, R.Gerlach, J.Fricke, "Experimental and theoretical investigations of SiO_2-aerogel matched piezo-transducers," *Ultrasonics*, **32 (3)**, 217-222 (1994).

[25] D.Reilly, G.Hayward, "Through air transmission for ultrasonic non-destructive testing," *Proc. 1991 IEEE Ultrasonics Symposium*, 763-766 (1991).

[26] R.Farlow and G.Hayward, "Real-time ultrasonic techniques suitable for implementing non-contact NDT systems employing piezoceramic composite transducers," *Insight*, **36**, 926-935 (1994).

[27] C.M.Fortunko, J.O.Strycek and W.A.Grandia, "Nondestructive testing of "thick" aerospace honeycomb structures using through-transmitted ultrasonic guided waves," *Rev. Prog. Quant. NDE*, **8B**, 1643-1650 (1990).

[28] H.Carr, W.S.H Munro, M. Rafiq, and C. Wykes, "Developments in capacitive transducers", *Nondest. Test. Eval.* **10**, pp3-14 (1992).

[29] H. Carr, " Electrostatic transducers for airborne ultrasonics", Ph.D thesis, University of Nottingham. (1989).

[30] M.J.Anderson, J.A.Hill, C.M.Fortunko, N.S.Dogan, R.D.Moore "Broadband electrostatic transducers; modelling and experiments," *J. Acoust. Soc. Am.* **97**, 262-272 (1995).

[31] H.Carr, C.Wykes, "Diagnostic Measurements in capacitance transducers," *Ultrasonics*, **31**, 13-20 (1993).

[32] M.Rafiq, C.Wykes "The performance of capacitive ultrasonic transducers using v-grooved backplates," *Measurement Science and Technology* **2**, 168-174 (1991).

[33] J. Hietanen, J. Ignatius, J. Stor-Pellinen " Electrostatic Solutions for a Capacitive Ultrasonic Air transducer with a Uniformly V-Grooved Backplate", *Sensors and Actuators*, **45**, pp95-98 (1994).

[34] J. Hietanen, J. Stor-Pellinen, M. Luukkala "A model for electrostatic Ultrasonic Transducer with grooved backplates", *Meas. Sci. Tech* **3**, pp 1095-1097 (1992).

[35] J. Hietanen, M. Oksanen, "Photoacoustic Testing of Ultrasonic Air Transducer", *Meas. Sci. Tech*, **5**, pp960-963 (1994).

[36] K. Suzuki, K. Higuchi and H. Tanigawa, "A silicon electrostatic ultrasonic transducer," *IEEE Trans. Ultras. Ferr. Freq. Contr.* **36**, 620-627 (1989).

[37] M.I.Haller, B.T.Khuri-Yakub, "A surface micromachined electrostatic ultrasonic air transducer," *Proc 1994 Ultrasonics Symposium*, 1241-1243 (1994).

[38] D.W. Schindel, D.A. Hutchins, L. Zou and M. Sayer, "The design and characterisation of micromachined air-coupled capacitance transducers," *IEEE Trans. Ultras. Ferr. Freq. Contr.* **42**, 42-50 (1995).

[39] D.W. Schindel and D.A. Hutchins, "Applications of micromachined capacitance transducers in air-coupled ultrasonics and nondestructive evaluation," *IEEE Trans. Ultras. Ferr. Freq. Contr.* **42**, 51-58 (1995).

[40] D.W. Schindel and D.A. Hutchins, "Through-thickness characterisation of solids by wideband air-coupled ultrasound," *Ultrasonics* **31**, 11-17 (1995).

[41] D.A. Hutchins, W.M.D. Wright and D.W. Schindel, "Ultrasonic measurements in polymeric materials using air-coupled transducers," *J. Acoustic. Soc. Am.* **96**, 1634-1642 (1994).

[42] B. Hosten, D.A. Hutchins and D.W. Schindel, "Measurement of elastic constants in composite materials using air-coupled ultrasonic bulk waves," *J. Acoust. Soc. Am.* **99** (4), 2116-2122 (1996).

CHAPTER 3

THE RESPONSE OF AIR-COUPLED ULTRASONIC TRANSDUCERS FOR VARIOUS BACKPLATE GEOMETRIES

3.1 Introduction

This chapter describes the manufacture and design of backplates for air-coupled capacitance transducers. Typically, as shown in chapter 2, the operation of the transducer can be described as a condenser microphone. Here, a thin membrane (usually a polymer) is used which has a surface covered by a thin layer of metal to produce an electrode. This is placed onto a contoured backplate with a conducting surface, thus trapping air between the contours and the membrane. The membrane is held in place by electrostatic attraction provided by a bias voltage across the electrodes, and is driven into motion by applying an additional time varying voltage.

The geometry of the backplate has been the focus of much research, and is one of the factors which determines the characteristics of the transducer. The membrane material thickness and applied bias voltage also have significant effect on the characteristics of the transducer.

The first form of an air coupled transducer appeared in 1917, which consisted of a stretched thin metal diaphragm fixed between two electrodes at a small distance from

the backplate [1]. Typically, these transducers were highly resonant (about 17kHz). The resonance was suppressed by introducing air damping in the form of holes or grooves in the backplate. At the time these transducers were called condenser microphones. By the 1950's an advanced design of the transducer appeared which replaced the metal diaphragm with a thin (10μm) polymer such as polyvinalchloride or polystreyne which was coated with a metal electrode [2] on one surface and placed directly onto a metal backplate which a polished, grooved or roughened backplate. Additionally, different membrane thickness and backplate topology was investigated by a number of researches who either concentrated on roughened [3-5] or grooved [1][6,7] backplates. The surface of a backplate for a capacitance transducer can either be textured (as in a roughened surface) or machined (as in a V-groove backplate). A variety of techniques for producing textured backplates have been investigated, including chemical etching, mechanical machining and shot peening [8]. Some recent research has produced backplates by either depositing polyamide ridges [9], machining, or etching to form regular patterns such as grooves and holes on or into a polished backplate. The results shown by references [10,11] for V-grooved transducers suggest that the resonant frequency can quantitatively be predicted from the dimensions of a V-groove with a 90% confidence limit. It was also shown that a lumped parameter approximation could be used to describe the transducer by an equivalent electrical circuit. Both the resonant frequency and sensitivity could accurately be predicted. Thus, placing a thin membrane on top of a textured backplate resulted in a significant increase in the sensitivity and bandwidth of the transducer, with the resonance exceeding well over 100kHz. Flat polished backplates (no machining) have also been investigated [12], and these produced bandwidths up to 3MHz (using

thin film, typically 5μm thick) and a resonance between 1-2 MHz. More recently, with the development of micromaching techniques air pockets with dimensions of only a few microns could be produced. This was done either by depositing polyamide rails onto the surface of the backplate [9], machining (chemical etching) an array of integrated cavities and membrane on a silicon substrate [13]. These types of transducers tended to have a high but very resonant frequency, typically 9MHz, and are complex in construction, and manufacture. Next micromachining small regular holes into the polished surface of a backplate [14] (either silicon or any metal), thus leaving a significant area on the backplate to generate the high frequencies (as with the polished backplate) with the holes giving the damping and lower frequency characteristics. The latter technique gives rise to a transducer which is simple in construction, has controllable characteristics, increased bandwidth, (typically, 3MHz, but is limited by the attenuation in air) and good sensitivity. Thus, this type of air-coupled transducer is subjected to further study throughout this thesis.

3.2 Theoretical Frequency Characteristics

One of the first models used to described the behaviour of capacitance transducers assumed that the membrane acted as a frictionless piston, with the air trapped between the membrane and the backplate acting as a spring [3,4][7][10], where the resonant frequency is given by:

$$f = \frac{1}{2\pi}\sqrt{\frac{\gamma . P_a}{\rho . t_a . t_f}} \qquad (3.1)$$

where γ is the adiabatic constant for air, P_a is the atmospheric pressure, ρ is the density of the membrane, and t_f and t_a are the thickness of the film and air gap respectively. This equation can be used with reasonable accuracy to predict the resonant frequency of a devices with backplates of varying surface roughness up to 600kHz. However, the theory is limited because of the random surface topology of roughened backplates, where a single value for t_a cannot be used. Also, the membrane is far from being frictionless. Further development to develop a more accurate method to predict the resonant frequency was shown by Carr and Wykes [10,15], where the air gap can be determined by the measured capacitance, and hence used in a experimentally-derived equation for the resonant frequency (accurate to 1MHz):

$$f(\text{kHz}) = (390 \pm 30) + (1110 \pm 50)\, d \qquad (3.2)$$

where d is the air gap determined from the capacitance measurement. This equation is valid for polymer membranes (such as Mylar or Kapton) with a thickness between 2μm and 15 μm.

Again, much work has been done on predicting the resonant frequency of a grooved backplates. However, disagreement occurs between different researchers on how the transducers operate. One of the main factors for grooved backplates as reviewed by Wykes [11] is the width of the grooves, where the wavelength of the fundamental resonance of the membrane is equal to twice the width of the groove, as the membrane is driven in phase at the rails, the even harmonics would cancel out leaving the odd harmonics which was confirmed by the report of a multipeak response [2].

Additionally, the air gap between the membrane and the rail will have a different stiffness than the air gap in the groove, and thus it is thought that this may be the main factor in determining the resonant frequency. Also, other views include the resonance of the membrane [2], and the surface finish of the rails [6].

Typically, when the dimensions of the grooves are less then the resonant wavelength, a Helmholtz resonator model can be used [7] where the resonant frequency f is given by:

$$f = \frac{c}{\pi}\sqrt{\frac{\rho_0}{2.\sigma.h}} \qquad (3.3)$$

where c is the speed of sound in air, ρ_0 is the density of air, σ is the mass per unit area and h is the depth of the groove. For a wide range of groove dimensions, the measured resonant frequency is close to the predicted resonant frequency using (3.3) a result confirmed later in [16]. Additionally, for each backplate the tension was the membrane was also varied from 0.6-6 N, however, this did not produce a significant change in the measured resonant frequency. As predicted from the equation (3.3), the smaller the depth of the groove, the higher the resonant frequency. Also, this applies to roughened backplates [17] where a decrease in the depth of the air pocket (reduced roughness) results in a higher resonant frequency and greater bandwidth. Conversely, as the resonance and bandwidth increase (due to the reduced groove depth) the sensitivity decreases [18]. Additionally, other factors which also has been shown to effect the response of the device include the thickness of the membrane [16] where the

thinner the membrane the greater the bandwidth, resonance and sensitivity. However, as shown in [19], in the case of roughened backplates, there is an optimum film thickness to achieve the greatest sensitivity for a given roughness. Applying a d.c bias between the membrane and the backplate can have the effect of increasing the bandwidth, resonance and sensitivity of the device. With no bias applied, the membrane is resting 'loose' on top of the backplate and gives an undamped response. However, when a bias is applied, the membrane is attracted closer to the backplate, thus reducing the depth of the air gap, and also increasing the capacitance. Any small change in the motion of the membrane will then result in a greater change in the charge on the membrane and thus the sensitivity is increased. As the bias increases, the membrane is held against the backplate and thus becomes stiffer. The resulting signal becomes damped, thus increasing the bandwidth of the device, but also decreasing the sensitivity. As far as the sensitivity is concerned, there is an optimum operating bias voltage but practically this is difficult to achieve due to the effects of polarisation of the polymer membrane (discussed under the electret section). For the case of using 5μm thick Mylar for the membrane, it is possible to apply up to 1KV bias which had the effect of causing the surface topology of the backplate to have an increasing effect on the response. Typically, the spectra for this condition [19] shows two separate peaks, where the lower frequency is due to the natural resonance of the membrane and the higher frequency is due to the surface topology of the backplate.

Although different factors concerning the response of the device have been briefly mentioned, this chapter will mainly focus on the effect of the micromachined cavities in the backplate on the response of the transducer, when driven as a source.

3.3 Manufacturing techniques and evaluation

Backplates were manufactured using etching techniques for silicon and metal. The backplates were then mounted onto a 12.5mm diameter holder (used for mounting samples for SEM) and secured with conducting epoxy. The holders had a 1mm diameter 5mm long pin which was inserted into a nylon insulator (see chapter 2). An electrical connection was made to the pin using a plug and socket arrangement (the pin acted as the plug). Hence, the backplates could be changed by sliding the nylon insert out of the back of the transducer, thus leaving the membrane and clamping aperture untouched (ideal for comparing backplates as the membrane and clamping pressure has a significant effect on the characteristics).

3.3.1 Backplate Preparation

Backplates were fabricated by chemical etching, ion beam machining and laser machining techniques. In the case of etched backplates, the surfaces were coated uniformly over a $1cm^2$ area by spinning a 3μm thick layer of polyamide photo-resist at 1200 rpm, followed by a soft bake in an oven at 90°C for 5 minutes. The backplates were attached to a mask containing 70μm square holes at a pitch of 70μm, placed in front of an ultra violet light source (which has a spectral output in the range of 350-450 nm) for 4 minutes. The backplates were placed into a developer which dissolved the exposed area, leaving the unexposed portion of the polymer. After hard baking the

sample at 180°C for 1 hour, the backplates were ready for machining. Polished silicon wafers are ideal for producing backplates, due to a flat and scratch- free surface. This enables us to have greater control over the characteristics of the transducers. Typically, when chemically etching silicon, a mask pattern is transferred into an oxide layer which is deposited onto the surface. In our case we only require a depth of less than 10μm, and thus we submerged the polished pure silicon backplate into a anisotropic etchant (hydrofluoric and nitric acid solution; the wafer was orientated in the (100) plane) for 1 minute and then washed in water. A pattern depth of about 2-4 μm was achieved before the photo resist dissolved away.

For the case of the showered ion-beam technique, the wafer was placed 75mm below the gun (ion-beam source) onto a copper heatsink due to the high temperatures generated, and the milling rate was kept low (0.1μm/min). After 15 minutes the photo resist had been milled away leaving a pattern about 2μm deep; due to the different milling rates between the photo resist and the silicon, only 66% of the photo resist thickness was transferred.

The laser machining technique only required a polished silicon backplate which was placed onto an X-Y stage and positioned in front of a Q-switched Nd.YAG laser with 100mm focal length, 8X beam magnification and 1.5mm aperture fitted. A silicon backplate with hole diameter of 50μm, pitch of 80μm and depth of 10μm was

produced. Again, the same laser machining technique was applied to a polished stainless steel backplate producing holes of the same dimensions.

For the polished copper backplate, a potassium hydroxide solution etchant at 50°C was used. After 10 minutes a hole depth of 10μm was achieved. The chemical etching of stainless steel used a ferric chloride based etchant immersed for 5 minutes giving a hole depth of 10μm.

For each silicon backplate, a micrograph surface view (X40 magnification) and received ultrasonic frequency spectrum in air is shown. Figure 3.1 is for the HF etched, Figure 3.2 for the ion-beam machined, Figure 3.3 for the laser machined samples. Again, for each metal backplates, a micrograph surface view and transmitted spectrum are shown in Figure 3.4 for the laser machined stainless steel, whereas Figure 3.5 is for the KOH etched copper and Figures is 3.6 for the FeCl etched stainless steel.

The dimensions of the holes machined into the backplates are shown in Table 3.1 for each technique.

Backplate Machining Technique	Width / Diameter (μm)	Pitch (μm)	Depth (μ)
Ion-beam (silicon)	70 X 70	70	2
Laser machining (steel)	50 diameter	80	10
Laser machining (silicon)	50 diameter	80	10
Potassium Hydroxide etch (copper)	70 X 70	70	10
Hydrogen Floride etch (silicon)	70 X 70	70	10
Hydrogen chloride etch (steel)	70 X 70	70	10

Table 3.1

3.3.2 Evaluating the characteristics of the backplates

A series of 5μm thick membrane capacitance transducers were assembled [1], each containing one of the prepared backplates. A 200V bias voltage was applied across the membrane, attracting the membrane onto the backplate. Each transducer was driven by a pulse with a width of 0.1μs, at 350V. The transmitted signal was received by a wide bandwidth capacitance transducer fitted with a 2.5μm thick membrane, amplified by a charge amplifier with a 100V d.c bias applied. The Fourier transform of the received signal was taken giving the frequency spectrum for each backplate.

Comparing the spectrum of each backplate, there was a noticeable change in the position of the peak sensitivity. Both laser machined silicon and stainless steel backplates had peaks which were centered at 1MHz, with an upper response close to 3MHz. Again, the ion-beam machined silicon backplate gave the same characteristics. It is clear from the micrographs that the laser and ion-beam machined backplates had the smoothest surface finish, and that the holes are well defined with sharp edges; thus, the charge concentration close to the membrane is increased. With the chemically etched backplates, it is clear from the micrographs that the enchants had etched below the photo resist layer, leaving a roughened surface (in some cases, parts of the mask had lifted of the surface). In the case of the chemically etched silicon, the surface had been slightly roughened and the edges of the holes had been blunted by the enchant, but they were still reasonably sharp and well defined. Again, the surface of the chemically etched copper and steel backplates were more severely roughened, both having blunted corners.

Analysis of Figures 3.1-3.6 indicate that with an increase in the surface roughness and a decrease in edge sharpness, the frequency at which the peak sensitivity occurs decreases. For the etched silicon, this peak occurred at about 900kHz, whereas it was 750kHz for the etched copper and stainless steel. Comparing the backplates which had a typical hole depth of about 2-4μm (i.e. chemically etched and ion-beam machined silicon) to the backplates which had hole depth close to 10μm (i.e. laser machined silicon and steel and chemically etched copper and steel), the amplitude of the peak sensitivity was significantly higher for the shallow holes; again, this is possibly due to a

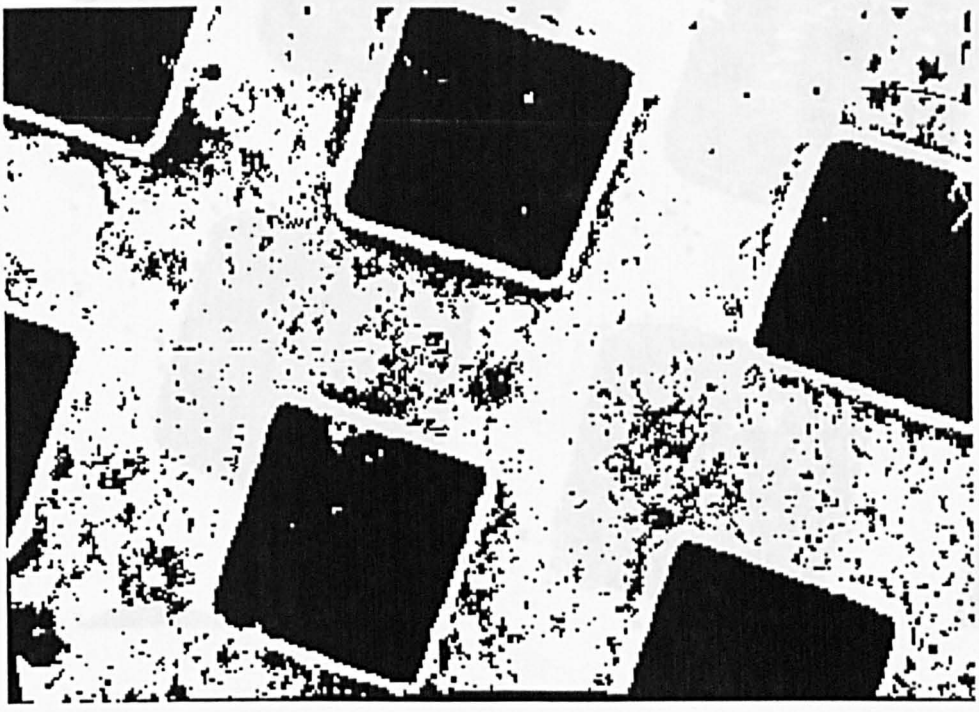

(a)

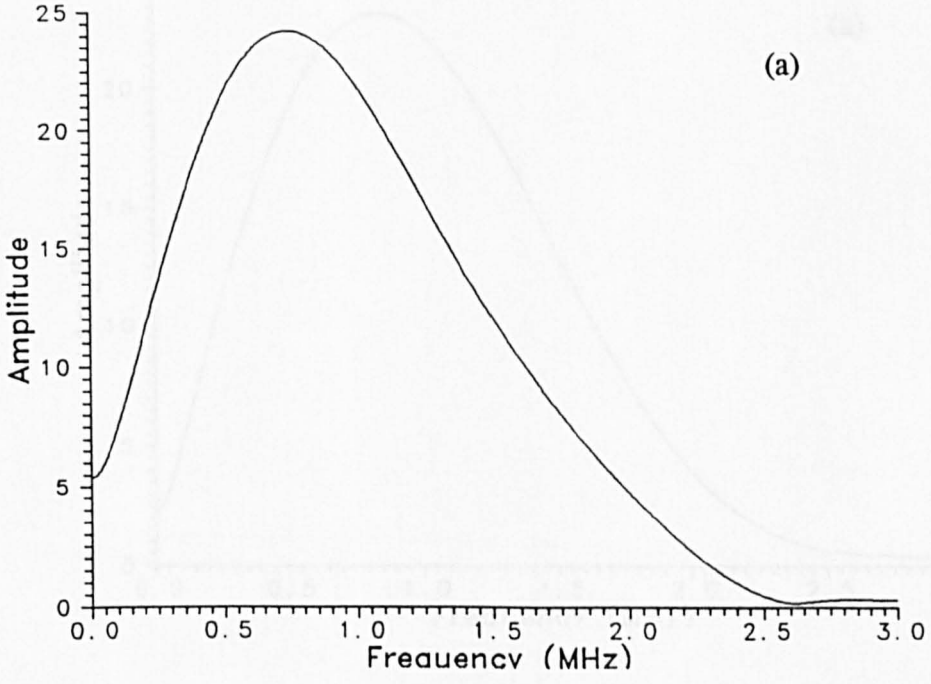

(b)

Figure 3.1, (a) Etched silicon using an HF based etchant, (b) is the received spectrum.

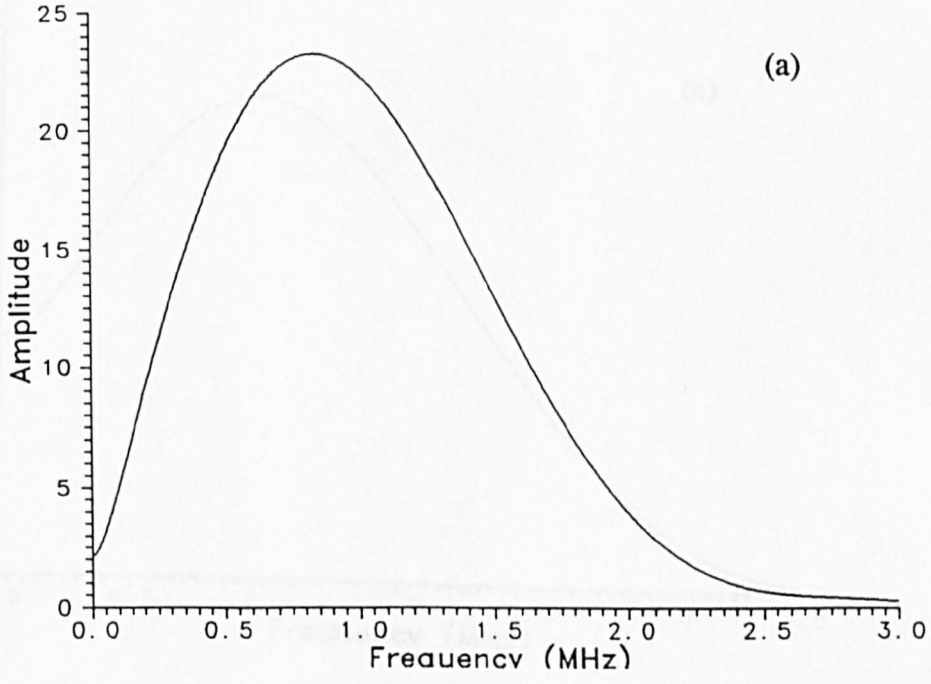

(a)

(b)

Figure 3.2, (a) Etched silicon using Ion beam machining, (b) is the received spectrum.

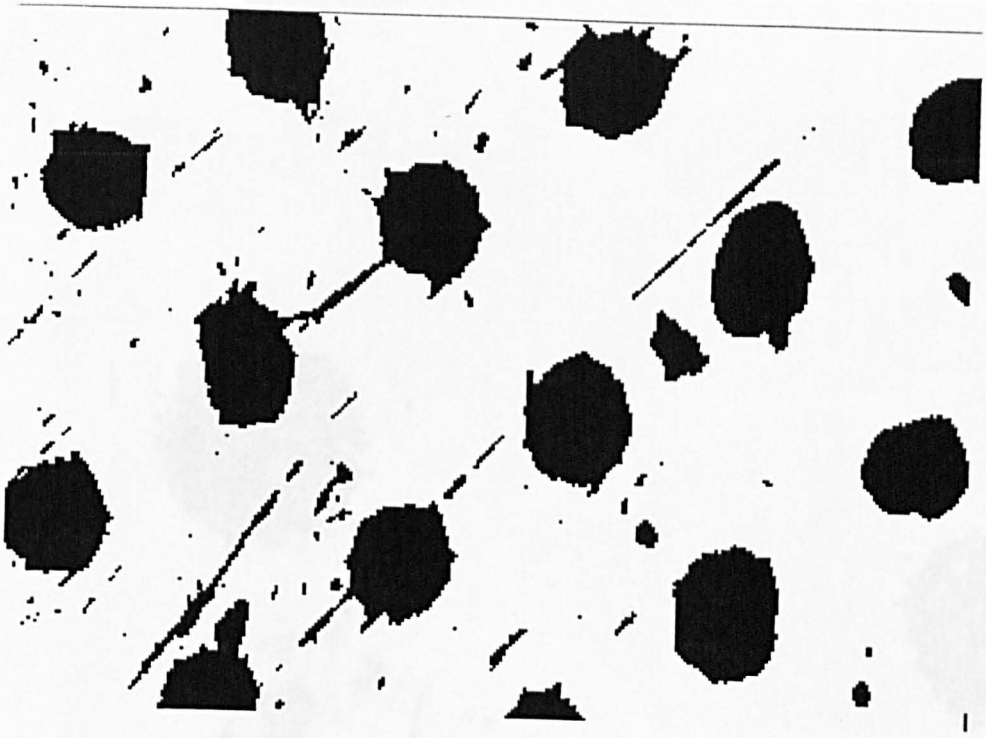

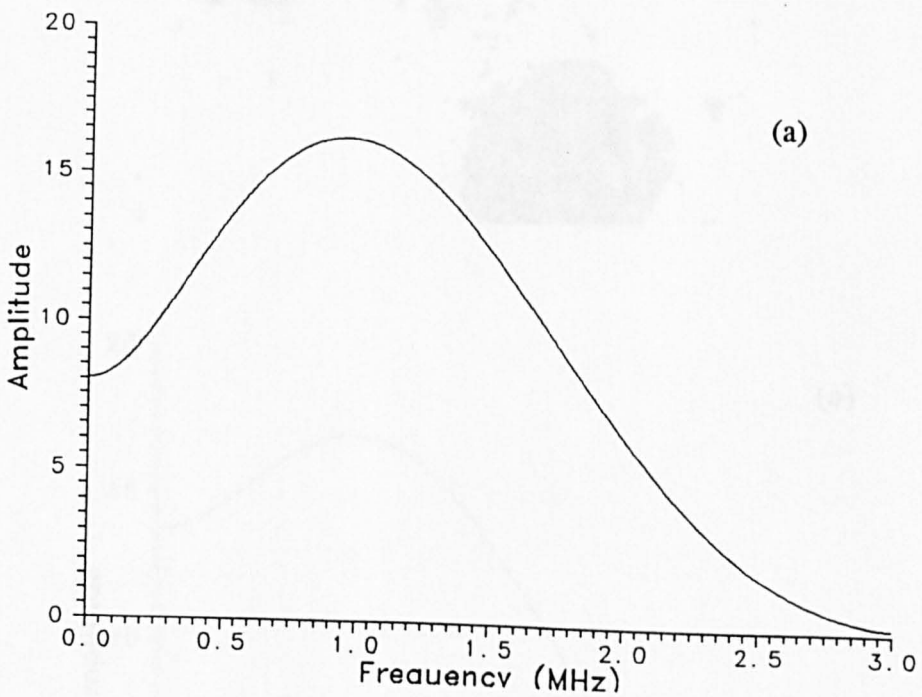

(a)

(b)

Figure 3.3, (a) Etched silicon using laser machining (magnification reduced to show the overall array of holes), (b) is the received spectrum.

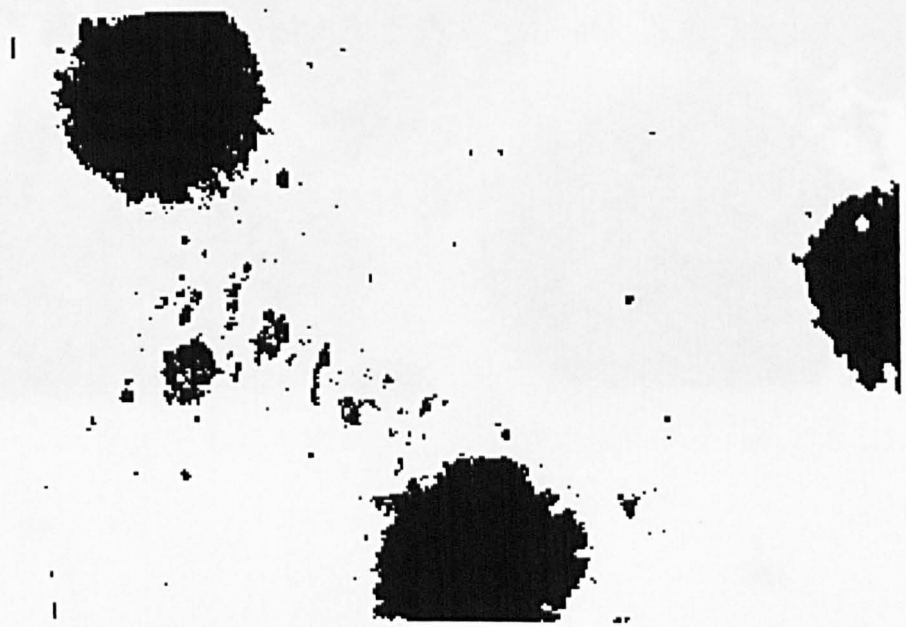

(a)

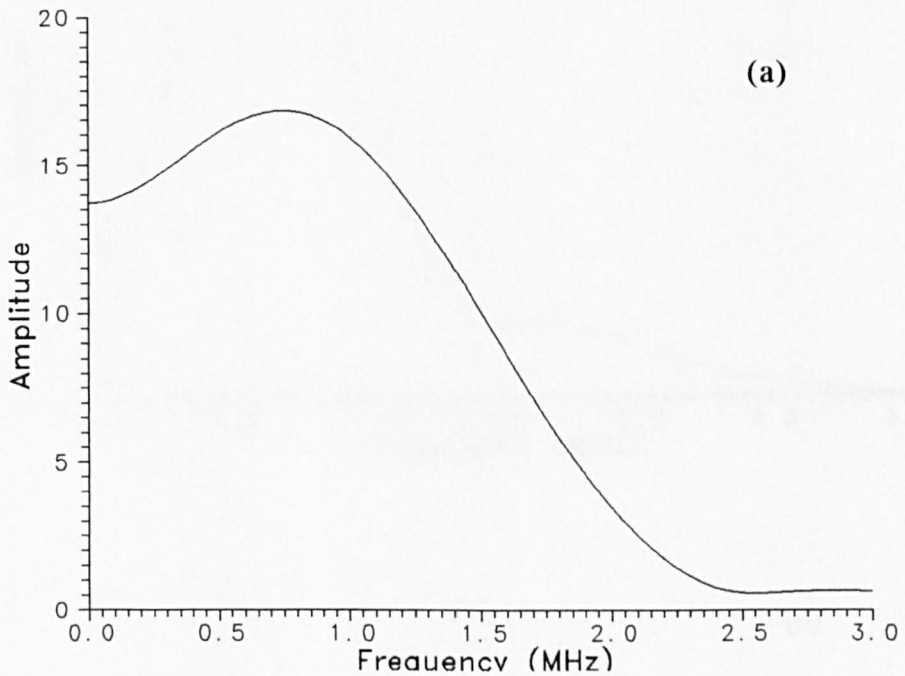

(b)

Figure 3.4, (a) Etched steel using laser machining, (b) is the receives spectrum.

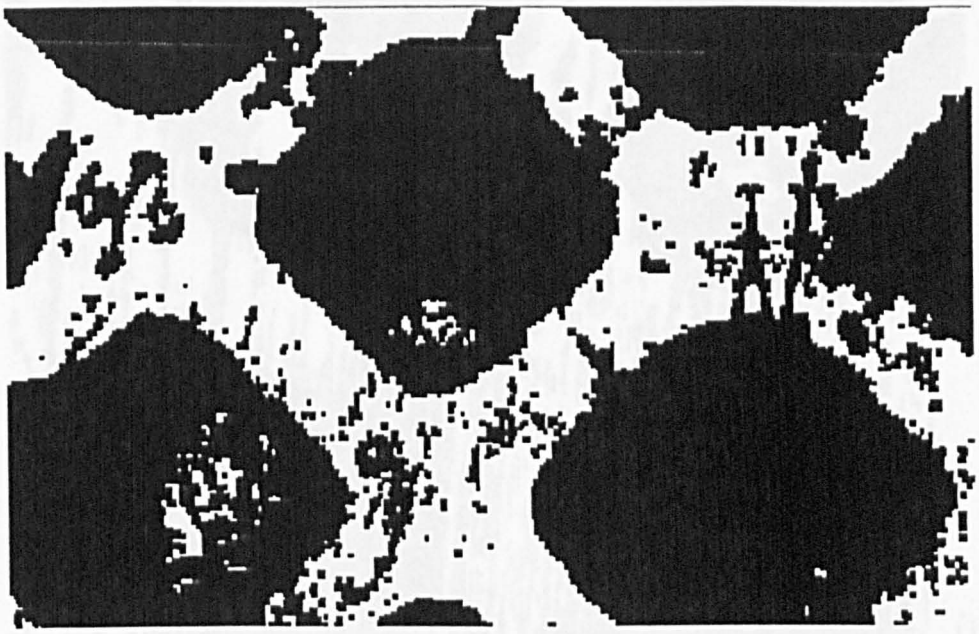

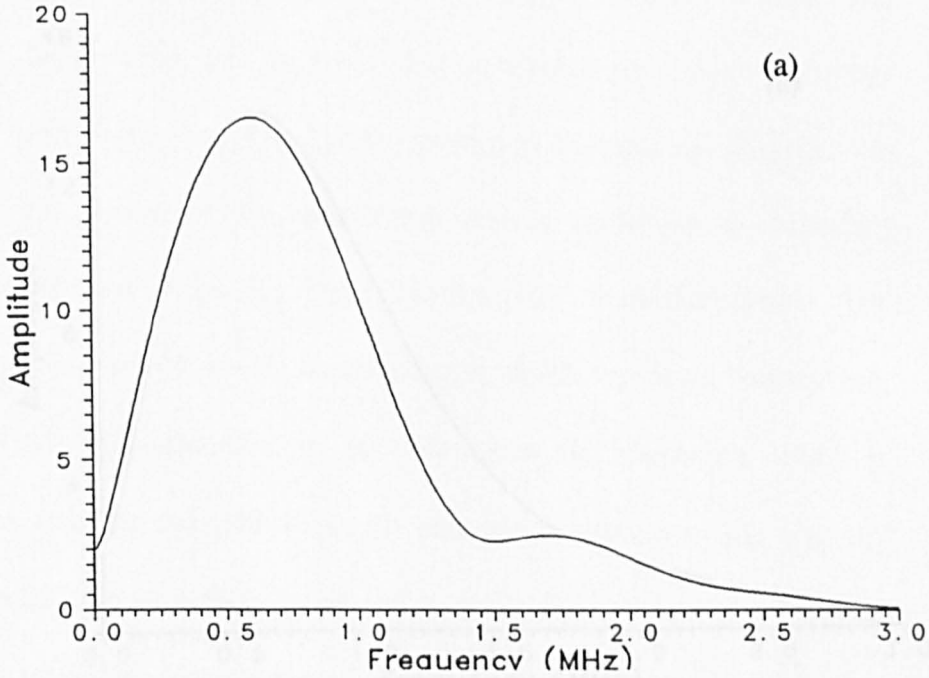

(a)

(b)

Figure 3.5, (a) Etched copper using an KOH etchant, (b) is the received spectrum.

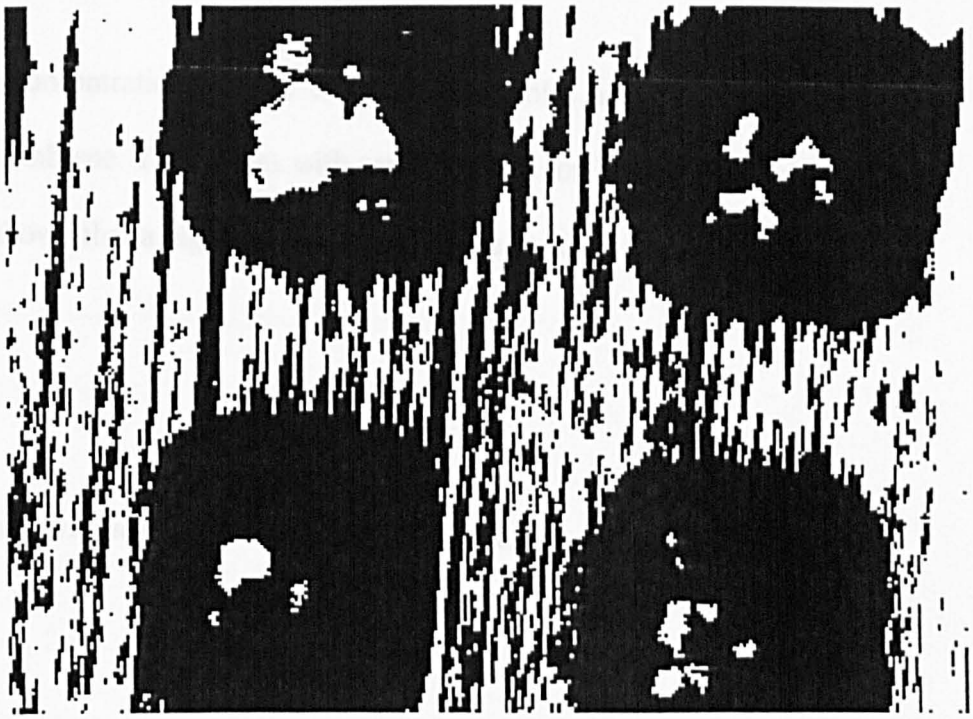

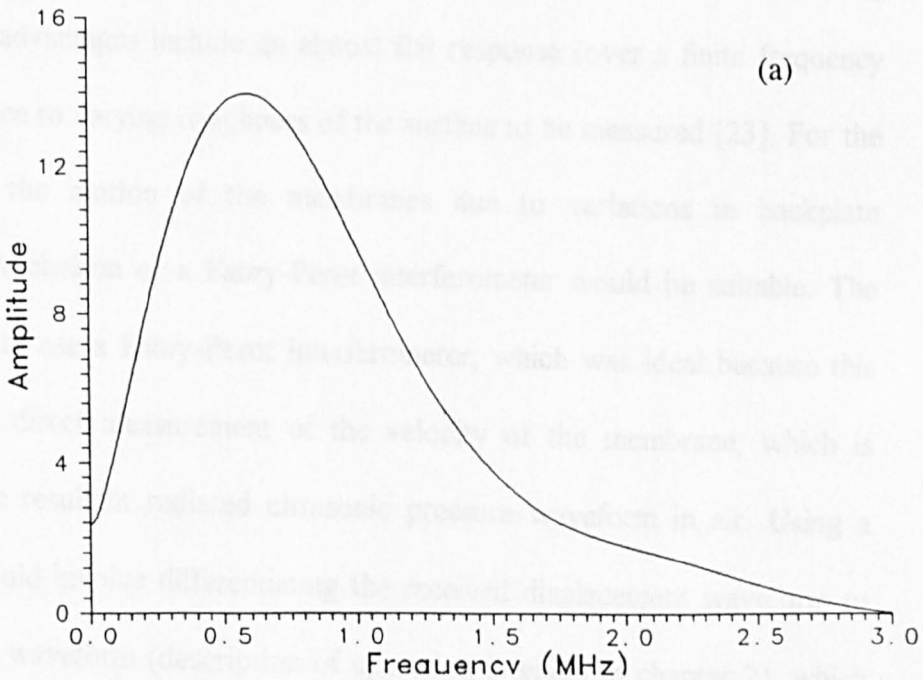

(a)

(b)

Figure 3.6, (a) Etched steel using an HCL etchant, (b) is the received spectrum.

higher charge concentration and the bottom of the holes having a greater attractive force on the membrane. This agrees with earlier studies for V-grooved backplates [7], where it was shown that a higher frequency response resulted from smaller hole depth and width.

3.4 Interferomic evaluation of the effects of the micromachined backplates.

Interferometers have several advantages over conventional methods for detecting ultrasound. Such advantages include an almost flat response (over a finite frequency range) and tolerance to varying roughness of the surface to be measured [23]. For the characterizing of the motion of the membranes due to variations in backplate characteristics, a Michelson or a Fabry-Perot interferometer would be suitable. The opportunity arose to use a Fabry-Perot interferometer, which was ideal because this instrument gave a direct measurement of the velocity of the membrane, which is proportional to the resultant radiated ultrasonic pressure waveform in air. Using a Michelson type would involve differentiating the received displacement waveform to obtain the pressure waveform (description of operation is given in chapter 2), which would increase noise. The interferometer, shown earlier schematically in figure 2.3(b), was used in the laboratories of Professor R.J. Dewhurst at the Department of Instrumentation and Analytical science, UMIST.

A series of backplates were produced by laser machining, each with varying hole diameters, depth and pitch. However, instead of mounting the backplate onto an aluminum SEM holder, the holes were machined onto the polished surface of the holder (eliminating the use of conducting epoxy). The dimensions of the holes in the backplate are shown in Table 3.2.

Backplate	Pitch μm	Diameter μm	Depth μm
A	100	50	50
B	200	50	50
C	100	80	50
D	100	50	10
E	Polished	-	-

Table 3.2

Laser etching offers fast accurate and inexpensive method for producing backplates, and as shown in section 3.3, laser machined backplates have a reasonable surface finish with well defined holes (sharp corners), which gave the best frequency response. Once the backplates had been machined, they were polished initially on a 6μm roughness grinding pad, then finally on a 0.5μm grinding pad (to remove any surface scratches).

The backplates were inserted in to the same transducer casing (the membrane and clamping pressure was not altered) and a 1KV bias voltage was applied across the

membrane (to apply the largest attractive force to obtain the maximum effect of the holes). A positive impulse driving signal was supplied from an AVTEC-1-C pulser.

3.4.1 Interferometer measurements

The transducers were placed in front of a Fabry-Perot interferometer, such that the incident laser beam was directed onto the center of the membrane. The transducers were arranged such that part of the reflection would enter in to a polarizing beam splitter and then into the interferometer. The laser beam was focused down to 1mm at at a power level of 20mW with a longitudinal wave length of 0.514μm. This was found to provide adequate reflection without damaging the membrane, and the reflected signal would contain information concerning the averaging effects of a number of holes. Although it was possible to focus the beam down to 80μm with reduced power, to isolate the response of a hole, practically, this was difficult to achieve in a known location on the backplate (i.e. whether it was over a hole or not). Thus, the waveforms correspond to an average over the 1mm diameter, which would contain a number of holes in each case. Each backplate was tested under identical conditions, and a waveform was recorded for each. The waveforms are presented for backplate A,B,C,D and E in Figures: 3.7(a), 3.8(a), 3.9(a), 3.10(a) and 3.11(a) respectively, and the corresponding frequency spectrums are shown in Figures 3.7(b), 3.8(b), 3.9(b), 3.10(b) and 3.11(b) respectively, the performances are summerised in Table 3.3.

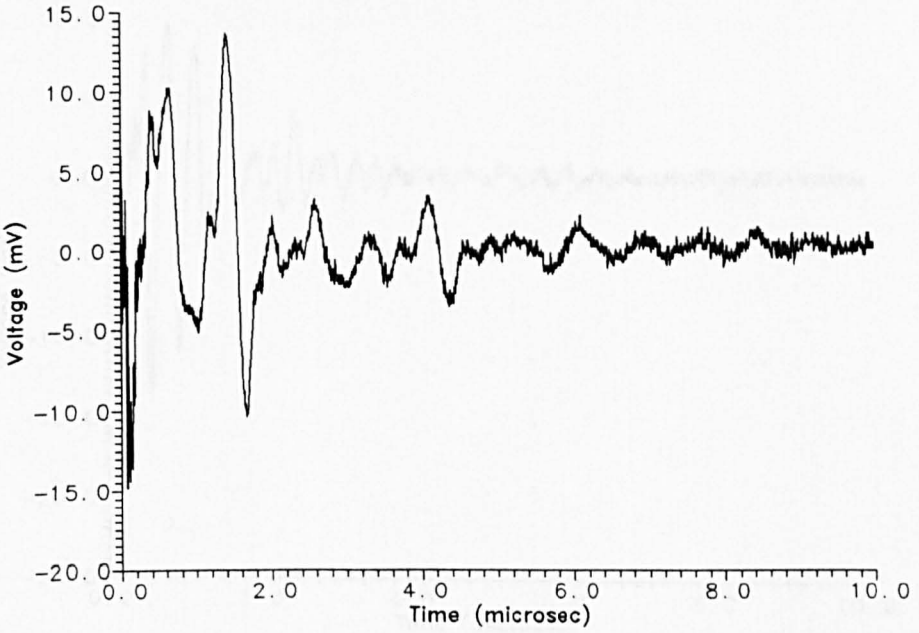

(a)

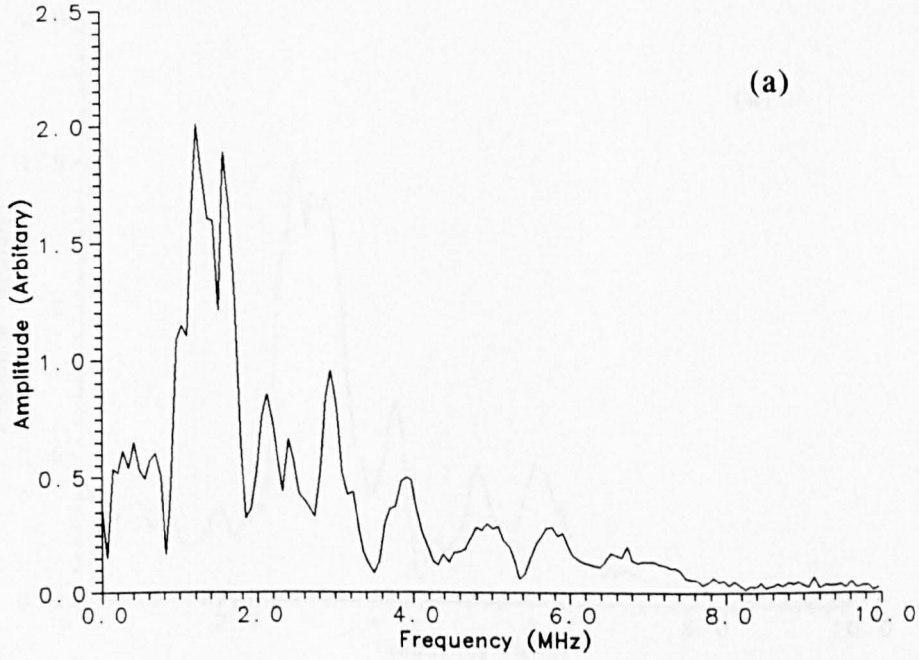

(b)

Figure 3.7, (a) Received waveform and (b) spectrum detected by a interferometer for a transducer fitted with backplate A.

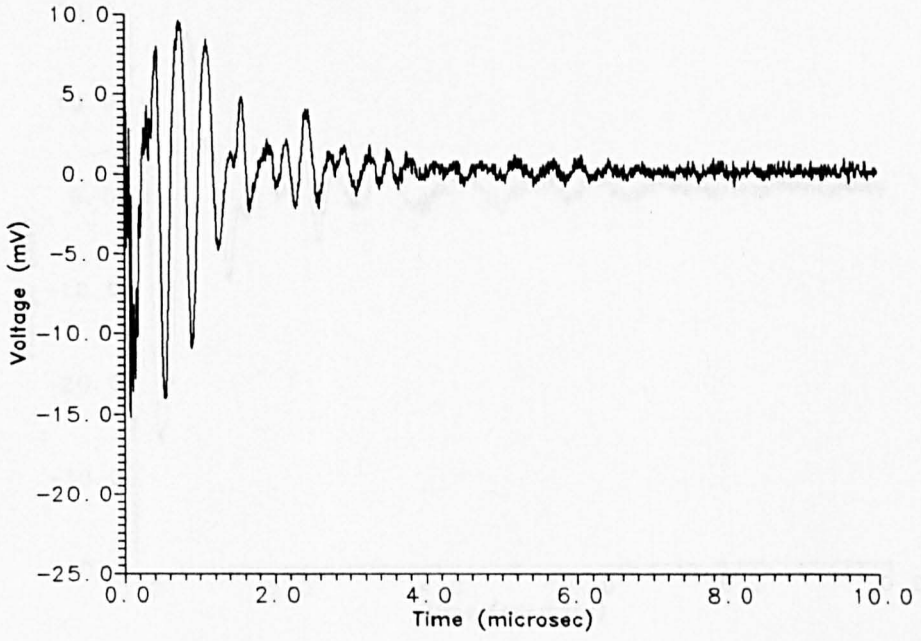

(a)

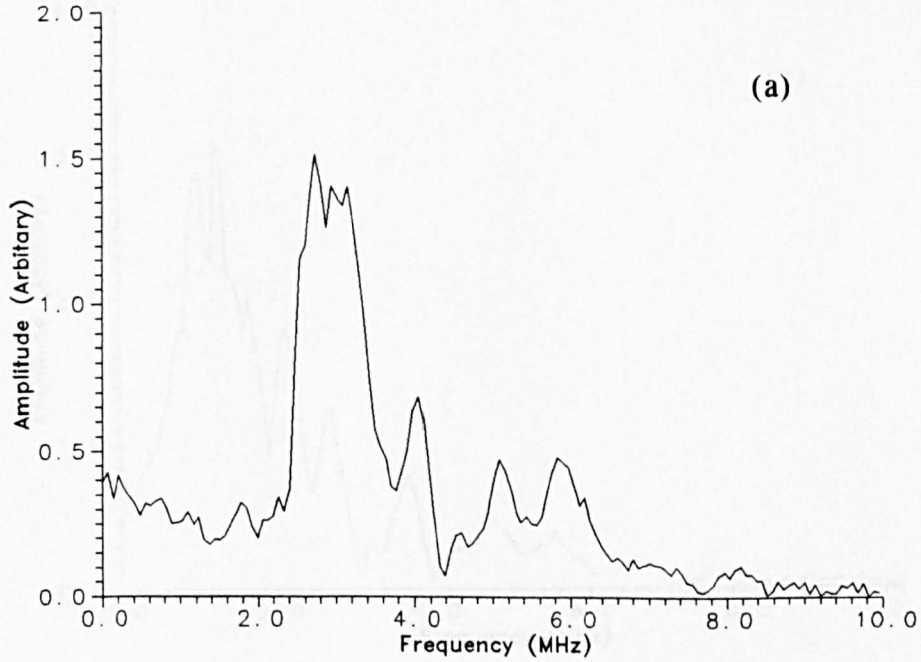

(b)

Figure 3.8, (a) Received waveform and (b) spectrum detected by a interferometer for a transducer fitted with backplate B.

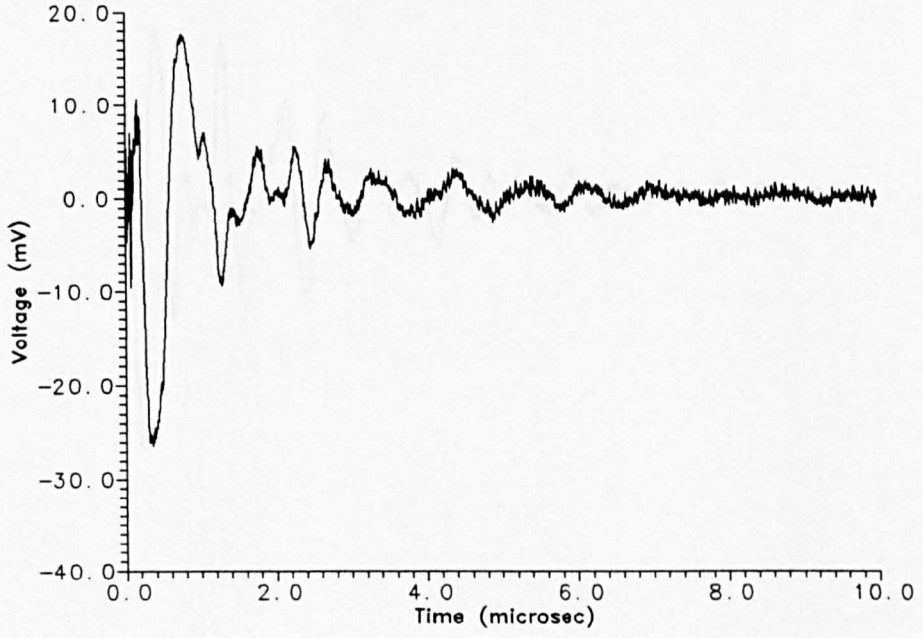

(a)

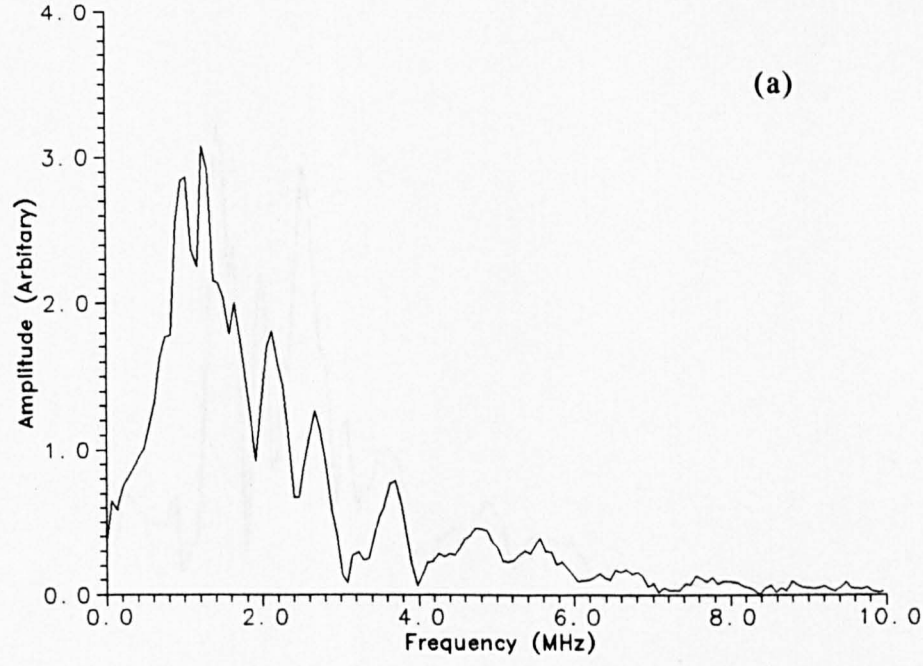

(b)

Figure 3.9, (a) Received waveform and (b) spectrum detected by a interferometer for a transducer fitted with backplate C.

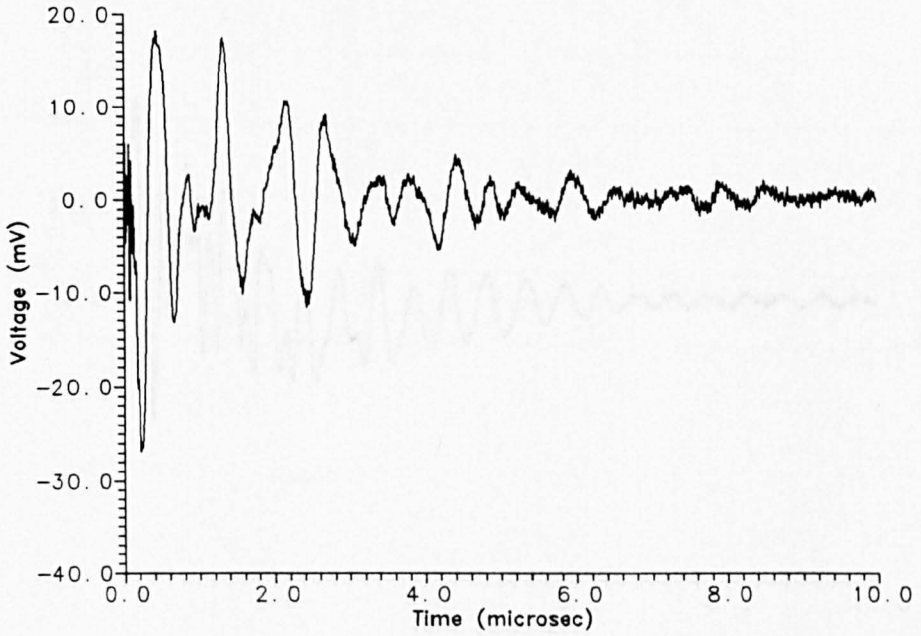

(a)

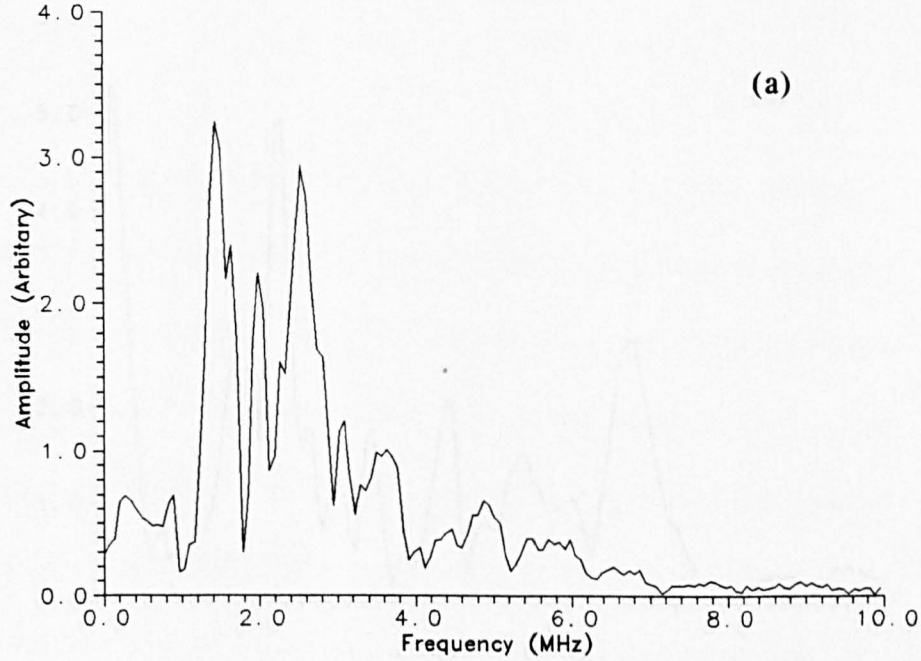

(b)

Figure 3.10, (a) Received waveform and (b) spectrum detected by a interferometer for a transducer fitted with backplate D.

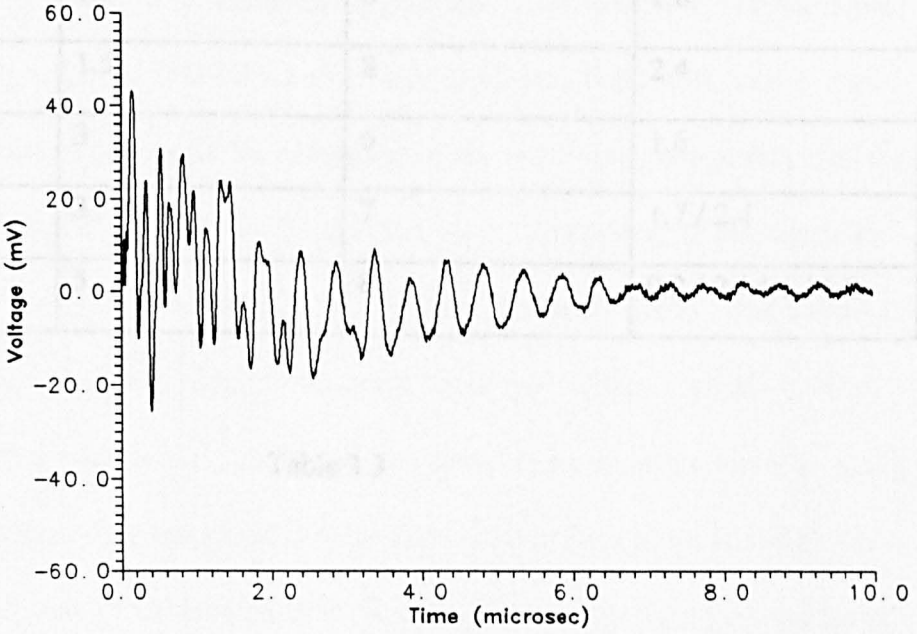

(a)

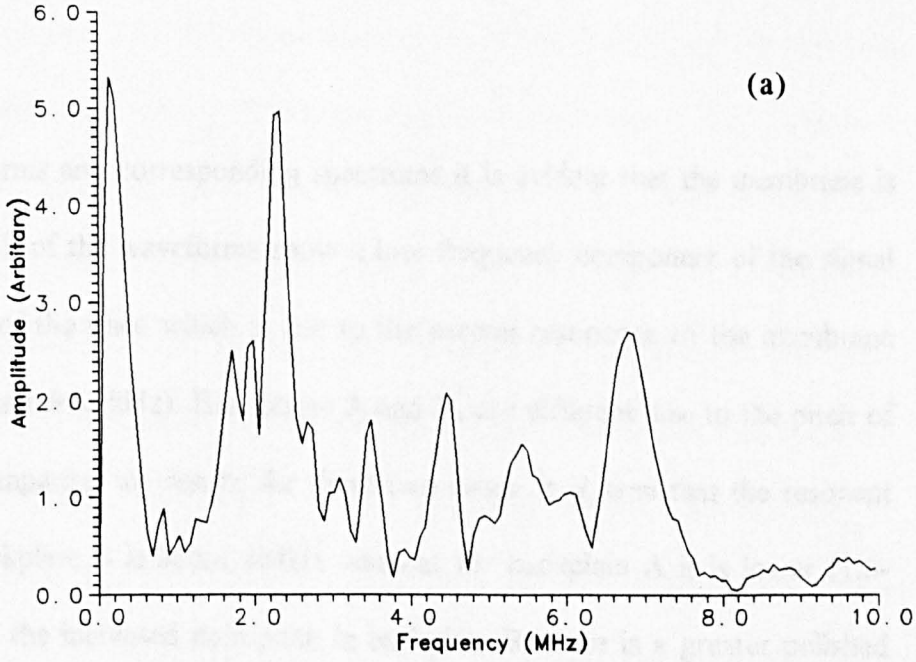

(b)

Figure 3.11, (a) Received waveform and (b) spectrum detected by a interferometer for a transducer fitted with backplate E.

Backplate	Signal Amplitude (arbitary)	Bandwidth (MHz)	Resonant Frequency(MHz)
A	1.9	8	1.6
B	1.5	8	2.4
C	3	6	1.6
D	3	7	1.7 / 2.4
E	5	8	0.2 / 2 / 4.1 / 6.8

Table 3.3

3.4.2 Discussion of results

From the waveforms and corresponding spectrums it is evident that the membrane is quite resonant. All of the waveforms show a low frequency component of the signal towards the end of the trace which is due to the natural resonance of the membrane (typically, a few hundred kHz). Backplates A and B, are different due to the pitch of the holes, and comparing the results for these two cases, it is seen that the resonant frequency for backplate B is about 3MHz whereas for backplate A it is lower (1.6-1.7MHz). Due to the increased hole pitch in backplate B, there is a greater polished area, and thus due to the small roughness (0.5μm) of the membrane, the shallow air pocket will account for the increase in the resonant frequency. However, there is a drop in the signal amplitude at resonance and frequencies below 2 MHz. If the results

from backplate C are compared to backplate A, the difference being that backplate C has a larger hole diameter, the spectrum for C shows a similar resonant frequency but the signal amplitude has been increased. Additionally, the sensitivity of the lower frequency response (below 1MHz) has also been increased. Both backplate A and C show a considerable reduction in the resonance of the membrane, suggesting that the pitch, and diameter of the holes has a large effect on the dampening of the membrane. Backplate D has the same dimensions as A, but with a reduced depth. The spectrum shows an increase in the resonant frequency, with two distinct peaks evident. Comparing this with backplate E (no holes, polished), again there are multiple peaks with one of the peaks being just above 2 MHz in the case of backplates B and E. Also, the signal from D was more damped than from E, again suggesting that the holes increase the damping of the membrane (as first discovered in earlier work [2]). As suggested by equation (3.3), the more shallow the holes, the higher the resonant frequency response of the device. Backplate E also demonstrates a highly resonant signal, but clearly from the waveform we can see the natural resonance of the membrane as a low frequency component at the end of the trace. Additionally, the spectrum for backplate E shows that the natural resonance of the membrane (first peak at 200kHz) is clearly distinguished from the other higher frequencies, this is mainly due to the lack of holes in the backplate, which are responsible for the low frequency characteristics (i.e. up to 2MHz) of the membrane and thus not easily resolved. Again backplate E had the largest signal amplitude because more of the membrane is situated closer to the backplate and thus the field between the electrodes is greater.

The received waveform for each backplate were repeated three times using the same equipment and alignment, and were found to be repeatable. Additionally, edge effects

were not present because the measurements were taken at the centre of the backplate. For the rest of the thesis, the laser machined backplate (C) fitted with a 5μm thick mylar membrane was used because it had the largest signal amplitude, little resonance and a bandwidth which was sufficient for the following chapters.

3.5 Electret membranes

An electret is a piece of material which is permanently polarised electrically. Generally, this polarisation is not affected by any external electric field (except in the case of a strong field). Typical electret materials are non-conducting such as organic wax and plastics [19]. Most industrial interest is with polymer materials such as Mylar or Kapton.

Electrets have the advantage of not requiring a d.c. bias voltage, constant sensitivity (over many years) and the ability to operate over a wide range of temperatures and humidity [20]. Polarisation of the membrane is typically done by heating the film to its softening temperature (for Kapton and Mylar this is about 150°C) and exposed to a d.c. bias of about 4KV. The voltage is supplied between two parallel plates with an air gap (2mm), the film is placed between the plates. After about 2 hours the film is left to cool slowly to room temperature and the film becomes polarised.

The polarisation can consist of hetero-charge and homo-charge [21]. Homo-charge is caused when the charge migrates from the film to the plates, thus leaving a net charge on the surface of the film with the same polarity as the applied field. The hetero-charge is formed by dipoles in the film orientating (by attraction) themselves such as to produce an opposite polarity to the applied field. Figure 3.12 shows the distribution of the hetero-charge and homo-charge.

The decay time of an electret is dependent on the volume resistivity. Ideally the resistivity needs to be high to produce a slowly varying polarisation material (i.e. the net charge is the difference between hetero-charge and homo-charge, ideally, the difference needs to remain constant). Initially for polymer films, the rate of decay of the charge is high, but after about a year the rate of decay is insignificant, and potentially has a useful life span (at room temperature) of a few thousand years.

An air-coupled capacitance transducer with a electret membrane was constructed, using a 5μm thick Mylar film which was heated to 150°C and left for two hours. The film was cooled to room temperature over a period of 8 hours with a 1KV bias voltage applied (throughout the cooling phase). The result was an electret membrane which was assembled into a capacitance transducer with a laser etched silicon backplate. The transducer was pulsed using a AVTEC-1-C pulser which produced a 0.1μs wide positive square wave at 350V. The receiver was the same device with a 2.5μm membrane connected to a Cooknell charge amplifier also supplying a 100V bias. The

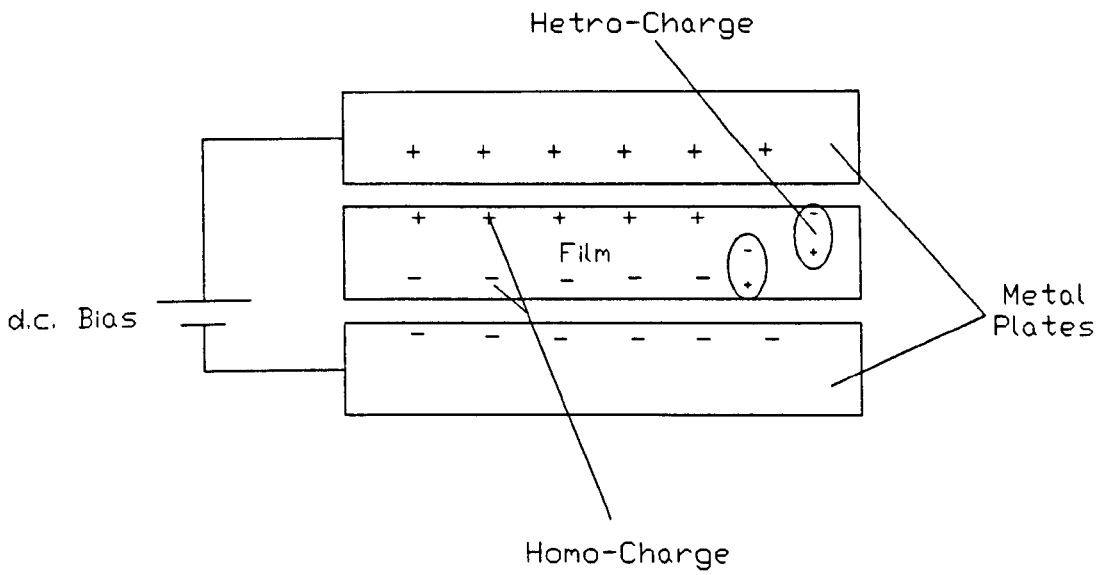

Figure 3.12, Polarisation process for electret film

receiver was placed at 28mm from the source and the resulting waveform is shown in Figure 3.13(a). From the received waveform we can see that the signal is inverted with respect to the waveform shown in chapter 2, suggesting that the charge on the film is opposing the applied driving voltage. The spectrum of the signal (Figure 3.13(b)) shows a bandwidth of about 1MHz and a peak response at about 700kHz. A qualitative measure of the charge was made by applying a positive d.c. bias across the membrane, which had the effect of opposing the permanent field across the membrane, thus causing the amplitude of the received signal to reduce. As the applied voltage increased, the signal reduced until it inverted and started thereafter to increase in amplitude. At the position where the signal amplitude is zero, the applied voltage was equal to the polarisation voltage of the membrane. Typically, for our electret samples the measured voltage was between 300-400V.

Electret films are ideal for use with capacitance transducers because they eliminate the need for an external bias supply. This opens up the possibility (because of the increased sensitivity and bandwidth) of connecting the transducer to standard pulse-echo equipment for imaging in air and water (see chapter 5). However, for the rest of the thesis electret transducers are not used because of their non-stable characteristics and low signal to noise ratio.

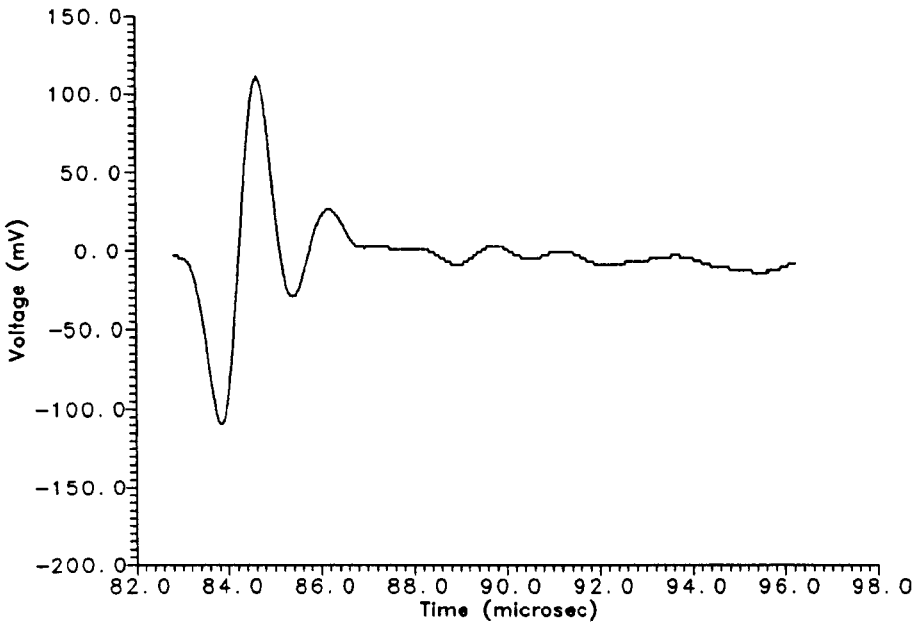

(a)

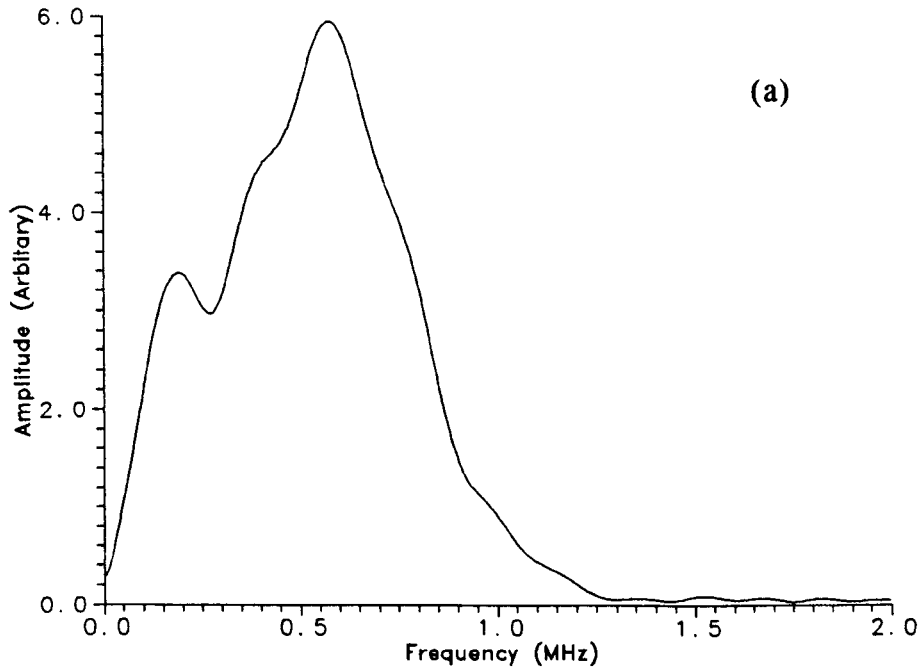

(b)

Figure 3.13, (a) Received waveform and (b) spectrum of a capacitance transducer with a 5μm thick Mylar electret membrane.

3.6 Conclusions

The diameter, depth and pitch of the holes has a significant effect on the emitted signal of the device. However, by adjusting any of these parameters the effects are not easily detectable in air because of the attenuation of high frequencies and the damping effect of the air. However, for immersion applications (where the attenuation and damping has a significantly smaller effect), and with the use of electret membranes, it would be possible to produce a highly sensitive, wide bandwidth capacitance transducer for pulse echo-applications (see chapter 5).

Part of this work had been presented at "Quantitative non-destructive Evaluation (QNDE)", University of Washington, Seattle, USA, 1995, and published as part of the conference proceedings [24].

3.7 References

[1] E.C. Wente "A condenser transmitter as a uniformly sensitive instrument for the absolute measurement of sound intensity", *Phys.Rev.* **10**, p39-63 (1917).

[2] W. Khul, G.R. Schodder and F.K. Schoder, "Condenser transmitters and microphones with solid dielectric for airborne ultrasonics", *Acustica* **4**, p519-532 (1954).

[3] K. Matsuzawa, "Condenser microphones with plastic diaphrams for airborne ultrasonics I", *J. Phys. Soc. Japan*, **13**, p1533-1543 (1958).

[4] K. Matsuzawa, "Condenser microphones with plastic diaphrams for airborne ultrasonics II", *J. Phys. Soc. Japan*, **15**, p167-174 (1959).

[5] J. Merhaut, "A combination to the theory of Electrostatic transducers based on the electrostatic principles", *Acoustica*, **17**, p283-293 (1967).

[6] G. Martin, Masters thesis, Canterbury, New zealand (1969).

[7] M. Rafiq and C. Wykes, "The performance of capacitive transducers using V-grooved backplates" *Meas. Sci. Tech*, **2**, p168-174 (1991).

[8] W.S.H.Munro, C.Wykes "Arrays for air-borne 100kHz ultrasound," *Ultrasonics*, **32 (1)**, 57-63 (1994).

[9] M.J.Anderson, J.A.Hill, C.M.Fortunko, N.S.Dogan, R.D.Moore "Broadband electrostatic transducers; modelling and experiments," *J. Acoust. Soc. Am.* **97**, 262-272 (1995).

[10] H.Carr, C.Wykes, "Diagnostic Measurements in capacitance transducers," *Ultrasonics*, **31**, 13-20 (1993).

[11] C.Wykes "Advances in air-coupled ultrasonics" (1995).

[12] K. Suzuki, K. Higuchi and H. Tanigawa, "A silicon electrostatic ultrasonic transducer," *IEEE Trans. Ultras. Ferr. Freq. Contr.* **36**, 620-627 (1989).

[13] M.I. Haller and B.K. Khuri-Yakub, "A surface micromachined electrostatic ultrasonic air transducer" *IEEE Ultrasonics Symp.* (Cannes), p1241-1244 (1994).

[14] D.W. Schindel, D.A. Hutchins, L. Zou and M. Sayer, "The design and characterization of micromachined air-coupled capacitance transducers", *IEEE Trans, Ultrason. Ferroelec. Freq. Contr.* UFFC-**42**, p42-50 (1995).

[15] H. Carr, "Electrostatic transducers for air-borne ultrasound" PhD thesis, University of Nottingham (1989).

[16] J. Hietanen, J. Stor- Pellinen and M. Luukkala, " A Helmholtz resonator model for an electrostatic ultrasonic air transducer with a V-grooved backplate", Sensors and *Actuators*, **39**, p.129-132,(1993).

[17] W.M.D. Wright, "Air-coupled ultrasonic testing of materials", Ph.D thesis, 1996.

[18] J. Hietanen, P. Mattila, J. Stor-Pellinen, F. Tsuzuki, H. Vaataja, K. Sasaki and M. Luukkala, "Factors effecting the sensitivity of electrostatic ultrasonic transducers", *Meas Sci. Technology*. **4**, p1138-1142 (1993).

[19] G.M. Sessler and J.E. West, "Electret transducers: a review", *J. Acoust. Soc. Am*, **53** No.6, p1589-1599, (1973).

[20] G.M. Sessler and J.E. West, "Foil-Electret Microphones", *J. Acoust. Soc. Am*, **40** No.6, p1433-1440, (1966).

[21] H.J. Wintle, "Introduction to electrets", *J. Acoust. Soc. Am*, **53** No.6, p1578-1588, (1973).

[22]M.M. Perlman, C.W. Reedyk, "Production and Charge Decay of film Electrets", *J. Electrochem. Soc*: Solid state science, Electret Symposium, Oct, 15-19, Abstract 133, p 43-49,(1967).

[23] Q. Shan, C.M. Chen and R.J. Dewhurst, "A conjugate optical confocal Fabry-Perot interferometer for enhanced ultrasound detection". *Meas. Sci. Tec.*, **6**, p921-928, (1995).

[24] A.G. Bashford, D.A. Hutchins and D.W. Schindel, "Response for an air-coupled ultrasonic transducer for various backplate and apertures", Proc. **15A** 1995, QNDE Conf. (Seattle), USA.

CHAPTER 4

PRESSURE FIELD VARIATIONS OF A MICRO-MACHINED AIR-COUPLED ULTRASONIC TRANSDUCER

4.1 Introdution

The ultrasonic field from a transducer is often the feature that limits the performance of an ultrasonic system. If the field pattern is unknown, this can lead to difficulties in retrieving information from the medium under investigation. As micromachined devices can be constructed with reproducible responses [1], it is possible to study the radiated fields and waveforms for different drive waveforms and external apertures. The aim of the chapter is thus to compare the peak sound pressure field of a micromachined silicon backplate capacitance transducer to that predicted by theory for a plane piston, and to extend this to transducer configurations (an annulus and a zone plate) which increase axial responses in air, for different voltage drive signals. The ability to characterise the pressure field of a transducer has importance in many ultrasonic applications [2], especially for focused transducers which has the advantage of enhanced imaging resolution.

The field variations in front of a transducer have been determined theoretically by using different techniques developed over the past 60 years, and thus have been extensively reviewed [3]. The first mathematical prediction made use of the Rayleigh surface integral solution [4] to define the velocity potential which is physically a statement of

Huygens principle (i.e. for a plane vibrating surface, every point on the surface is a source of spherical wavelets and the field at every point is the superposition of these wavelets). However, new solutions were later devised for the velocity potential by manipulating the geometry and co-ordinate system of the original Rayleigh integral [5,6]. Conventional techniques to compute the pressure field variation for a circular piston with transient excitation [7-9] use a velocity impulse response which defines the system for wide bandwidth, and this is convolved with a simulated velocity response of the piston. The field can be described in terms of two components: a plane wave from the source, and an inverted wave from the edge (referred to as the 'edge' wave). Edge waves are diffracted from the aperture or at the boundaries of the source, and travel towards the axis of the transducer, thus interfering with the plane wave.

The peak pressure variations in air for any size of aperture can be predicted, using established theory for the radiated field of a plane piston transducer [7-9]. The mathematical model assumes that the pressure at any point across and away from the transducer face can be computed from the interference of the plane and edge components, and also assumes that the front face is vibrating with a uniform amplitude and phase (although variations in these parameters can be included if required). The relevant expression for the time-dependent velocity potential at any given observation point in a half space can be derived, and further details can be found in the quoted publications. Briefly, the velocity potential impulse response $\Phi(M,t)$ of a plane piston can be written as a combination of plane and edge wave components:

$$\Phi(M,t) = c|A|\mathbf{H}(t-t_0) + (c/2\pi)\Omega(ct)\mathbf{H}(t-t_1)\mathbf{H}(t_2-t) \qquad (4.1)$$

(Plane wave) (Edge wave)

where M is the observation point, c is the longitudinal wave velocity, t is time, t_1 and t_2 are as defined below, and **H** is the Heaviside step function. The value of |A| in the plane wave component depends on the field position. For M opposite the front face the value is 1. For a field position such that x=a, the value drops to 1/2, and |A| is zero at greater radial (x) distances, i.e. beyond the physical edge of the transducer. The time taken for an edge wave to reach the observation point from the closest and furthest edge of the piston is given by t_1 and t_2 respectively. In the case of a circular piston, $\Omega(ct)$ represents the angle of equidistant arc which is an analytical expression derived for the edge wave diffraction impulse response [7-9], and is given by:

$$\Omega(ct) = 2\cos^{-1}\{[(ct)^2-z^2+x^2-a^2]/2x[(ct)^2-z^2]\}, \qquad (4.2)$$

where a is the piston radius, x is the radial distance from the centre, and z is the axial distance from the piston. The arrival times t_0 (for the plane wave), t_1 and t_2 are given by:

$$t_0 = z/c, \qquad (4.3)$$

$$t_1 = \{(a-x)^2+z^2\}/c, \qquad (4.4)$$

$$t_2 = \{(a+x)^2+z^2\}/c. \qquad (4.5)$$

The pressure impulse response $S(M,t)$ for an arbitrary point M is defined as the differential of the velocity potential impulse response, i.e.

$$S(M,t) = \rho_0(\delta\Phi/\delta t)(M,t), \qquad (4.6)$$

where ρ_0 is the density of the medium. Equation (4.6) is only valid for values of t which are greater than or equal to t_0 and less than or equal to t_2; elsewhere $S(M,t) = 0$. The actual pressure waveform $P(M,t)$ is then obtained by convolving the simulated motion of the piston (ie., the velocity waveform $v(t)$) with the pressure impulse response for each spatial point:

$$P(M,t) = v(t) * S(M,t). \qquad (4.7)$$

where P(M,t) is the pressure response.

An additional factor is attenuation, which causes amplitude degradation and phase shifting. This can be high in air at ultrasonic frequencies, and so this factor needs to be incorporated into the model. The effect can be predicted using previous studies [10,11] and recent work has produced an experimentally-derived expression [12] used here, which is:

$$\sigma = 15.895X10^{-11}(T/T_0)^{1/2}f^2/(P/P_o) \qquad (4.8)$$

where σ is the peak sound pressure attenuation per meter (dB/m). The numerical constant in eq.(4.8) is an experimentally measured value, determined at a constant temperature of 25°C [12] and f is the frequency (Hz). T is the measured temperature, T_o is the reference temperature, P is the measured pressure, and P_o is the reference pressure. In the present work, T and P are taken as the standard reference values (25^0C and 101.325kpa respectively), and thus both T/T_o and P/P_o are unity. The attenuation was calculated at each field position by taking the Fourier transform of the predicted waveform, to give a frequency spectrum of the signal. This was then modified according to the expression for the calculated attenuation σ, so that the higher frequencies were suppressed more than the lower frequencies. An inverse Fourier transform then gave the resultant attenuated waveform. The resultant spatial variations were found as before by taking the peak to peak amplitude of the signal. Note that low humidity levels (30%) were maintained throughout the experiments; while water vapour is known to affect attenuation, its effect is small at high frequencies [13].

To obtain the required theoretical velocity waveform of the vibrating membrane of the capacitance transducer (v(t) in eq-(4.7)) it was assumed that a small d.c. polarised component is always present on the membrane; thus, we can assume the devices have a linear response [14] (i.e. the force is proportional to the drive voltage and hence the displacement). A pulser was used to provide a square wave with a 0.15μs rise time and a width of 0.7μs as the driving signal. This was band-pass filtered between 100 and 800kHz (typical bandwidth for a source with a small d.c bias), and the velocity waveform hence obtained by the differential with respect to time of the drive

waveform. The predicted velocity waveform is shown in Figure 4.1(a), and was used as $v(t)$ in the above theoretical predictions.

The predicted theoretical sound pressure waveform at an axial distance of 15mm is shown in Figure 4.1(b). This may be compared to the experimental waveform of Figure 4.1(c), detected by the miniature scanned detector at the same position, where reasonable agreement with theory is evident.

4.2 Apparatus and experiment

The pressure waveforms throughout the spatial field of micromachined capacitance transducers (as used in chapter 3) were measured in air using a scanned miniature hydrophone (0.1 - 2MHz response). The source transducers under test were derived from a device with a polished flat silicon backplate containing 40μm diameter etched cylindrical pits of 40μm depth [15] fitted with a 5μm Mylar polymer membrane, and which had a 10mm diameter active area. They were fitted with a grounded brass case, as described in [15], where additional detail of construction can be found. The scanned receiver was made in the same way, but was fitted with a 1mm diameter aperture to define a limited detection area. Although bandwidths in excess of 2MHz were available for both source and receiver, source driving frequencies were restricted to an upper limit of 700kHz, where the wavelength in air is approximately 0.47mm. Hence, at the upper frequency limit, the detector is approximately two wavelengths in diameter. In the experiment illustrated in Figure 4.2, the apertured receiver was scanned over a two dimensional horizontal plane throughout the field of the radiating transducer (the x-z

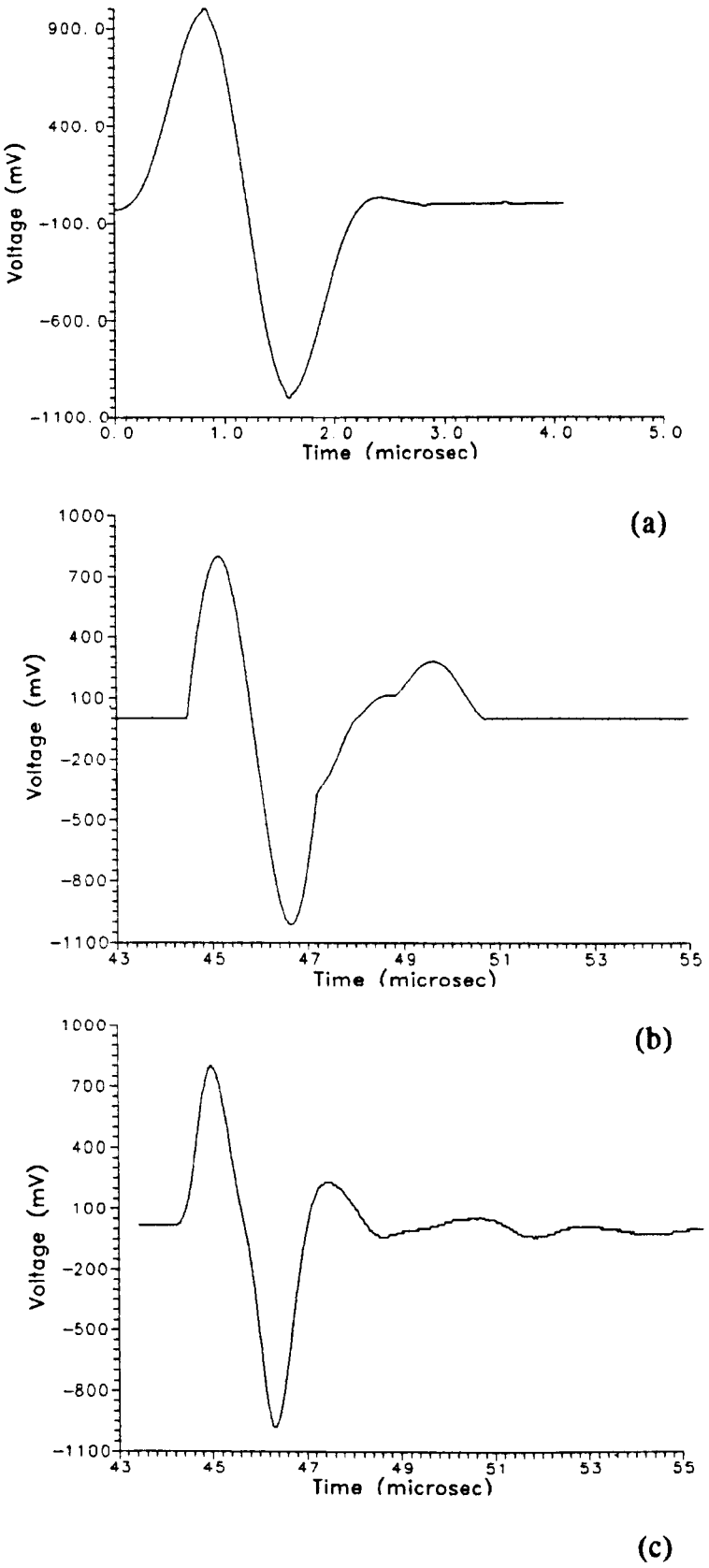

Figure 4.1. (a) Predicted velocity waveform of the membrane. (b) Theoretical and (c) experimental sound pressure waveform, at Z=15.

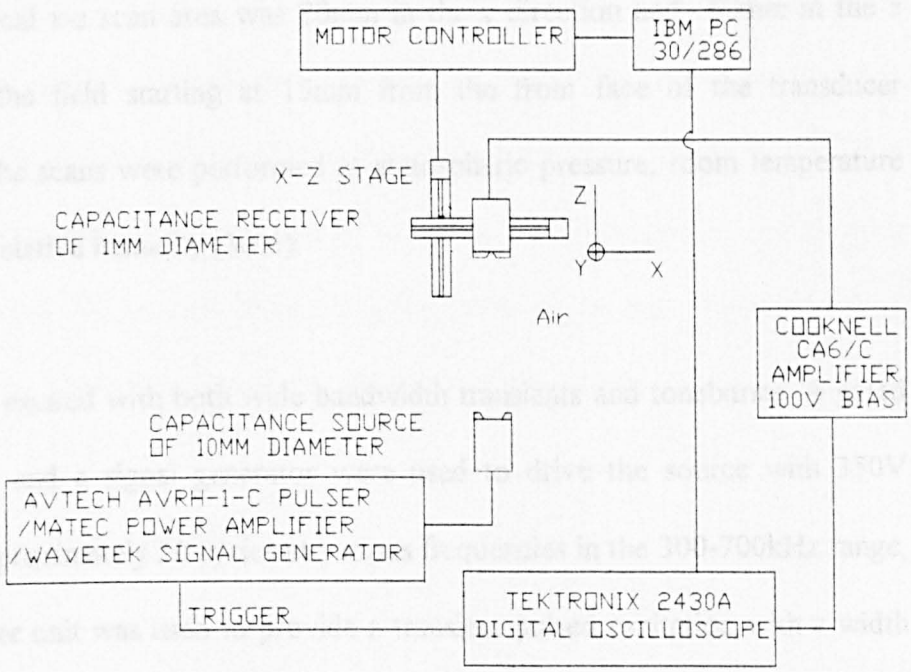

Figure 4.2. Schematic diagram of the scanning system used.

plane), with the source radiating horizontally along the z axis. Scanning was achieved using a computer-controlled system which consisted of a PC, controlling a digital oscilloscope and a motor controller, the latter driving two linear stages (one for each axis). Each stage was fitted with a synchronous stepping motor having 400 steps per revolution giving an absolute resolution of 0.005mm and a positional accuracy of $\pm$0.004mm / 50mm of travel for the system. The scans were performed with a 0.5mm spatial resolution in the x (radial) direction and a 1mm resolution in the z (axial) direction. A typical x-z scan area was 20mm in the x direction and 50mm in the z direction, with the field starting at 15mm from the front face of the transducer membrane. All the scans were performed at atmospheric pressure, room temperature (20°C) and low relative humidity (30%).

The source was excited with both wide bandwidth transients and tonebursts. A gated power amplifier and a signal generator were used to drive the source with 350V tonebursts of approximately 20 cycles at various frequencies in the 300-700kHz range, whereas an pulser unit was used to provide a transient pulsed excitation with a width adjustable from 0.1-10μs. The signal produced by the 1mm apertured receiver was sent to a charge sensitive amplifier with a gain of 5mV/pC, which also supplied a 100V bias between the backplate and the membrane of the receiver. The nominal capacitance of the device was 650pF. The signal waveform at each field position was digitised using a digital oscilloscope, and stored on the PC. The peak sound pressure variations were obtained from stored waveforms by taking the maximum peak to peak amplitude of the signal at each designated point.

Peak sound pressure spatial variations were now measured for a 10mm diameter plane piston, using a 350V drive pulse from the pulser unit. The driving pulse width was varied to give a plane wave pressure component close to the transducer face in the form of a bipolar square wave pulse of variable width, and hence with a predetermined centre frequency. The experimental and variations in peak sound pressure waveform amplitude throughout the whole scanned field are presented in Figure 4.3(a) for a drive excitation with the frequency centred at 318kHz. The pulser was tuned to give the transducer a resonance of about 300kHz because of the reduced amount of signal averaging and also gives a few millimeters in the near fied region to pick up the edge waves in the nearfield region. Remembering that this started 15mm from the front face of the vibrating membrane, the remnants of the edge wave component can be seen clearly at the top left (i.e. at small axial (z) values), converging onto the axis to form the axial maximum by interference with the plane wave component.

4.3 Results and comparison to theory

The predicted theoretical peak sound pressure variations in air for a plane piston were now calculated using equations (4.1)-(4.8), to compare to the experiment, the results being shown in Figure 4.3(b) for the same scan area of 40mm x 20mm. Good agreement is evident, with the nearfield/farfield boundary positioned at the axial distance of approximately 24mm, as expected from the quoted centre frequency.

The above field plotting experiments were now repeated for toneburst excitation (15 cycles), using the gated power amplifier to drive the transducers with a tone voltage

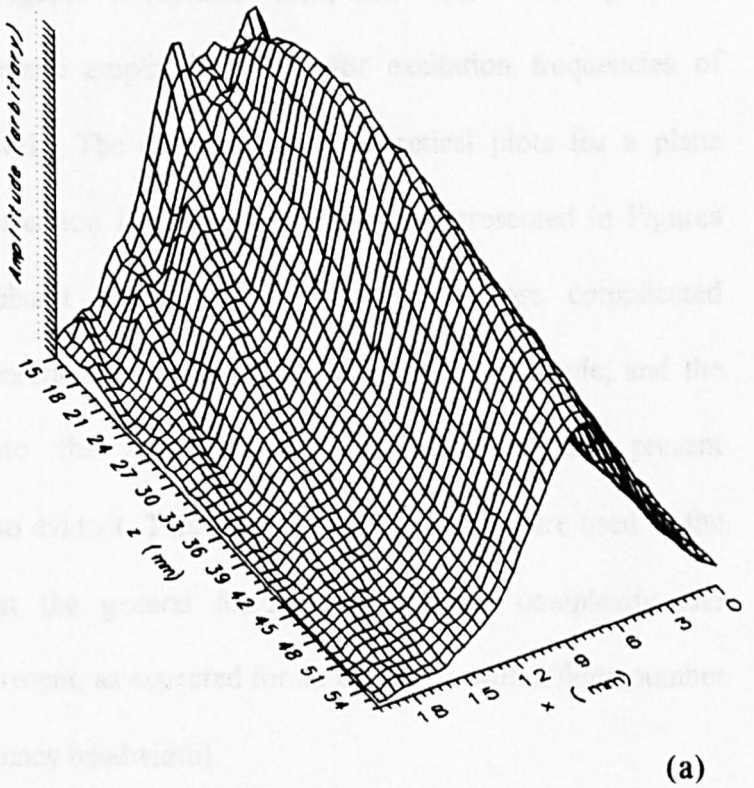

(a)

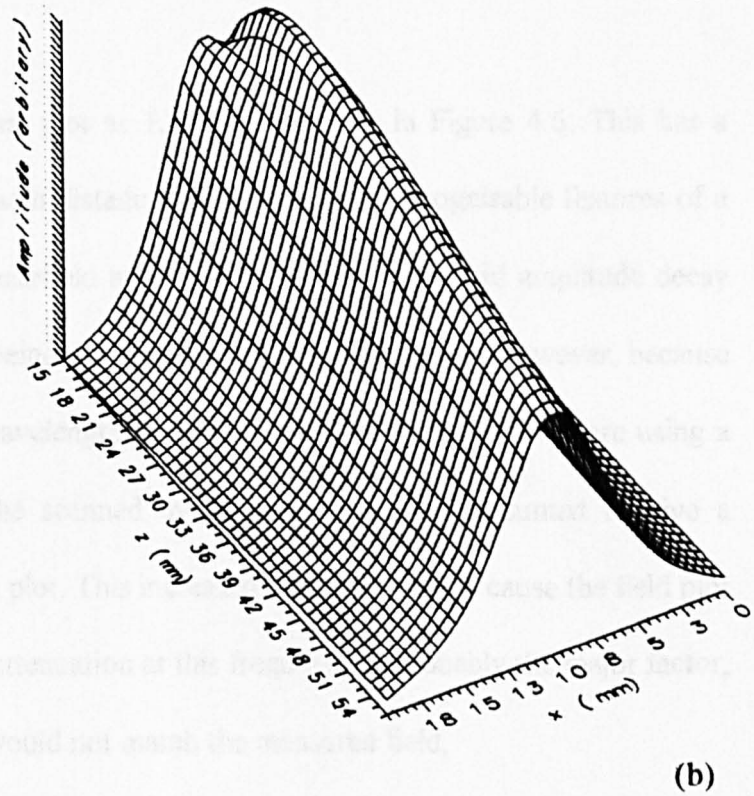

(b)

Figure 4.3. (a) Experimental peak sound pressure variations, (b) theoretical peak sound pressure variations, for a plane piston driven by a pulse centred at 318kHz.

signal containing 15 cycles. Figures 4.4(a) and 4.5(a) show the resulting spatial variations in peak sound pressure amplitude in air, for excitation frequencies of 500kHz and 700kHz respectively. The corresponding theoretical plots for a plane piston, again including the correction for attenuation, are also presented in Figures 4.4(b) and 4.5(b). For toneburst generation, the fields are more complicated theoretically, with marked theoretical axial variations in nearfield amplitude, and the edge waves converging onto the axis. While some variations are present experimentally, these are not so evident. This is due to the finite aperture used in the receiver. Note, however, that the general features of nearfield complexity and increased side lobe levels are present, as expected for an excitation with a finite number of cycles (i.e. a narrower frequency bandwidth).

For completeness, an additional plot at 1.5MHz is shown in Figure 4.6. This has a much faster amplitude decay with distance, but still has the recognisable features of a converging edge wave, and nearfield interference effects. This rapid amplitude decay is due to several factors, one being the increased attenuation in air. However, because of the fact that the radiated wavelength is approximately 0.22mm, and we are using a detector aperture of 1mm, the scanned hydrophone cannot be assumed to give a wholly representative pressure plot. This increased directivity could cause the field plot to decay artificially, although attenuation at this frequency is probably the major factor, and thus the theoretical field would not match the measured field.

The well-behaved nature of the emitted beam can be illustrated further by scanning in a plane perpendicular to the beam axis (i.e. in the X-Y plane). This is done in the

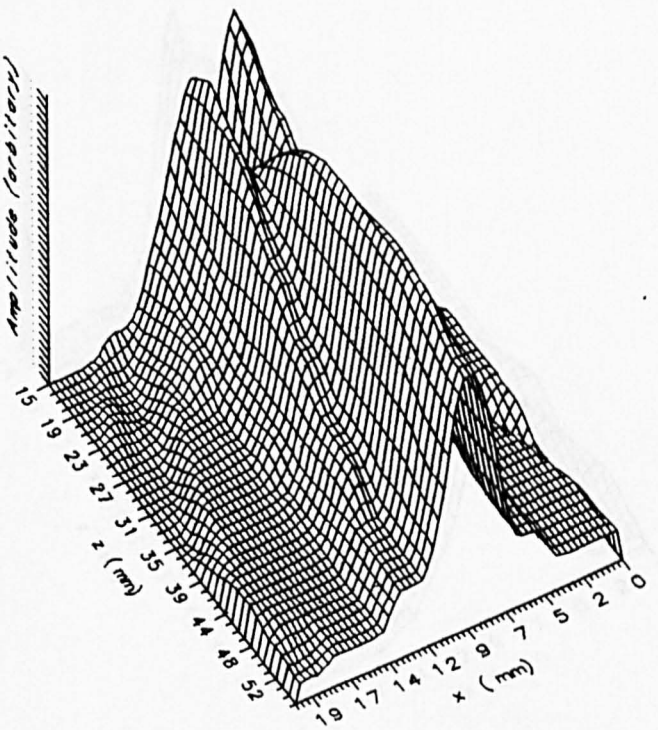

(a)

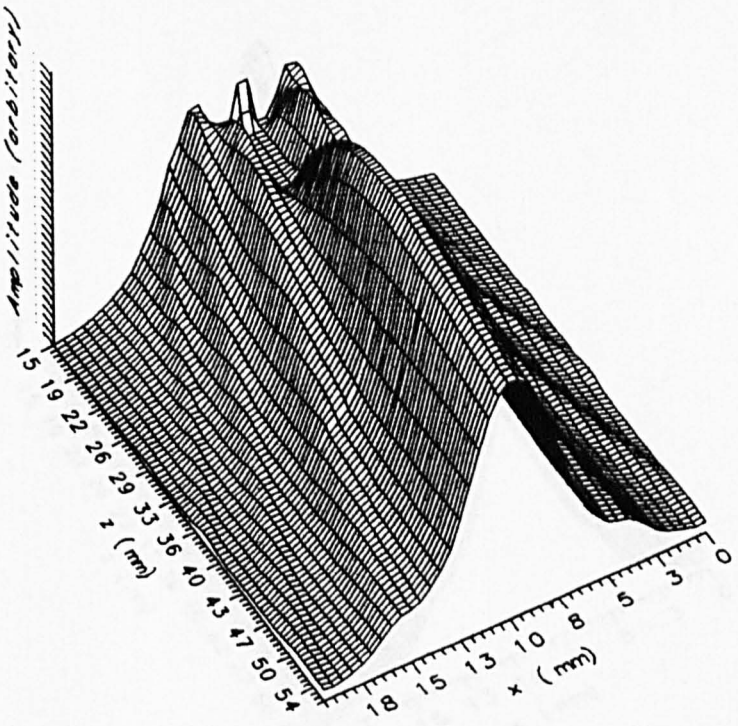

(b)

Figure 4.4. (a) Experimental peak sound pressure variations, (b) theoretical peak sound pressure variations, for a plane piston driven by a 500kHz toneburst.

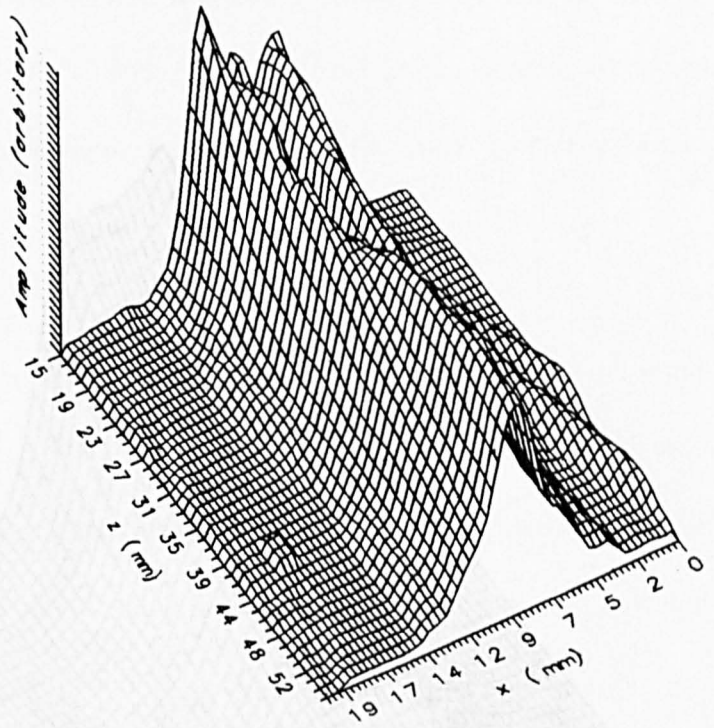

(a)

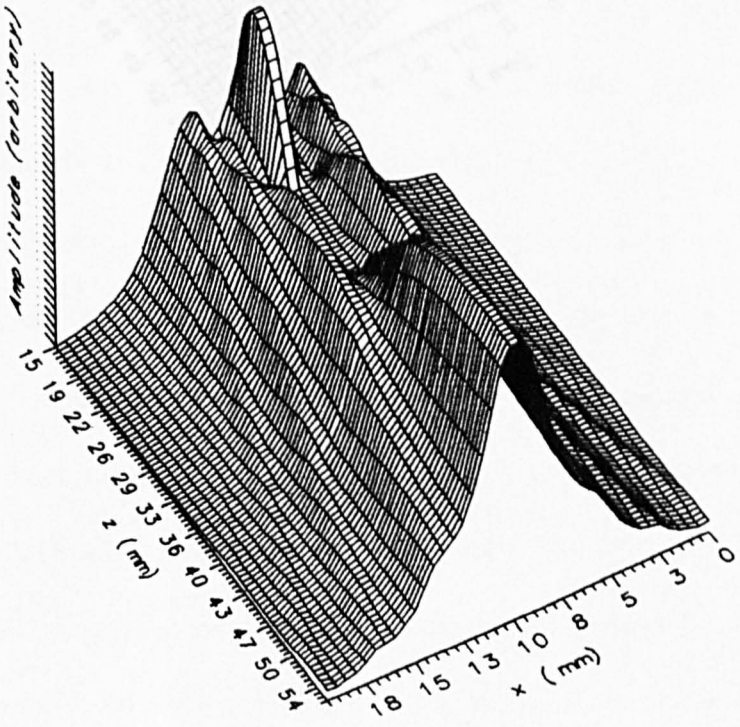

(b)

Figure 4.5. (a) Experimental peak dound pressure variations, (b) theoretical peak sound variations, for a plane piston driven by a 700kHz toneburst.

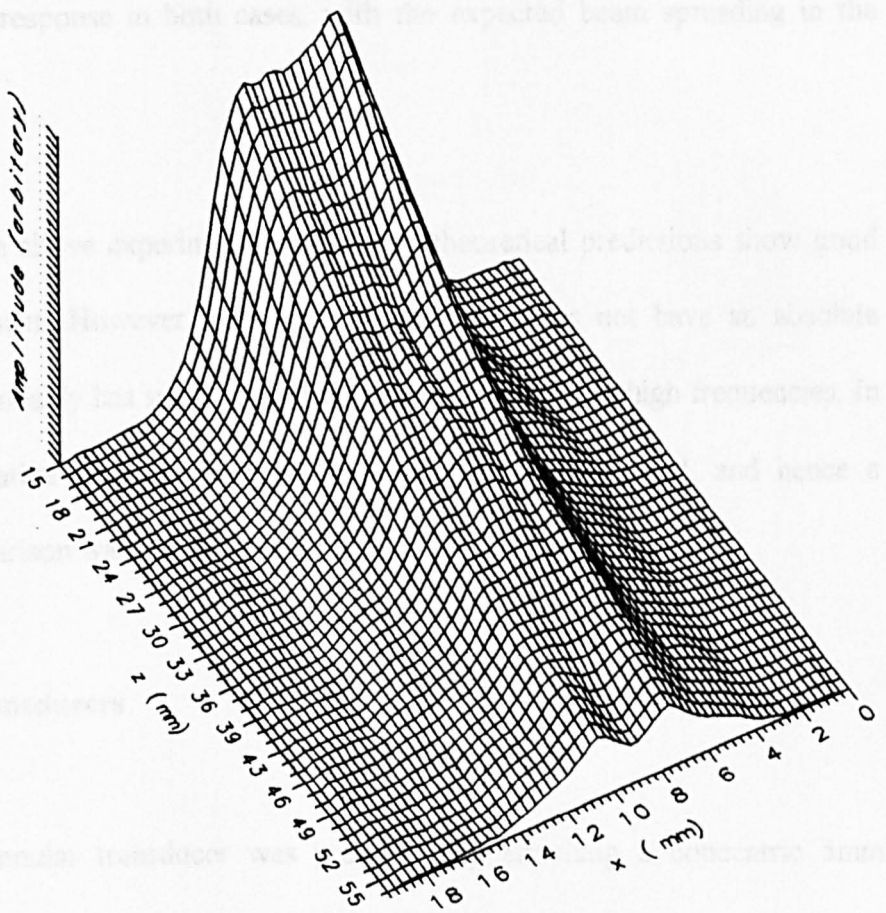

Figure 4.6. Experimental peak sound pressure variations for a plane piston driven by a 1.5MHz toneburst.

nearfield region for pulsed excitation centred at 500kHz, 15mm axially from the source (Figure 4.7(a)), and at a distance of 50mm (Figure 4.7(b)) in the farfield. Note the relatively smooth response in both cases, with the expected beam spreading in the farfield.

Comparison of the above experimental scans with theoretical predictions show good qualitative agreement. However, the miniature detector does not have an absolute calibration, and probably has some directivity effects of its own at high frequencies. In addition, only relative peak sound pressure amplitudes were plotted, and hence a quantitative comparison was not attempted.

4.3.1 Annular transducers

An air-coupled annular transducer was produced by attaching a concentric 5mm diameter paper disk to the centre of the 10mm diameter membrane (i.e. a small disk fitted inside the aperture). This absorbed radiated output over the 5mm diameter central area, producing an annulus with an active inner diameter (d) of 5mm and an outer diameter (D) of 10mm. The peak sound pressure field for this annulus was determined experimentally (as described above) for pulsed excitation, giving a signal with a centre frequency of 318kHz. The results are shown in Figure 4.8(a). Note the tendency for axial focusing, with a gradual increase in axial amplitude towards the maximum, accompanied by a smooth decrease in the direct radiation from the active area of the annulus. Similar features are seen in the theoretical plot, Figure 4.8(b). This was produced by predicting the waveforms produced at each field point by two

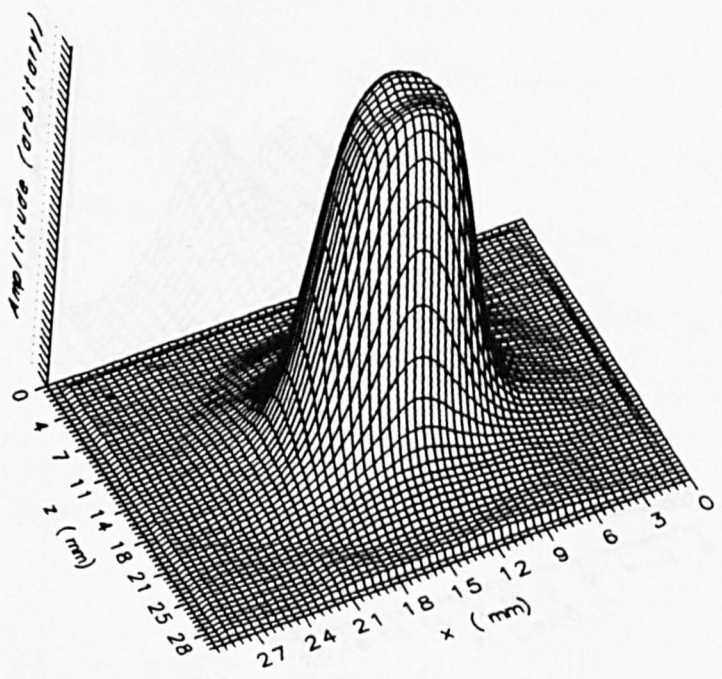

(a)

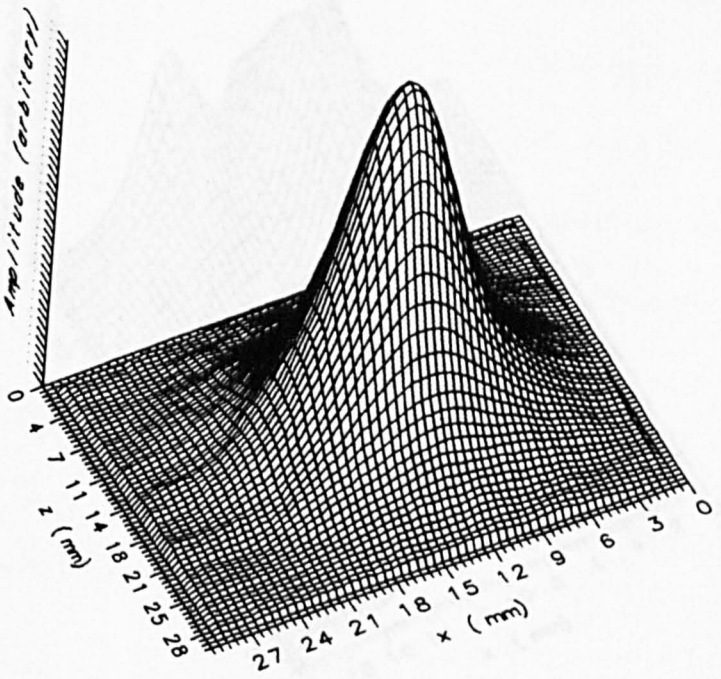

(b)

Figure 4.7. Experimental peak sound pressure variations for a plane piston transducer at 318kHz in the X-Y plane, (a) 15mm, (b) 50mm from the source

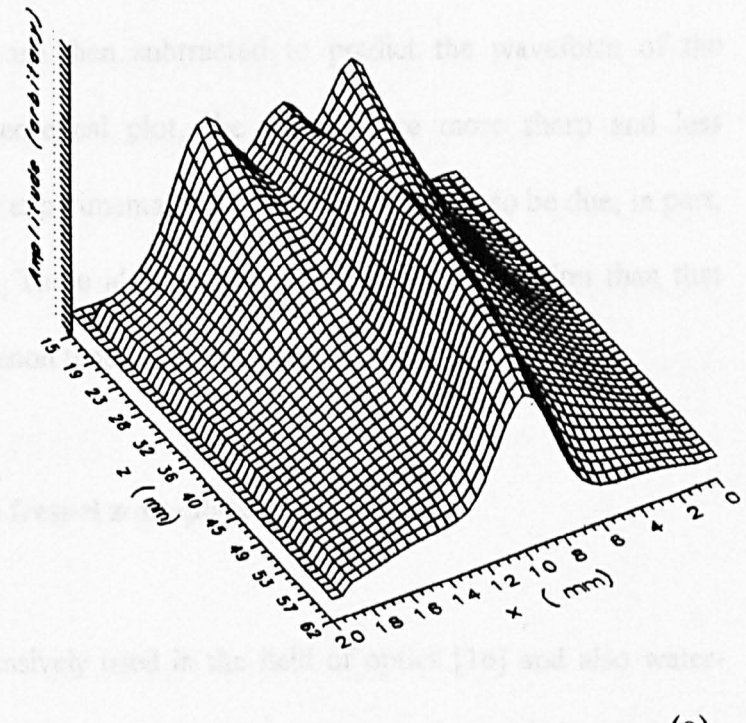

(a)

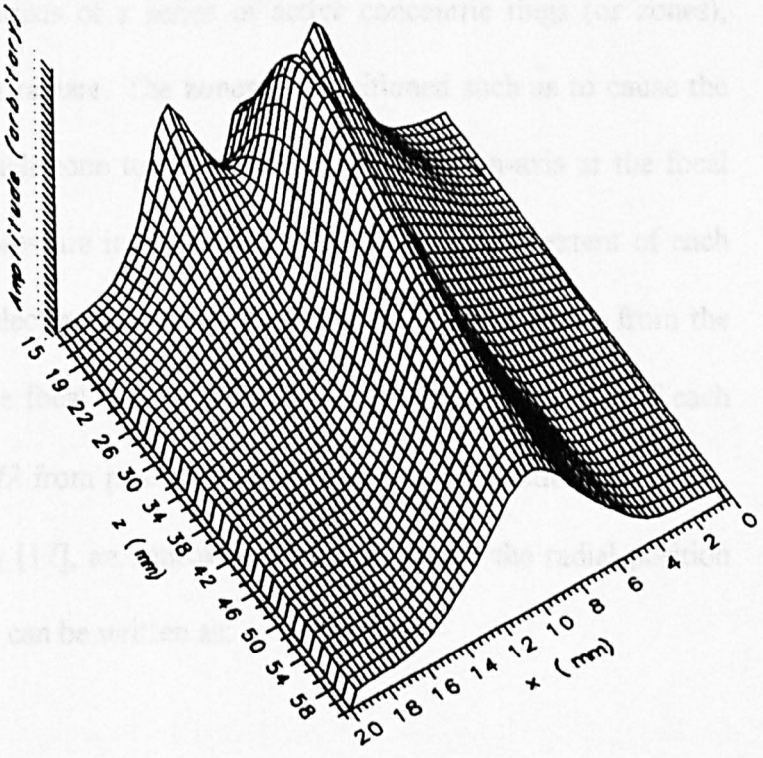

(b)

Figure 4.8. (a) Experimental peak sound pressure variations for an annulus, (b) theorectical peak sound pressure variations for an annulus, using a pulse centred at 318kHz (d=5mm D=10mm).

separate plane pistons, one of 10mm diameter and the other of 5mm diameter. At each spatial point, the waveforms are then subtracted to predict the waveform of the annulus. Note that in the theoretical plot, the features are more sharp and less attenuated than those observed experimentally. This is again thought to be due, in part, to the finite receiver aperture. There also seems to be greater attenuation than that predicted by theory, a phenomenon that merits further investigation.

4.3.2 Transducers fitted with fresnel zone-plate

The Fresnel zone-plate is extensively used in the field of optics [16] and also water-coupled ultrasonic transducers [17], but has not been used on air-coupled capacitance transducers. A zone plate consists of a series of active concentric rings (or zones), separated by areas that do not radiate. The zones are positioned such as to cause the radiated contributions from each zone to interfere constructively on-axis at the focal position, thus increasing the pressure intensity at the focus. The radial extent of each zone (R_M) is determined by selecting the required axial focusing position Z_0 from the face of the zone plate (i.e. the focal length), and then positioning the edge of each zone to be at a distance $Z_0+M\lambda$ from position Z_0 where λ is the acoustic wavelength, and M=1,3,5,7... As shown by [17], an approximate expression for the radial position of the edges of each zone (R_M) can be written as:

$$R_m = \sqrt{\frac{M\lambda}{2}(Z_0 + \frac{M\lambda}{8})} \qquad (4.9)$$

The equation results by assuming the wave emanating from the mth zone boundary will arrive at the focal point with a $m\lambda/4$ phase shift relative to the wave emanating from the origin of the zone-plate. Note, the zone-plate is a 'wavelength device', in that once the focal length z_o is chosen, the focusing performance will depend on the wavelength of the incident plane wave (i.e. a wavelength of 680μm will have the same focusing performance in air and water, 500kHz and 2.25MHz respectively). Using equation (4.9) to design a zone-plate that focusses at 7.5mm with a 500kHz input plane wave, the dimensions (innermost to outermost) are shown in Table 4.1:

Radii	Dimension (mm)	Radii	Dimension (mm)
r_1	1.606	r_{13}	6.167
r_3	2.812	r_{15}	6.690
r_5	3.670	r_{17}	7.190
r_7	4.389	r_{19}	7.674
r_9	5.029	r_{21}	8.142
r_{11}	5.617	–	–

Table 4.1

Figure 4.9 shows a schematic diagram of a zone plate with 6 zones, with a predicted focal length from equation (4.9) of 7.5mm when driven at a frequency of 500kHz in air. The radii R_1, R_3 etc. are shown on the Figure, with the unshaded areas representing regions where there is radiation; elsewhere, it is assumed that no emission occurs. The

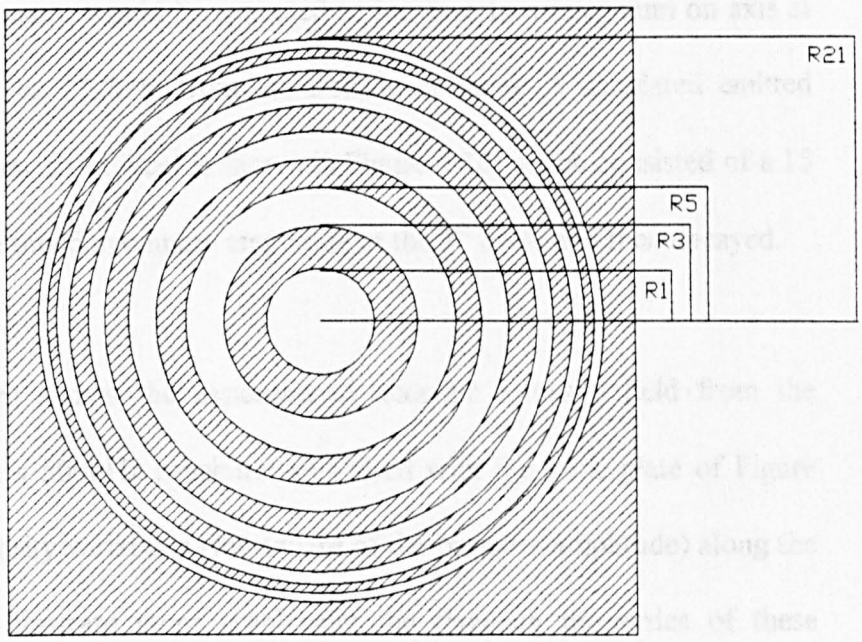

Figure 4.9. Schematic diagram of a zone plate.

zone plate was etched chemically from sheet stainless steel of 0.13mm thickness, using a computer-derived mask and photolithography. Concentric rings were held together by thin radial bridges included in the original mask (not shown). This zone plate was placed across the transducer aperture, at a distance of 5mm from the radiating membrane. Thus, when a 500kHz toneburst was applied to a transducer fitted with the zone plate, the axial pressure would be expected to increase to a maximum on axis at 7.5mm from the plate (or 12.5mm from the transducer face). A simulated emitted waveform (i.e. close to the front face) is shown in Figure 4.10, which consisted of a 15 cycle toneburst which reached maximum amplitude at the 7^{th} cycle and then decayed.

Figure 4.11 (solid line) shows the experimental acoustic intensity field from the transducer, driven with a 500kHz toneburst and fitted with the zone plate of Figure 4.9. Note that now intensity variations (the square of the pressure amplitude) along the axis were plotted, to illustrate more graphically the focusing properties of these devices; due to the high noise floor on the experimental plot, pressure field variations off-axis did not correspond well to the theoretical result, and is possibly due to the effects of signal averaging across the receiver aperture. It is evident, however that the transducer assembly has focused in air at the expected distance of 7.5mm from the zone plate. Note the sharp radial focus, and the rapid axial decay of pressure amplitude at larger axial distances. Theoretically, the response of the zone plate can be simulated using the response of annuli as above. Here, the zone plate can be considered as a set of concentric annuli surrounding a central radiating disk; hence, the response can be found by adding the separate contributions of the central disk and each annulus in turn, for each field point. When this is done, the pressure field expected theoretically for

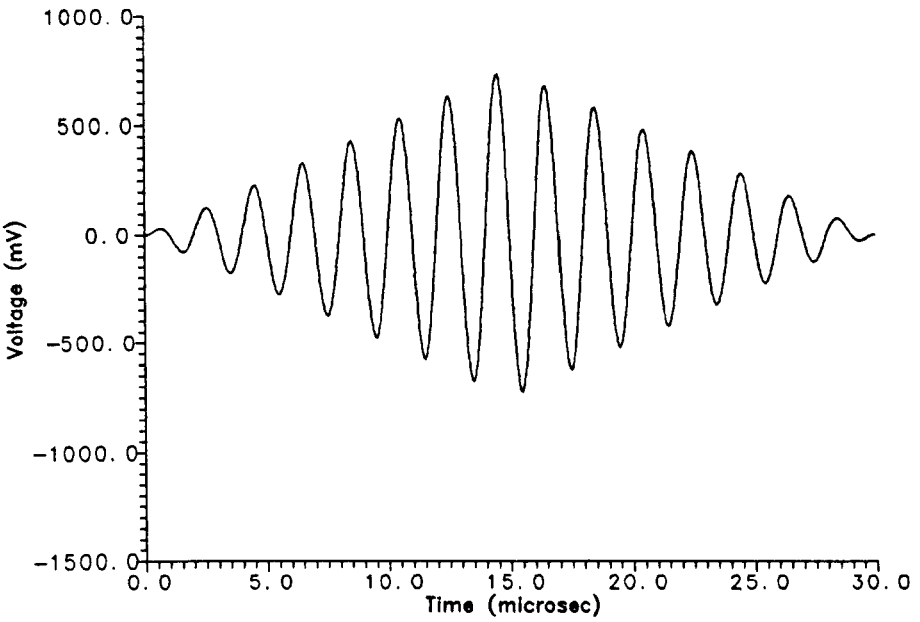

Figure 4.10. Simulated emitted waveform (i.e. close to the front face) used to predict the field of the transducer fitted with the zone plate.

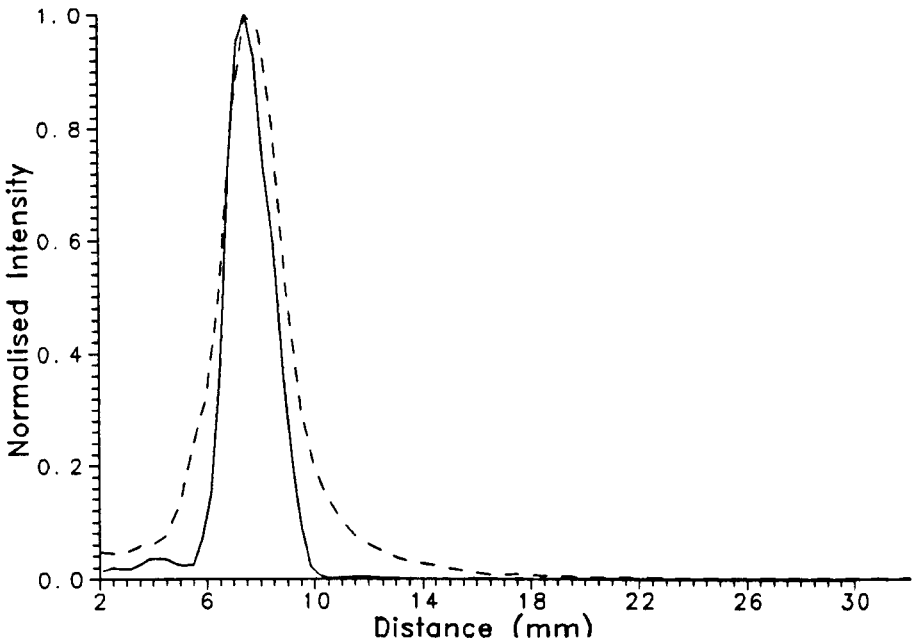

Figure 4.11. Experimental(solid line) theoretical (dashed line) 2D acoustic intensity axial plot, for a plane piston transducer fitted with the zone plate driven by a 500kHz toneburst.

500kHz toneburst generation in air is shown in Figure 4.11 (dashed line). In agreement with the predictions of equation (4.9), and the experimental observations of Figure 4.11(a), the pressure amplitude peaks at 7.5mm, and exhibits a rapid decay in amplitude at greater axial distances.

Furthermore, with the development of the theoretical model it was possible to determine the manufacturing errors and variations errors in the driving frequency. Typically, due to the manufacturing process of the mask, undercutting amounted up to 12μm departure from the ideal design specification. As zone plates are sensitive to zone displacement it was first thought that the performance could be affected by the dimensions. The ideal dimensions were reduced by 12μm at each of the boundaries, and thus each ring was reduced by 24μm. A theoretical intensity plot was generated using a drive frequency of 500kHz for the modified zone plate and this is shown in Figure 4.12(b), this was compared to a zone plate of ideal dimensions driven by 500kHz (Figure 4.12(a)). Both theoretical plots were virtually identical with the focal point appearing at the design value (7.5mm), thus suggesting that undercutting during zone plate manufacture has a negligible effect. Again, the performance of an ideal zone (i.e. design dimensions) plate was modelled using different drive frequencies of the same format as in Figure 4.10 (the velocity was fixed at 340m/s). The intensity plots for a frequency of 580kHz, as shown in Figure 4.13, and the ideal driving frequency 500kHz (Figure 4.12(a)) shows only a small difference in some of the near field and interference structure leading to the peaks. The main difference was found to be a small reduction in the focal intensity and the focal length increased to about 9mm from the nominal 7.5mm.

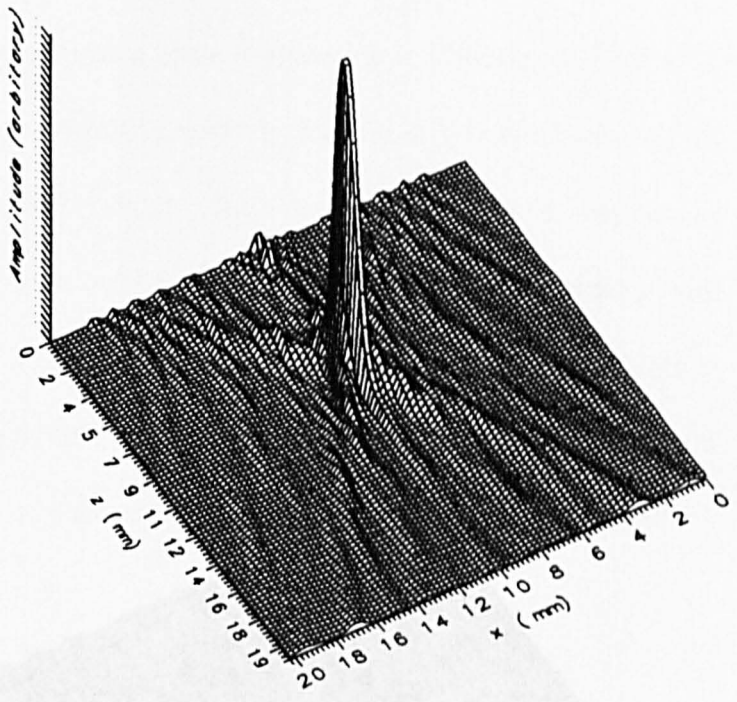

(a)

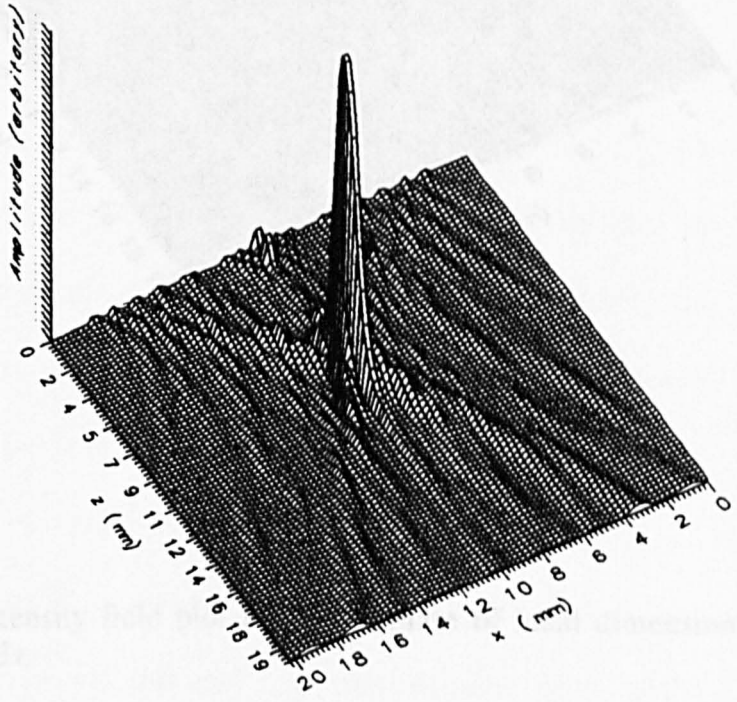

(b)

Figure 4.12. (a) Theoretical intensity plot for a zone plate of ideal dimensions driven at 500kHz, (b) theoretical intensity plot for a modified zoneplate driven at 500kHz.

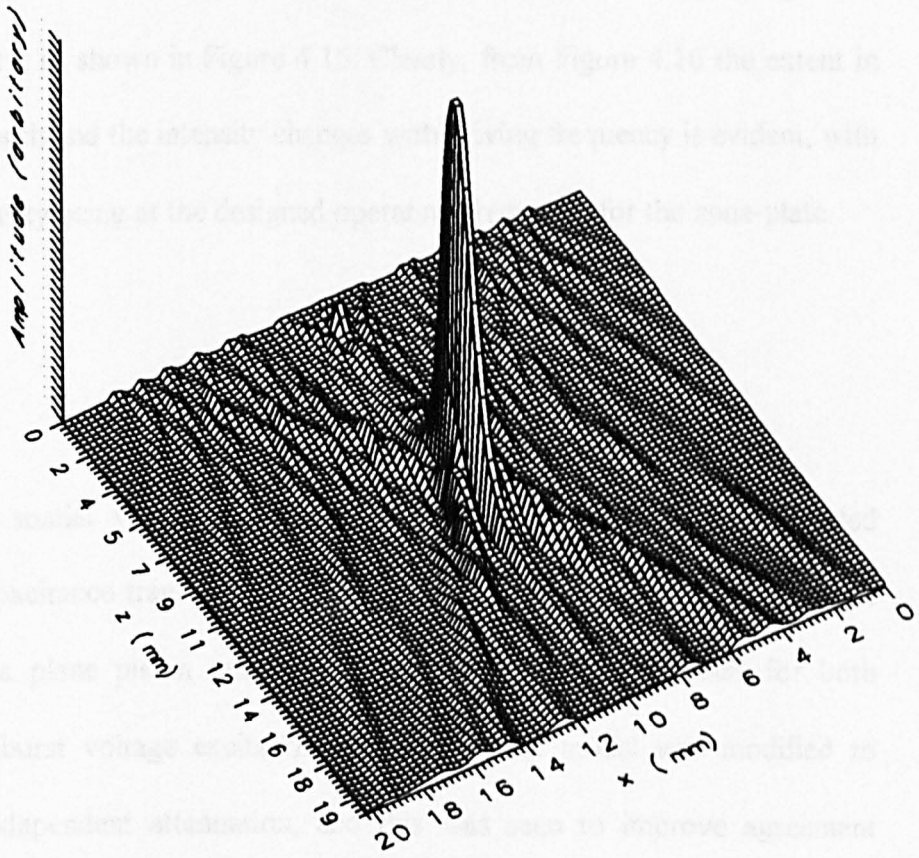

Figure 4.13. Intensity field plot for a zoneplate of ideal dimensions driven at 580kHz.

Intensity plots were also generated using drive frequencies of 300kHz, and 800kHz, and are shown in Figures 4.14 and 4.15 respectively. Clearly, the focal length changes dramatically with the range extending from 2.5mm for the 300kHz to 14mm for the 800kHz drive signals. However, the focal spot-size does not significantly change with change in frequency, as shown in Figure 4.16. Clearly, from Figure 4.16 the extent in which the focal length and the intensity changes with driving frequency is evident, with the maximum intensity being at the designed operating frequency for the zone-plate.

4.4 Conclusions

The experimental spatial variations in peak sound pressure from an air-coupled micromachined capacitance transducer have been demonstrated to show many of the characteristics of a plane piston radiator. This was seen to be the case for both transient and toneburst voltage excitation. The theoretical model was modified to include frequency-dependent attenuation, and this was seen to improve agreement between theory and experiment. With additional modifications to the plane piston model, it was possible to predict the output from both annular and zone plate transducers, and this was again compared to experiment with reasonable agreement, indicating that axial pressures could be increased by both methods. With further investigations, the theoretical model was also used to predict the performance of the zone plate for changes in dimension and driving frequency, and control over the focusing length was achieved over a frequency range of 300-800kHz which covers much of the useful frequency range of air-coupled ultrasonics.

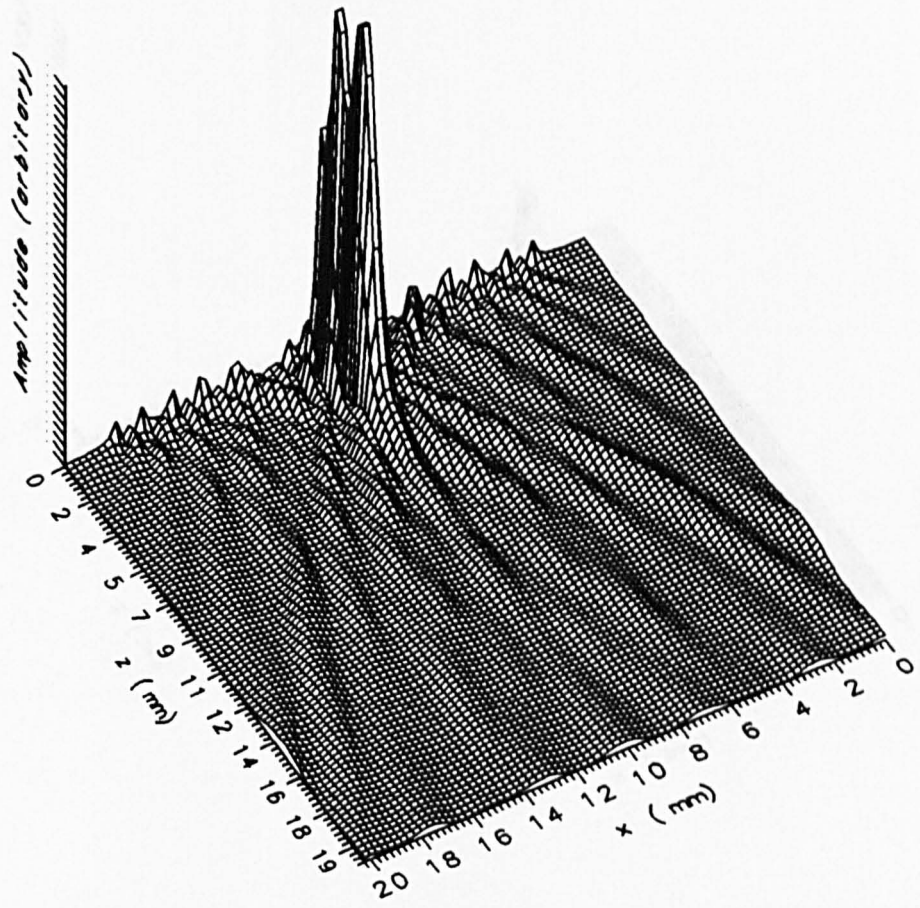

Figure 4.14. Theoretical intensity plot for a zoneplate of ideal dimensions driven at 300kHz.

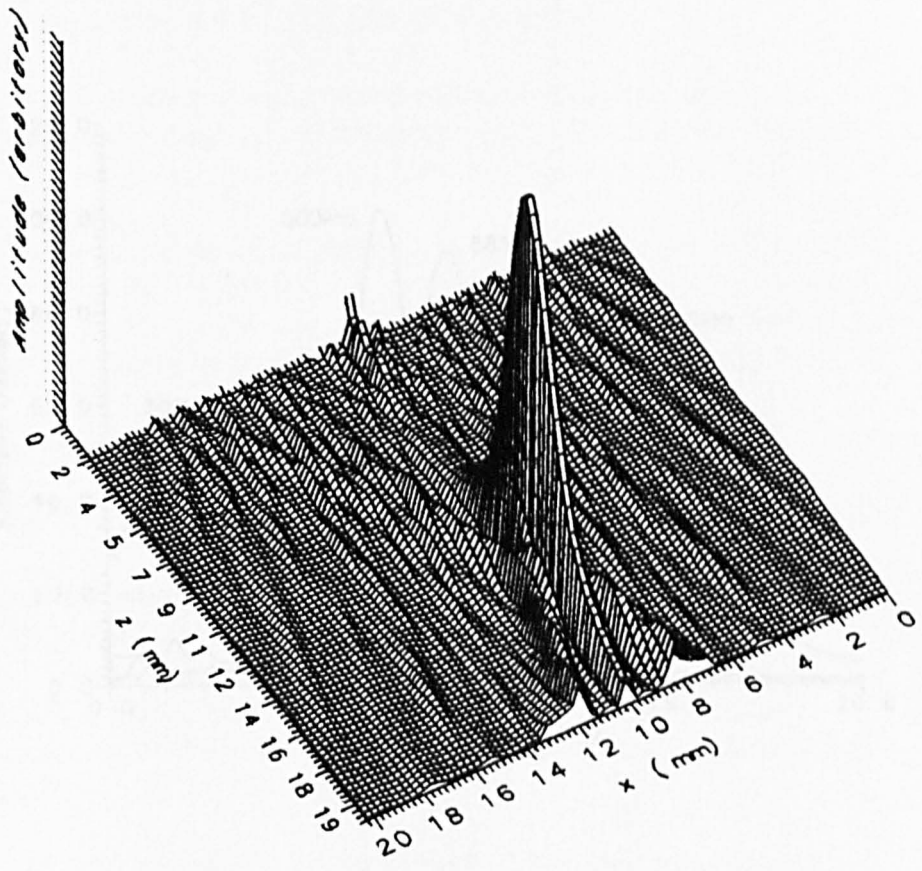

Figure 4.15. theoretical intensity plot for a zone plate of ideal dimensions driven at 800kHz.

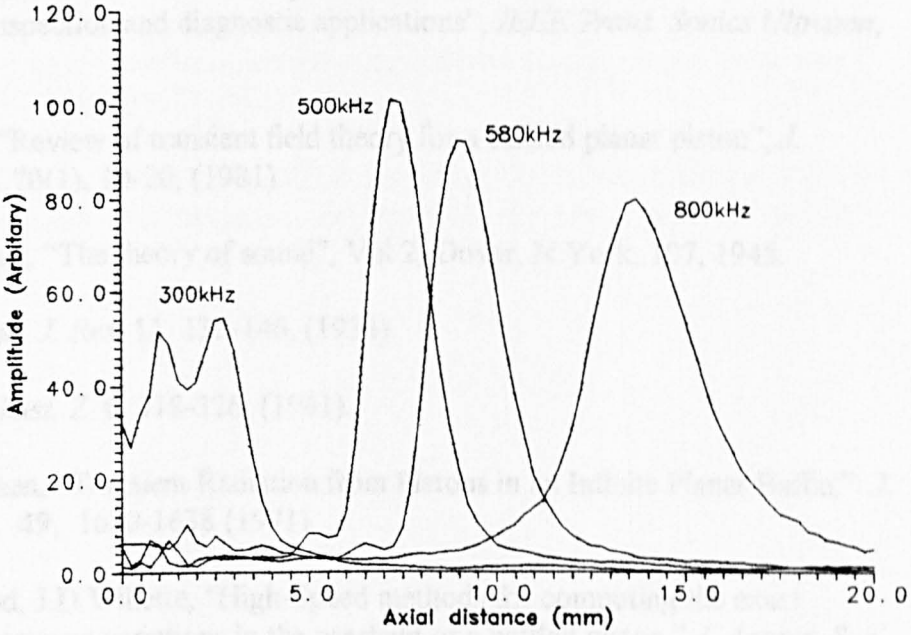

Figure 4.16. Theoretical axial 2D intensity field plot for an ideal zone plate with a drive frequencies of 300kHz, 500kHz, 580kHz, and 800kHz.

The results presented in this chapter were published as papers [18,19].

4.5 References

[1] M.Babic, "A 200-kHz Ultrasonic transducer coupled to the air with a radiating membrane," *IEEE Transactions (UFFC)*, **38 (3)**, 252-255 (1990).

[2] E.P. Papadakis, "Theoretical and experimental methods to evaluate ultrasonic transducers for inspection and diagnostic applications", *IEEE Trans. Sonics Ultrason*, **26**, 1-14, 1979.

[3] G.R. Harris, "Review of transient field theory for a baffled planar piston", *J. Acoust. Soc. Am*, **70**(1), 10-20, (1981).

[4] J.W.S Rayleigh, "The theory of sound", Vol 2, Dover, N.York, 107, 1945.

[5] L.V King, *Can, J. Res.* **11**, 135-146, (1934).

[6] A. Schoch, *Akust. Z.* **6**, 318-326, (1941).

[7] P.R.Stepanishen, "Transient Radiation from Pistons in an Infinite Planar Baffle," *J. Acoust. Soc. Am.* **49**, 1630-1638 (1971).

[8] J.C.Lockwood, J.D.Willette, "High-Speed methods for computing the exact solution for the pressure variations in the nearfield of a baffled piston," *J. Acoust. Soc. Am.* **53**, 735-741 (1973).

[9] D.A. Hutchins and G. Hayward, "The radiated field of ultrasonic transducers," in *Physical Acoustics, Vol XIX (Academic Press, NY, R.N. Thurston and A.D. Pierce, eds., 1990)*, 2-134 (1990).

[10] R. Hickling and S.P. Marin, "The use of ultrasonics for gauging and proximity sensing in air," *J. Acoust. Soc. Am.* **79**, 1151-1159 (1986).

[11] H.E. Bass, L.C. Sutherland and L. Evans, "Atmospheric absorption of sound: Theoretical predictions," *J. Acoust. Soc. Am.* **51**, 1565-1572 (1972).

[12] L.J.Bond, C.Chiang, C.M.Fortunko "Absorption of ultrasonic waves in air at high frequencies (10-20MHz)," *J. Acoust. Soc. Am.* **92**, 2006-2015 (1992).

[13] H.E. Bass, L.C. Sutherland, A.J. Zuckerwar, "Atmospheric absorption of sound:Update," *J. Acoust. Soc. Am.* **88**, 2019-2020 (1990).

[14] D.W. Schindel, D.A. Hutchins "The capacitance transducer as a standard ultrasonic source in solids," *J. Acoustic. Soc. Am.* **97**, 1650-1659 (1995).

[15] D.W. Schindel, D.A. Hutchins, L. Zou and M. Sayer, "The design and characterisation of micromachined air-coupled capacitance transducers," *IEEE Trans. Ultras. Ferr. Freq. Contr.* **42**, 42-50 (1995).

[16] E. Hecht, A.Zajac, "Optics", Addison-Wesley, London, ch.10 (1979).

[17] M.Z.Sleva, W.D.Hunt, R.D. Briggs, "Focusing performance of epoxy and air-backed polyvinylidene fluoride Fresnel zone plates," *J. Acoust. Soc. Am.* **96**, 1627-1633 (1994).

[18] A.G. Bashford, D.W. Schindel, D.A. Hutchins, and W.M.D. Wright, "Field characteriastion of an air-coupled micromachined ultrasonic capacitance transducer", *J. Acoust. Soc. Am.* **100**(6), 1-8 (1996).

[19] D.W. Schindel, A.G. Bashford and D.A. Hutchins, " Field characterisatics of air-coupled micromachined capacitance transducers fitted with a zone plate", *J. Acoust Soc. Am.* (in press).

CHAPTER 5

MICROMACHINED ULTRASONIC CAPACITANCE TRANSDUCERS FOR IMMERSION APPLICATIONS

5.1 Introduction

Water-coupled ultrasonic transducers are widely employed for immersion applications, such as non-destructive evaluation of materials, medical imaging, and others. The majority of the transducers used in such applications are based upon a piezoelectric active element, the most common of which is PZT (lead zirconate titanate). PZT has become popular mainly because of its high conversion efficiency between electrical and mechanical energy, and also because it is widely available, but it also has the drawbacks of having an inherently resonant response and a strong coupling between radial and thickness modes of vibration. These drawbacks, in fact, have been the driving force for investigations into other types of piezoelectric materials that are suitable for immersion testing, such as PMN (lead metaniobate), and PVDF (polyvinyldene difloride). PMN, for example, has been found to have a lower cross-coupling to radial modes, whereas PVDF, being a thin polymer material, can be made with a wider bandwidth and with an acoustic impedance that is closer to that of water. In spite of such advances, however, PZT is still the preferred material for many immersion applications, where its resonant nature is often controlled through the use of backing/damping layers, while its impedance mismatch with water is commonly reduced by the use of front-face matching layer(s).

Another significant and ongoing problem with immersion transducers (piezoelectric or otherwise), is the difficulty in making the devices perform both predictably and repeatably; studies, in fact, have shown, that there is a great variability in the performance of such transducers. Provided that the transducer characteristics approach those of a plane piston transducer, then standardised measurements with miniature hydrophones can be used to predict performance, and comparison to theoretical approaches can be made [1,2]. However, it is problems with repeatability that can hinder such studies, as often the front surface of the transducer does not radiate with a uniform amplitude and phase, and hence a plane piston cannot be assumed. For these reasons, much work has been performed to try to make piezoelectric transducers more predictable and with wider bandwidths. For instance, modified piezoelectric materials such as porous PZT and PZT-polymer composites [3-5] have shown some promise; they exhibit wider bandwidths and better matching to water (as compared with PZT alone), and most-importantly have shown some improvements in terms of predictability. But despite the improvments, current immersion transducers are still less than ideal, and transducers with greater predictability continue to be sought. If found, such transducers would lead to marked improvements in calibration techniques and standards, as well as in quantitative measurements for immersion applications.

One type of immersion transducer that shows promise in terms of repeatability and predictability is the capacitance or electrostatic transducer, particularly when manufactured using micromachining techniques, Capacitance devices employing thin polymer membranes have been investigated extensively for use in air, to which they are inherently well-coupled (see Chapter 4). But with the exception of some early work [6-

8], and some preliminary studies by the authors and others [9-12], very little research has been done on the use of these capacitance transducers in liquids. And yet they appear to have a number of valuable properties. For example, the preliminary studies have shown that capacitive immersion transducers are: (a) inherently wideband, with frequency responses extending from 200kHz to over 15MHz [6,8]; (b) surpringly well-coupled to water; (c) operate on electrostatic forces, which are generally far-easier to model than piezoelectric forces [16,21]; and (d) when manufactured using micromachining techniques, may allow predictable and reproducible generation of any beam-profile that might be required in a liquid [6]. Such characteristics, if they can be fully developed, would no doubt be of value in immersion ultrasonics, particularly where calibration, standards, and quantitative measurements are concerned. A further investigation of capacitive immersion transducers is therefore justified.

Of particular interest are the changes in performance that occur when these devices are subject to water loading. As will be seen, there are at least three reasons to expect a difference in response. First, the acoustic impedance of water is very much higher than for air, yet is closer to the bulk membrane material (usually a polymer). Second, the increased pressure exerted on the membrane through water loading can change both bandwidths and sensitivities. And finally, the attenuation in air above 2MHz starts getting to be a serious limitation in air-coupled work [13-15], whereas this is not the case in water.

In the work to follow, it was important to theoretically model the responses of the micromachined capacitance transducers, as well as to experimentally characterise their

performance in water. The theoretical approach to determine the pressure field variations is the same as described for the air-coupled case in chapter 4.

A variety of experimental methods have also been established with which to characterize immersion transducers, and an overview is provided by Sachse & Hsu [1]. Typically, the most common method is to scan a miniature hydrophone within the radiated field, where a range of hydrophones may be used. Piezoceramic elements, for example, have often been used for hydrophone transduction in the past, although recent designs that introduce pores into the piezoceramic to reduce the impedance mismatch [16] have lead to hydrophones with improved sensitivity. Other hydrophones have substituted piezoceramic composites instead, such as a low-dielectric polymer phase within a 3-D network of porous PZT ceramic. This method gives an increase in the piezoelectric constant of about 4-5 times as compared to pure PZT [17]. More recently, PVDF polymer film has become a common element for use in hydrophones [18,19] which, when compared to piezoceramic, tends to have an increased frequency response range, lower mechanical Q, and a higher piezoelectric constant. These PVDF films are often used either to produce a membrane [18], or a miniature probe [20-22], although for large angles of incidence the membrane approach is usually avoided due to spurious Lamb wave generation. Note that a number of systematic errors can occur when using any hydrophone for absolute pressure-field measurements, including spatial averaging, which arises when the received ultrasonic wavelength is of comparable size (or smaller) than the finite radius of the hydrophone, and waveform distortion, which arises from effects of finite amplitude propagation in the water path (for wide-

bandwidth hydrophones). Typically, correctionscan sometimes be made, these account for the waveform distortions on spatial averaging [23].

5.2 Apperatus and experiment

The pressure waveforms throughout the fields of the micromachined capacitance transducers were measured in water using a 1mm diameter miniature hydrophone (0.1 - 10 MHz flat response, not the same as used in chapter 3). The source transducers under test were specially constructed using polished aluminum backplates, each of 12.5mm diameter. These backplates were laser micromachined to create a square array of 50μm diameter cylindrical pits with a 150μm pitch, where each pit had a depth of 50μm. The backplates were fitted with either a 5μm thick, metallized Mylar polymer membrane, or a 20μm thick solid Mica membrane, whose upper surface was metallized with gold. Mica was considered as a membrane material because of its high dielectric constant and stiffness, and it does not leak water, the former property allowing it to withstand high driving voltages without dielectric breakdown, whereas the latter property provides a higher frequency response for the thickness.

Figure 5.1 shows the construction of a typical water-coupled capacitance transducer source (essentially the same as the air-coupled transducer in chapter 3 but with O-ring seals). The thin membrane was stretched across the circumference of the grounded aluminium casing, and an O-ring of 10mm outer diameter and 9mm inner diameter was placed centrally on top of the membrane. A 7mm diameter aperture was placed over the O-ring and secured to the grounded case using conducting screws. When the

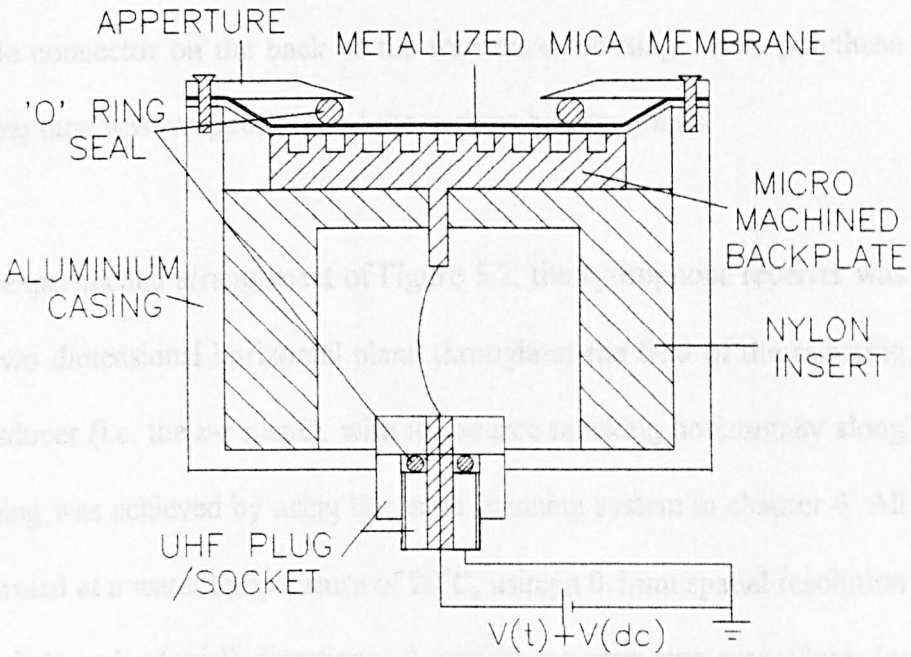

Figure 5.1. Schematic diagram of a water-coupled capacitance transducer employing a laser micromachined backplate.

backplate was moved towards the aperture, the O-ring was compressed between the membrane and aperture, creating a watertight seal and reducing the fluid contact area. As Mylar membranes of this thickness will allow moisture to diffuse through to the backplate after a few hours, the membrane was made waterproof by spraying the active area with a thin layer of PTFE (Teflon). Note that a second O-ring was used at the UHF power cable connector on the back of the transducer housing, while polythene electrical insulating tape was wrapped around the various housing joints.

As shown in the experimental arrangement of Figure 5.2, the hydrophone receiver was scanned over a two dimensional horizontal plane throughout the field of the radiating capacitance transducer (i.e. the x-z plane), with the source radiating horizontally along the z axis. Scanning was achieved by using the same scanning system in chapter 4. All scans were performed at a water temperature of 20°C, using a 0.5mm spatial resolution in both the x (radial) and z (axial) directions. A typical x-z scan area was 15mm by 20mm, with the field starting at z=2mm from the front face of the transducer membrane.

Driving voltages applied to the capacitance sources were of two different types. The first was a toneburst voltage, which was created using an power amplifier (55dB gain, 0.3- 35MHz) and a arbitrary waveform generator. This toneburst consisted of approximately 5 cycles of a sinusoidal signal at 2.25MHz (same wavelength in air at 500kHz, thus the same scan parameters from chapter 3 can be used) and with a 350V amplitude (peak-to-peak). The second type of driving voltage was in the form of a pulse. This was created by a pulser and provided an impulsive transient of 350V with

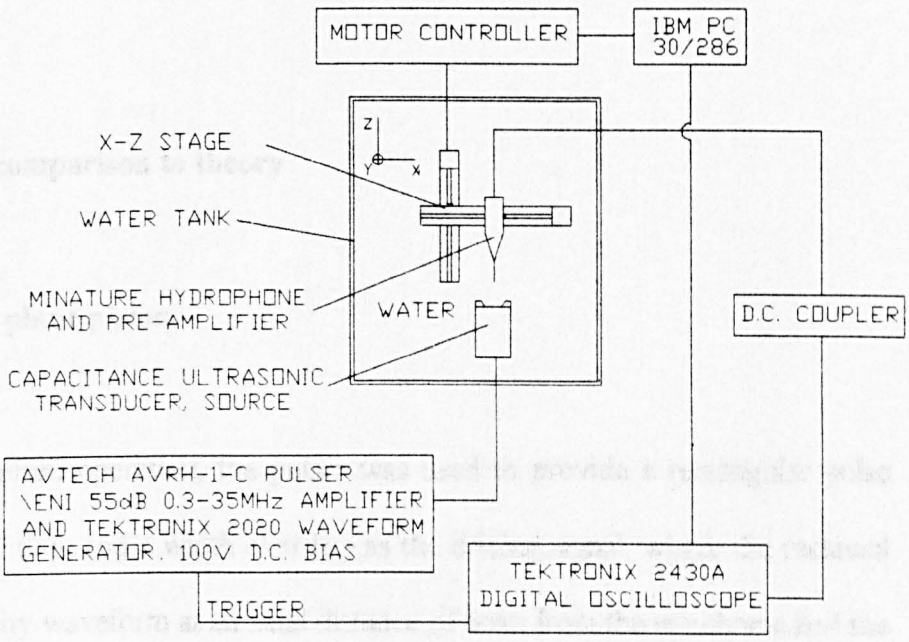

Figure 5.2. Schematic diagram of the hydrophone scanning system used.

a width adjustable from 0.1-10μs. Superimposed upon both types of transient voltage was a 100V bias. Note that all scanning was performed with source driving frequencies restricted to an upper limit of 2.25MHz, for at this frequency the wavelength in water is approximately 0.66mm (i.e. less then two wavelengths over the hydrophone diameter).

5.3 Results and comparison to theory

5.3.1 Fields of a plane piston

In the case of pulsed operation, the pulser was used to provide a rectangular pulse with a 0.15μs rise time and a width of 0.1μs as the driving signal, where the recieved hydrophone velocity waveform at an axial distance of 6mm from the membrane had the form shown in Figure 5.3(a) (solid line) for water coupling, and (dashed line) for air-coupling. Note that both signals were received by a damped wide-bandwidth 1mm diameter PVDF hydrophone.

By looking at the normalized FFTs of the above measured signals (Figure 5.3(b)), it is evident that a bandwidth of approximately 2MHz has resulted in air, whereas in water the bandwidth was in excess of 8MHz. This is thought to be due to the three effects mentioned earlier, namely a different impedance load on the front membrane; compression of the air-pockets behind the thin-polymer membrane in the case of water-loading; and the more extensive attenuation in air at higher frequencies.

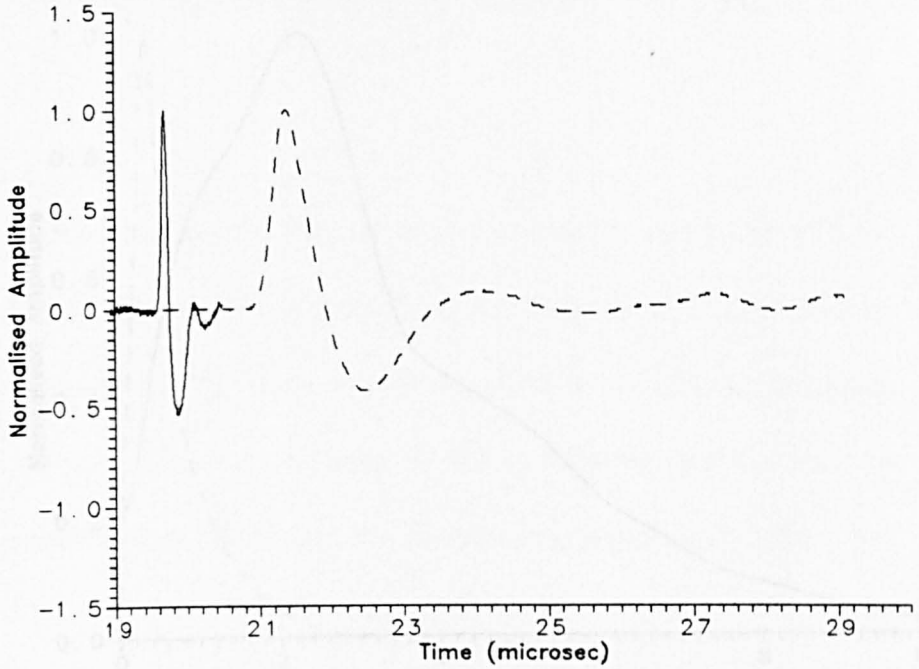

Figure 5.3. (a). Detected normalised velocity waveform in water (solid line) and in air (dashed line) at z=6mm using a 5μm thick Mylar membrane.

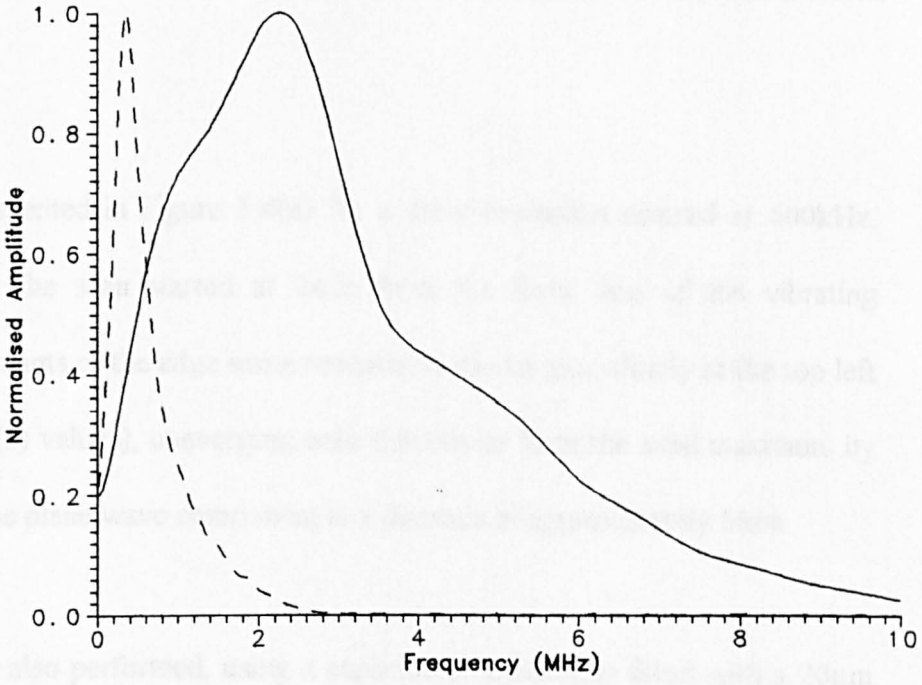

Figure 5.3. (b) Spectrum of the received velocity waveform: water (solid) and air (dashed).

Two scans were performed, first using a Mylar membrane (5μm) and the second using a Mica membrane (20μm). Spatial variations of the peak sound-pressure were now measured experimentally for the 7mm diameter Mylar membrane capacitance transducer source, using a 350V drive pulse. The driving pulse width was varied to give a plane wave pressure component close to the transducer, with a predetermined center frequency.

The results are presented in Figure 5.4(a) for a drive excitation centred at 600kHz. Remembering that the scan started at 2mm from the front face of the vibrating membrane, the remnants of the edge wave component can be seen clearly at the top left (i.e. at small axial (z) values), converging onto the axis to form the axial maximum by interference with the plane wave component at a distance of approximately 5mm.

A second scan was also performed, using a capacitance transducer fitted with a 20μm thick mica membrane (allows the aperture to be secured water tight without damaging the membrane). These results are included in Figure 5.4(b), where the same driving signal was again employed (i.e., as for the Mylar-membrane transducer of Figure 5.4(a)). A comparison of Figures 5.4(a) and 5.4(b) shows that the mica membrane device operated in a similar fashion, with the nearfield/farfield boundary positioned at an approximate axial distance of 5mm.

The corresponding theoretical pressure variations in water for a plane piston radiator of 7mm diameter were now calculated using equations (1)-(8) in chapter 4. The result is shown in Figure 5.4(c) and may be directly compared with the two previous

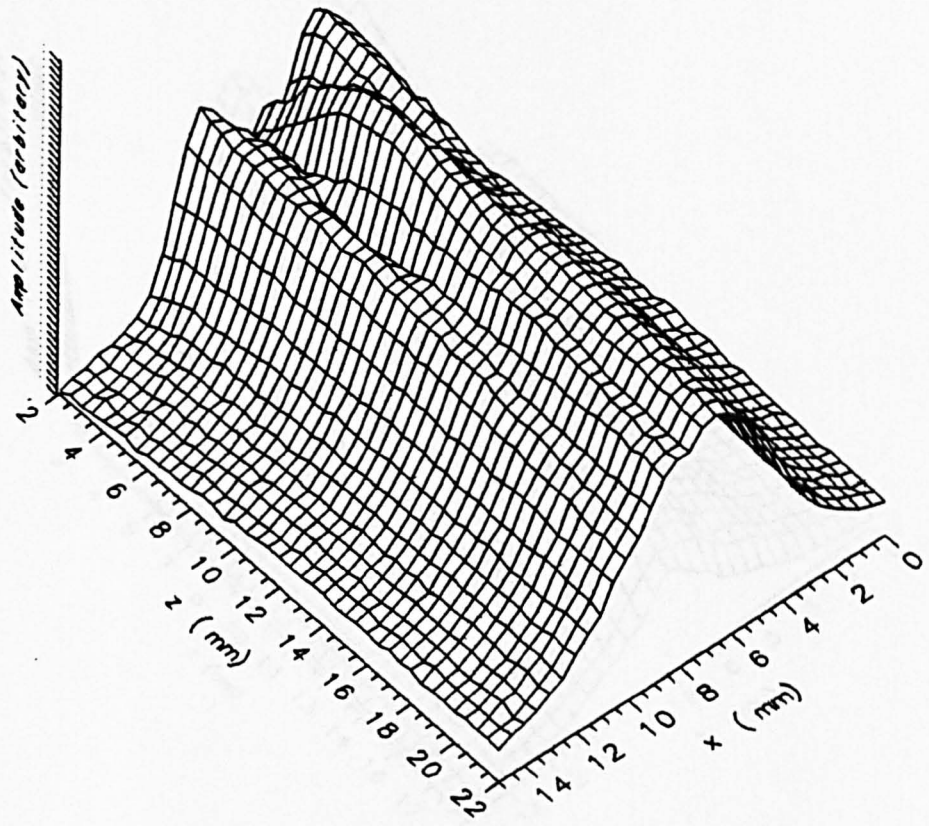

Figure 5.4 (a) Experimental peak sound pressure variations using a 5μm thick Mylar membrane.

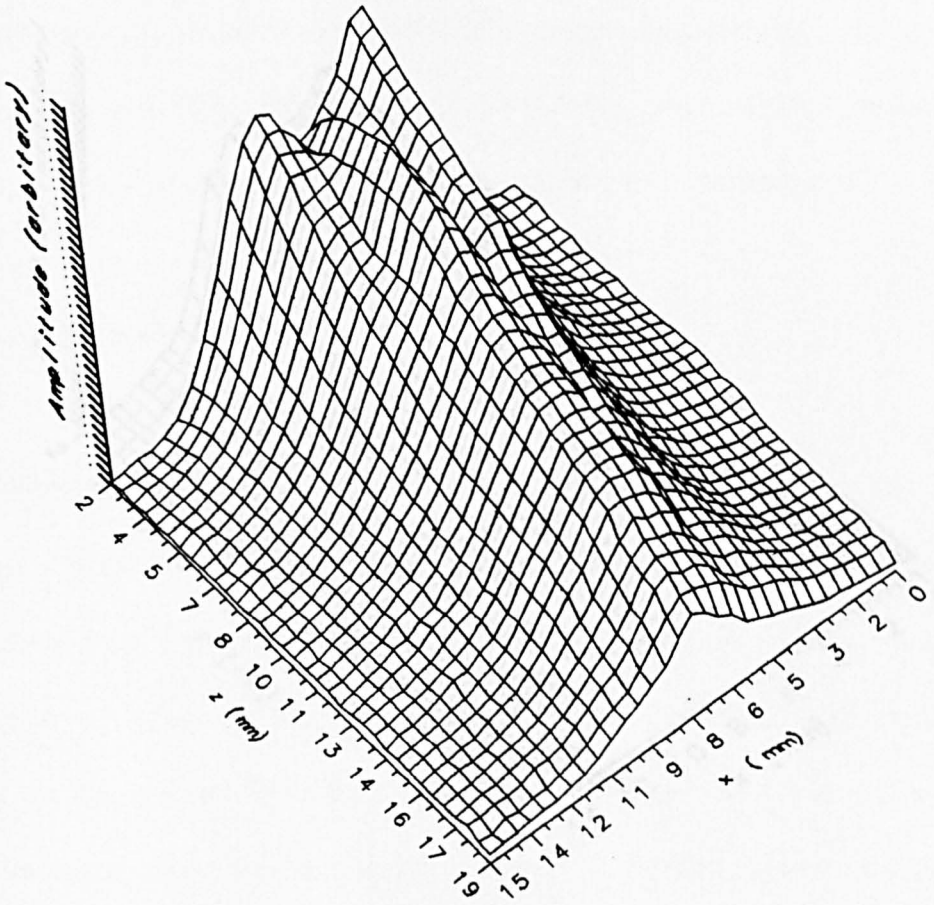

Figure 5.4. (b) Experimental peak sound pressure variations using a 20μm thick Mica membrane.

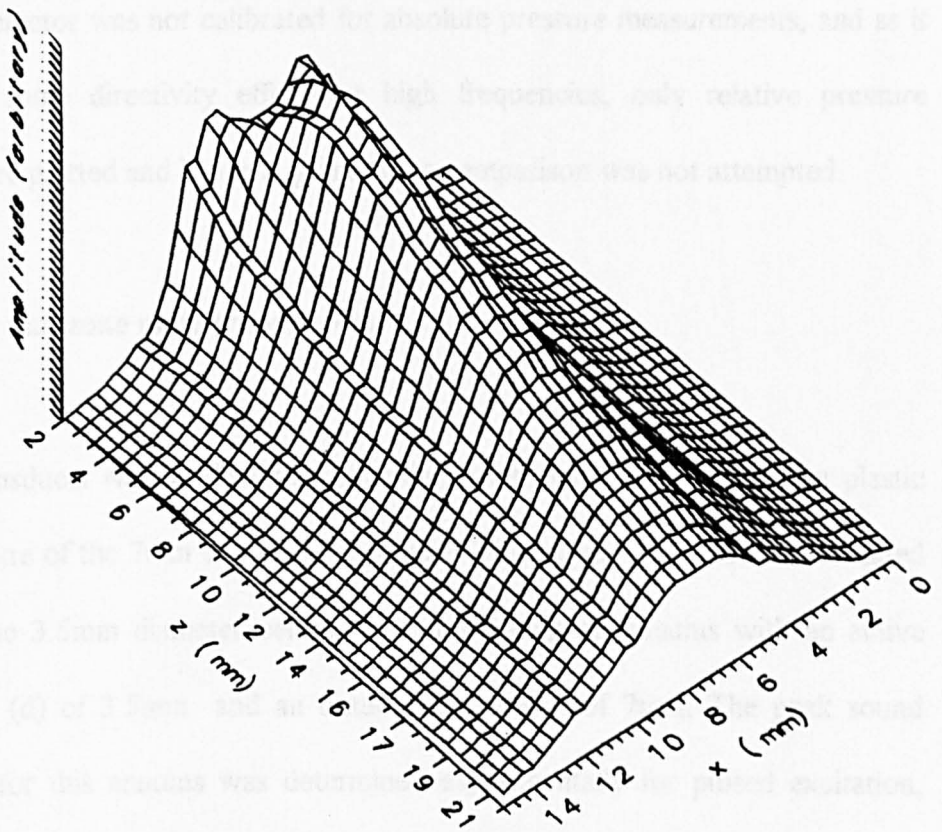

Figure 5.4 (c) Theoretical peak sound pressure variations, for a plane piston driven by a pulse centred at 600kHz.

experimental scans. Good qualitative agreement is evident throughout, with the nearfield/farfield boundary positioned at the same axial distance of approximately 5mm, as expected from the quoted centre frequency. However, as the miniature hydrophone detector was not calibrated for absolute pressure measurements, and as it probably has some directivity effects at high frequencies, only relative pressure amplitudes were plotted and hence a quantitative comparison was not attempted.

5.3.2 Annular and zone plate transducers

An annular transducer was produced by attaching a concentric 3.5mm diameter plastic disk to the centre of the 7mm diameter membrane. This plastic disk absorbed radiated output over the 3.5mm diameter central area, producing an annulus with an active inner diameter (d) of 3.5mm and an outer diameter (D) of 7mm. The peak sound pressure field for this annulus was determined experimentally for pulsed excitation, again using the Avtec pulser with a centre frequency of 600kHz. The results are shown in Figure 5.5(a). Note the tendency for axial focusing, with a gradual increase in axial amplitude towards the maximum, accompanied by a smooth decrease in the direct radiation from the active area of the annulus. Similar features are seen in the corresponding theoretical plot of Figure 5.5(b). This was produced by predicting the waveforms produced at each field point by two separate plane pistons, one of 7mm diameter and the other of 3.5mm diameter. At each spatial point, the waveforms were then subtracted to predict the waveform of the annulus. Note that in the theoretical plot, the features are more sharp and less attenuated than those observed experimentally. This is again thought to be due, in part, to the finite receiver aperture.

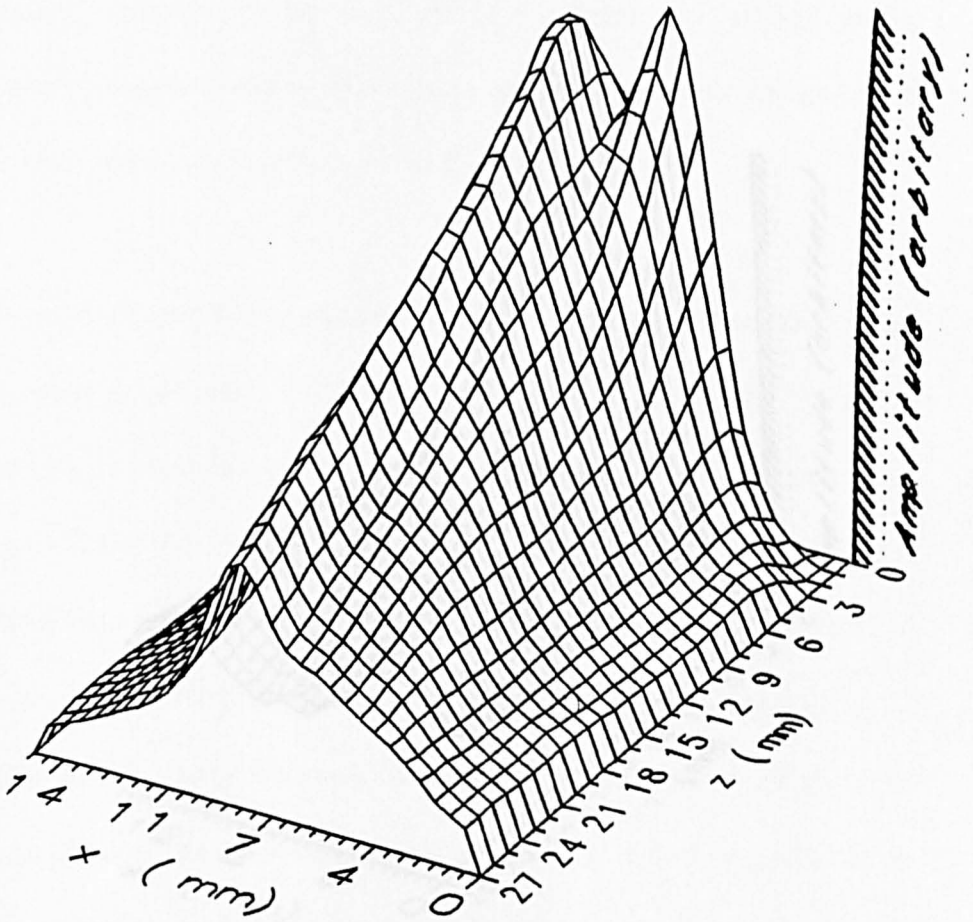

Figure 5.5 (a). Experimental peak sound pressure variations for an Annulus, driven by a pulse centred at 600kHz.

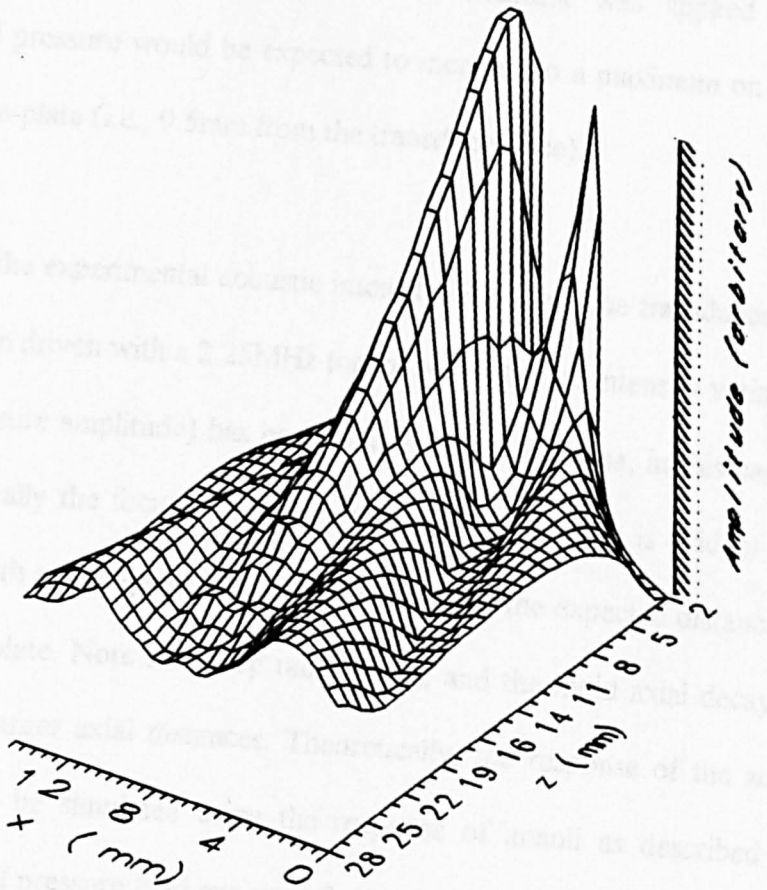

Figure 5.5. (b) Theoretical pressure variation for an annulus, driven by a pulse centred at 600kHz.

Again, the transducer was fitted with the same zone plate as in chapter 4. This zone plate was placed in front of the transducer aperture at a distance of 2mm from the radiating membrane, such that when a 2.25MHz toneburst was applied to the transducer, the axial pressure would be expected to increase to a maximum on axis at 7.5mm from the zone-plate (i.e., 9.5mm from the transducer face).

Figure 5.6(a) shows the experimental acoustic intensity field from the transducer with fitted zone-plate, when driven with a 2.25MHz toneburst. Note that intensity variations (or the square of pressure amplitude) has been plotted on the abscissa, in this case to illustrate more graphically the focusing properties of these devices. It is evident that the transducer fitted with a zone-plate has focused in water at the expected distance of 7.5mm from the zone plate. Note the sharp radial focus, and the rapid axial decay of pressure amplitude at larger axial distances. Theoretically, the response of the zone plate in water can also be simulated using the response of annuli as described in chapter 4. The theoretical pressure field expected for 2.25MHz toneburst generation in water resulted, and this is shown in Figure 5.6(b). In agreement with the predictions of equation (9) in chapter 4, and the experimental observations of Figure 5.6(a), the pressure amplitude peaks at 7.5mm, and exhibits a rapid decay in amplitude as z increases. The differences that do exist between the experimental and theoretical results are attributed primarily to the fact that transducer's radiating area in this case was smaller the largest zone of the zone-plate, such that uniform plane-wave illumination was not provided as perfectly as it should have been. Improvements can therefore be expected for such focussing transducers in the future.

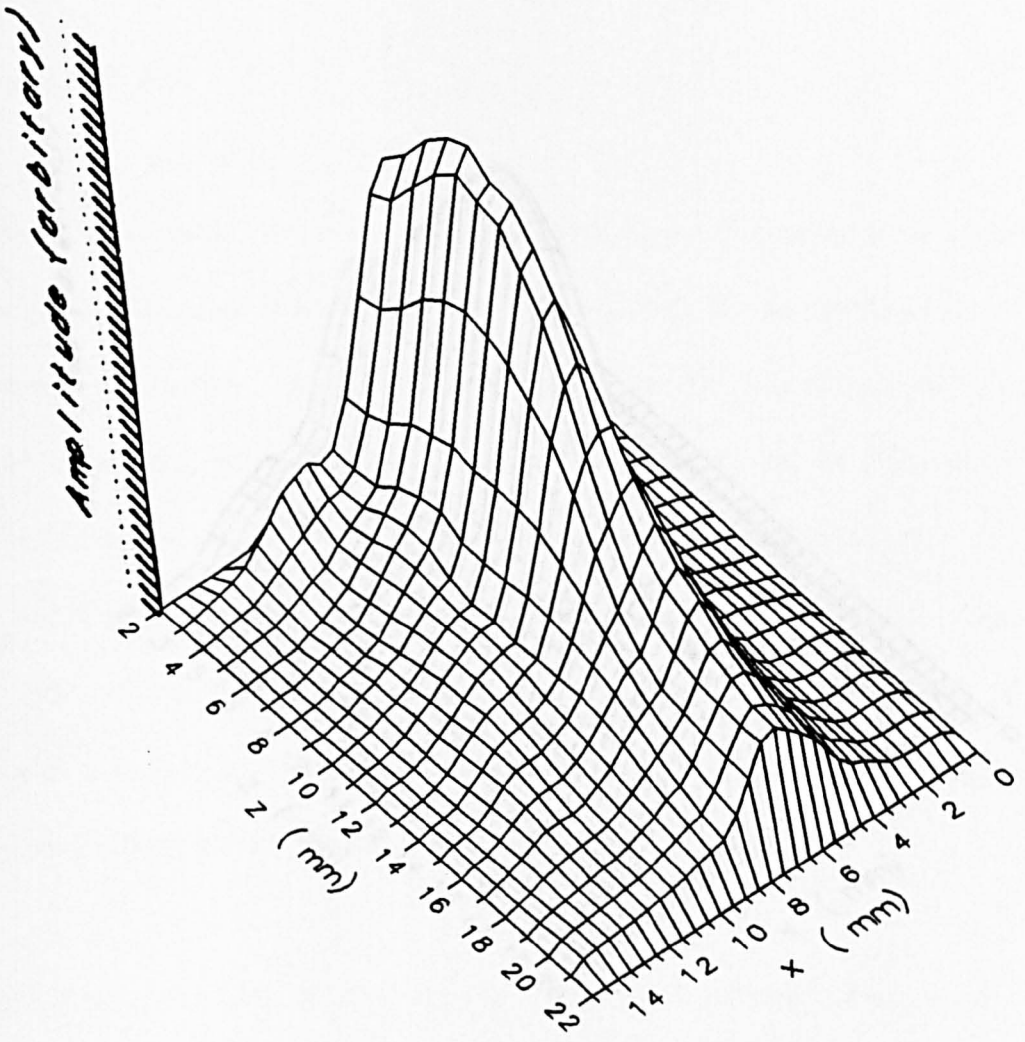

Figure 5.6 (a) Experimental peak sound pressure variations using a 5μm thick membrane plane piston transducer fitted with a zone plate.

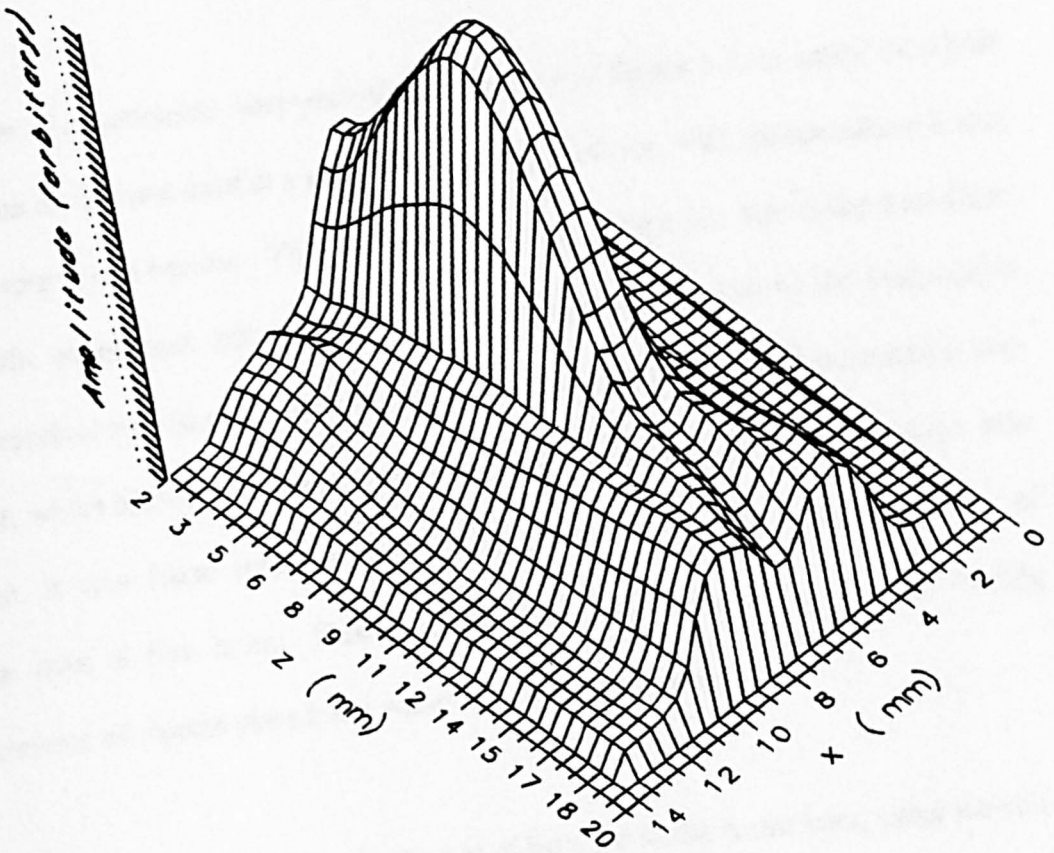

Figure 5.6. (b) Theoretical peak sound pressure variations for a plane piston transducer fitted with a zone plate.

5.4 Pulse echo c-scan

A final set of experiments were performed, as shown in Figure 5.7, in which the Mylar membrane device was used in a pulse-echo arrangement, i.e. with the transducer acting as both source and receiver. This was achieved by applying a d.c. bias to the transducer before the experiment, but then removing this before connection to the Panametrics pulser/receiver unit in pulse-echo mode. It was found that a residual polarisation was present, which allowed the device to operate without the need for an external d.c. bias voltage. It was found that this polarisation decreased gradually due to leakage of charge over a few hours. However, this was long enough for C-scan imaging experiments of objects placed in a water tank to be performed.

Figure 5.8 shows a waveform obtained in pulse-echo in the water tank, using the side-wall of the tank as a reflector. The front and back wall echoes are visible, with the phase inversion expected for a water/Plexiglas and a Plexiglas/air interface respectively. The transducer was now scanned horizontally over a Plexiglas plate containing a flat-bottomed square hole of 20mm size, and a series of waveforms recorded at 0.5mm intervals in a two-dimensional scan to form a conventional immersion C-scan image as shown in Figure 5.9. The square defect is immediately visible in the image, illustrating the fact that the capacitance device was capable of operation in a pulse-echo scanning system.

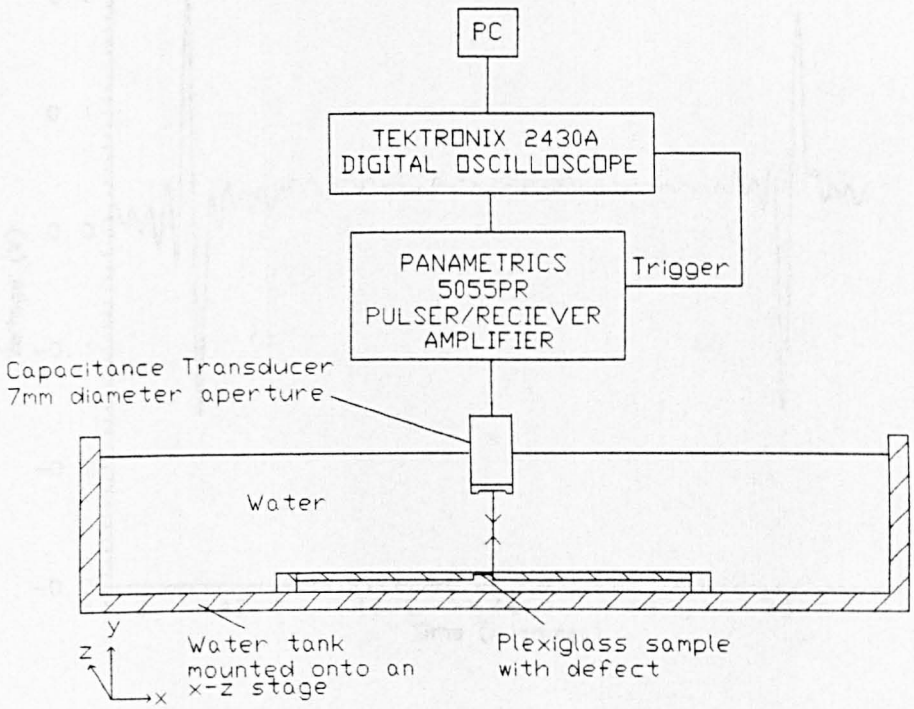

Figure 5.7. Schematic diagram of the scanning system used.

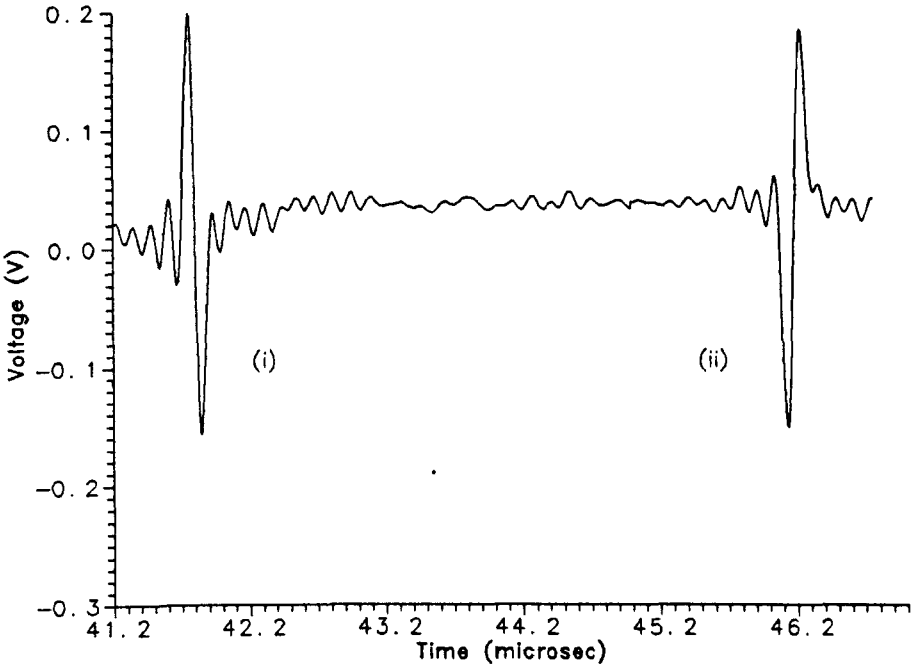

Figure 5.8. Waveform received from the pulse-echo scan, (i) front wall and (ii) back wall reflection.

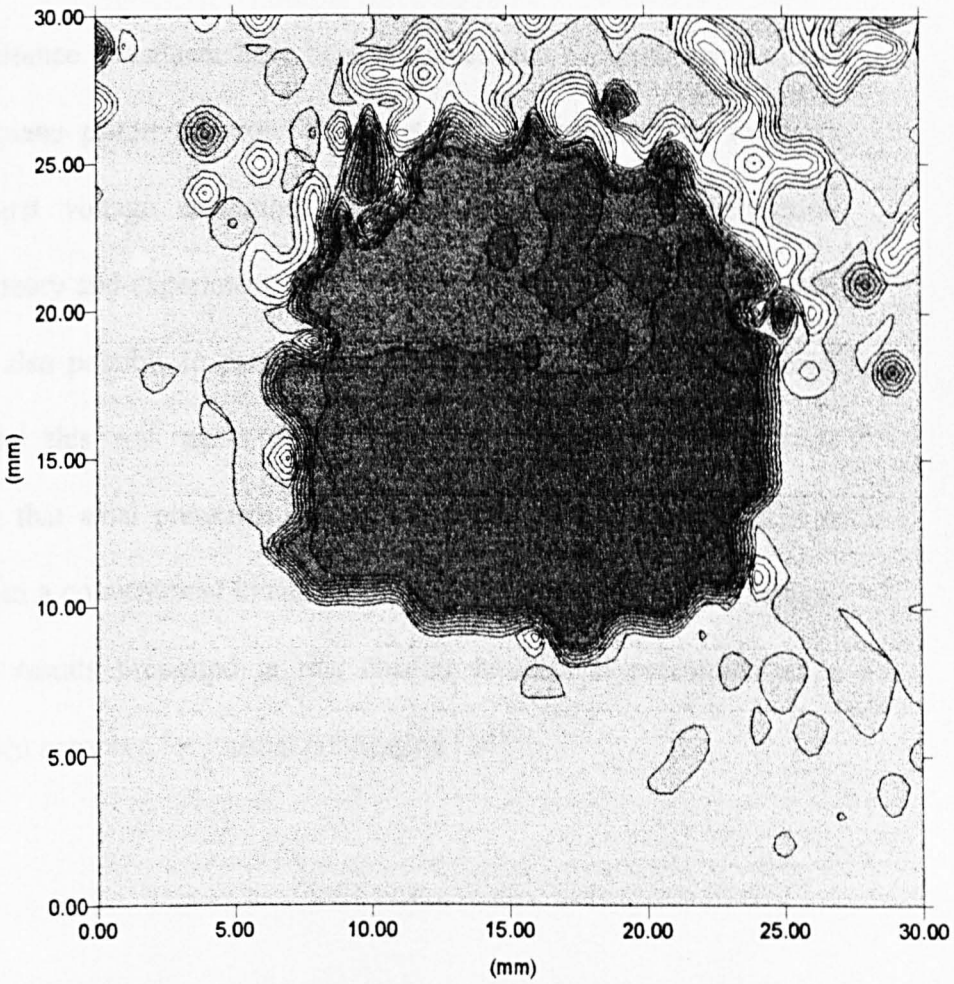

Figure 5.9. Pulse - Echo C scan image of a 20mm square defect in a perspex sample

5.5 Conclusions

The experimental spatial variations in peak sound pressure of a water-coupled micromachined capacitance transducer have been demonstrated to show many of the characteristics of a plane piston radiator. This was seen to be the case for both transient and toneburst voltage excitation. The theoretical model showed good agreement between theory and experiment. With additional modifications to the plane piston model, it was also possible to predict the output from both annular and zone plate transducers, and this was again compared to experiment with reasonable agreement, indicating that axial pressures could be increased by both methods. A device was also used in a conventional immersion system to produce a C-scan image. Please note that the results presented in this chapter have been prersented at a conference and has been accepted for journal publication [24].

5.6 References

[1] W. Sachse and N.N. Hsu, "Ultrasonic transducers for materials testing and characterisation," *Physical Acoustics, Vol XIV (Academic Press, NY, W.P Mason, R.N. Thurston, eds., 1979).*

[2] G.R. Harris, "Transient fields of a baffled planar piston having an arbitrary vibration amplitude distribution", *J. Acoust. Soc. Am.*, **70**, 186-204, (1981).

[3] T. Arai, K. Ayusawa, H. Sato, T. Miyata, K. Kawamura, K. Kobayashi, "Properties of hydrophone with porous piezoelectric ceramics", *Japanese Journal of Applied Physics*, **30**, **9B**, 2253-2255, (1991).

[4] A.M. Varaprasad, R. Krishnan " PZT-Polymer composites for transducers of hydrophone systems", *Sensors and Actuators*, **14**, pp 361-368 (1988).

[5] K. Ogura, M. Ogawa, K. Ohya, H. Banno "Receiving characteristics of d_{31}-zero piezo-rubber hydrophone", *Japanese Journal of Applied Physics*, **32**, pt 1, 5B, 2304-2306, (1993).

[6] P. Alais and M-.T. Larmande, "Etude d'un transducteur ultrasonore electostatique," C.R.Acad.Sc.Paris, t.272, Serie B, 185-188 (1971).

[7] J.A. Clarke, "A matched impedance electrostatic approach to hydrophone design", *Journal of Sound and Vibration*, 77(1), 51-59, (1981).

[8] J.H. Cantrell, Jr., J.S. Heyman, W.T. Yost, M.A. Torbett and M.A. Breazeale, "Broadband electrostatic acoustic transducer for ultrasonic measurements in liquids," *Rev.Sci.Instrum.*, **50**(1), 31-33 (1979).

[9] D.W. Schindel, D.A. Hutchins, "Capacitance devices for the controlled generation of ultrasonic fields in liquids" *Proc. 1991 IEEE Ultrasonics Symposium* **1**, 301-304 (1991).

[10] D.W. Schindel, D.A. Hutchins, L. Zou and M. Sayer, "Capacitance Transducers for Generating Ultrasonic Fields in Liquids and Gases," Proc.IEE.Conf.on 'Acoustic Sensing and Imaging', pp.7-12, conf.publ.#369, London, UK, 29-30 March, 1993.

[11] D.W. Schindel and D.A. Hutchins, "Air-coupled ultrasonic transducer" *US Patent #5,287,331*, February 1994.

[12] Khuri-Yakub, *Proc. 1995 IEEE Ultrasonics Symposium*

[13] H.E. Bass, L.C. Sutherland and L. Evans, "Atmospheric absorption of sound: Theoretical predictions," *J. Acoust. Soc. Am.* **51**, 1565-1572 (1972).

[14] L.J.Bond, C.Chiang, C.M.Fortunko "Absorption of ultrasonic waves in air at high frequencies (10-20MHz)," *J. Acoust. Soc. Am.* **92**, 2006-2015 (1992).

[15] H.E. Bass, L.C. Sutherland, A.J. Zuckerwar, "Atmospheric absorption of sound: an update," *J. Acoust. Soc. Am.* **88**, 2019-2020 (1990).

[16] A. Safari, S. Davanzo, R.E. Newnham "Perforated PZT composites for hydrophone applications", *Ferroelectrics*, **49**, No. 1-4, 257, (1983).

[17] C. Richard, P. Eyraud, L.Eyraud, M. Richard, G. Grange, " 1.3.1 PZT-Polymer composites for high-pressure hydrophone application", *Ferroelectrics*, **134**, No.1-4, 59-64, (1992).

[18] D.R Bacon " Characteristics of a PVDF membrane hydrophone for use in the range 1-100 MHz", *IEEE Transactions on Sonics and Ultrasonics*, **SU-29**, No.1, 18-25, (1982).

[19] P.A. Lewin, "Miniature piezoelectric polymer ultrasonic hydrophone probes", *Ultrasoics*, **19**, 213-216, (1981).

[20] Y. Naskamura, T. Otani, "Study of Surface elastic waves induced on backing material and diffracted field of a piezoelectric polymer film hydrophone", *J. Acoust. Soc. Am.*, **94** (3), pt.1, 1191-1199, (1993).

[21] Y. Yiquan, S. Binwen, L. Zongjie " A new multi-planar PVDF standard hdrophone and its applications", *IEEE Transactions on Ultrasonics, Ferroelectrics, and Frequency Control*, **42**, No.5, 958-964, (1995).

[22] Y. Yiquan, S. Binwen, "A cylindrical hydrophone made of PVDF piezoelectric polymer and its performance", *Sensors and Actuators*, **35**, 231-234, (1993).

[23] B. Zeqiri, A.D. Bond, "The influences of waveform distortion on hydrophone spatial-averaging corrections-Theory and measurements", *J. Acoust. Soc. Am.* **92**(4), pt 1, 1809-1821, (1992).

[24] A.G. Bashford, D.W. Schindel, and D.A. Hutchins "Characteristics of Ultrasonic micromachined capacitance transducers in water", IEEE Trans. (*In press*).

CHAPTER 6

MATERIAL CHARACTERISATION USING AIR-COUPLED MICROMACHINED CAPACITANCE TRANSDUCERS.

6.1 Introduction

Non-destructive methods to characterise materials are largely based on using ultrasound, and there are some approaches that can achieve this without contacting the sample. Such methods include electromagnetic acoustic transducers (EMATs) [1], and laser generation [2]. However, EMATs require high current drivers, and must be placed close the surface, whereas with laser ultrasound high power lasers are needed to achieve adequate signal levels (in both generation and detection). Air-coupled ultrasonic capacitance transducers offer a range of advantages for this application including good sensitivity and wide bandwidth [3], and for the application of material characterisation careful alignment is not critical (as shown in the following experiment). Typically, air-coupled capacitance transducers have been primarily used for the non-destructive evaluation of engineering materials. Such applications include through-transmission, and guided surface wave imaging of polymeric and carbon fibre reinforced composite materials [4-6]. Only recently, air-coupled capacitance transducers have been used for characterising materials in terms of their elastic or viscoelastic properties [7-8].

Measurement of the elastic constants of composite materials has been achieved in the past using either contact or immersion ultrasonic techniques [9-15]. Elastic constant

measurements have also been performed using transducers in pulse-echo configuration [12,15], and by using acoustic resonance spectroscopy for short fibre and particulate reinforced composites [15]. Additionally, analytical methods exist for determining the elastic constants of composites, including the use of the Thomson-Haskell method for computing transmission / reflection coefficients through stratified media [16], which was also adapted to include anisotropic attenuation [17], and introduction of the Delta operator to improve numerical stability in multi-layered anisotropic plates (i.e. modelling the propagation of plane waves) [18]. Also, other published analytical methods include determining elastic constant in composites using a knowledge of the strain concentration factor, orientation dependent average fields [19], and also from separate knowledge of the elastic constants of the composite and matrix resin [20].

In the air-coupled system used here, two capacitance transducers were used, one acting as the source and the other as the receiver. Although air-coupled piezoelectric transducers could be used [21], the bandwidth for typical piezoelectric devices is limited. In contrast to this, capacitance transducers have a sufficiently wide enough bandwidth to be able to resolve the longitudinal and shear modes needed in the following experiment. Below is a description of how air coupled transducers were used to measure the elastic constants in a range of materials where contacting or immersion transducers could not be used. The principal operation of the experiment involves measuring the velocity of the through-transmitted quasi-longitudinal and shear modes as the sample is rotated, and optimising the match between these values and those predicted by theory. Additionally, the transmission coefficients of the samples were

also predicted in normal incidence again by optimal matching of values obtained both experimentally and theoretically.

The work was carried out in collaboration with Prof. B. Hosten, Department of Mechanics and Physics, University of Bordeaux, Bordeaux, France. The air-coupled transducers (used in chapter 3) were used on an existing system which was designed primarily for immersion ultrasonic characterisation of materials. The system uses high-precision equipment, and complex programming which had been developed over many years. Thus, replicating the experimental set-up for ourselves would not be viable. Instead the experiments were performed in Bordeaux with transducers and instrumentation developed as part of this research.

6.2 Theory

In orthotropic materials, stresses σ and strain ε are linked by the linear relationships [17,22]:

$$\sigma_i = C_{ij}\,\varepsilon_i. \qquad (1)$$

which define the stiffness matrix C_{ij}. This matrix has 81 components, but because of symmetry all the stresses and strains when the body are in equilibrium and are equal:

$$C_{ijkl} = C_{ijlk} = C_{jikl} = C_{jilk} \qquad (2)$$

thus, we can simplify the C_{ijkl} stiffness matrix to 36 constants. Typically, othotropic composites have three perpendicular planes of symmetry, and are often transversely isotropic [22]. The numbers of elastic constants are then reduced to 9:

$$Cij = \begin{bmatrix} c_{11} & c_{12} & c_{13} & 0 & 0 & 0 \\ & c_{22} & c_{23} & 0 & 0 & 0 \\ & & c_{33} & 0 & 0 & 0 \\ & SYM & & c_{44} & 0 & 0 \\ & & & & c_{55} & 0 \\ & & & & & c_{66} \end{bmatrix} \quad (3)$$

but for our case we are only going to find values for the elastic constants C_{11}, C_{22}, C_{66} and C_{12} in the P12 plane (normal to the fibres: $\phi=0^{\circ}$) and C_{11}, C_{33}, C_{55} and C_{13} in the P13 plane (parallel to the fibres: $\phi=90^{\circ}$), as shown in Figure 6.1 for a composite material.

6.3 Experimental determination of the elastic constants

6.3.1 Apparatus

The experimental arrangement used to determine the elastic constants is shown in Figure 6.2. The sample to be tested was mounted onto a high precision goniometer stage, with an angular resolution of 0.1 ° and the transducers were arranged at a distance of 40mm away from the sample one on each side for through-transmission experiment. The transducers were as described in earlier chapters, and consisted of a polished aluminium backplate with an array of 50μm diameter holes machined into the

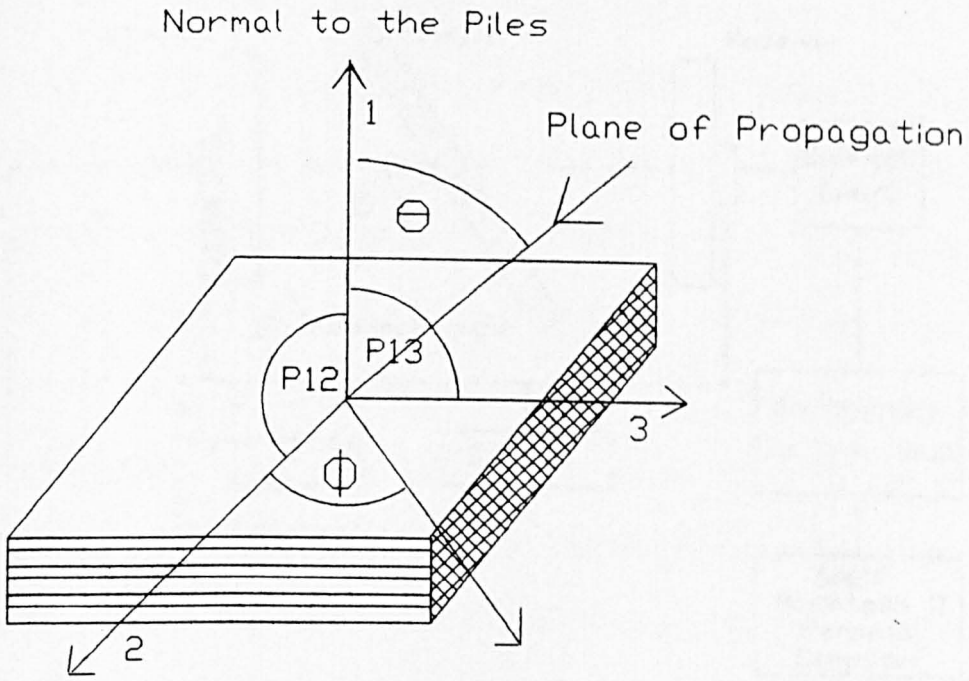

Figure 6.1 Planes of symmetry for a composite material

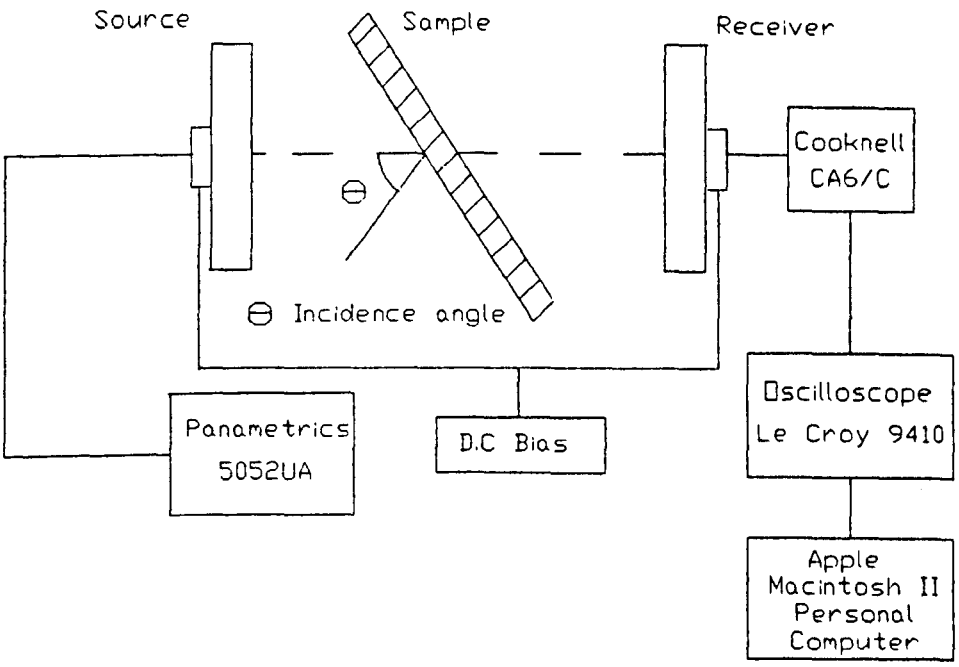

Figure 6.2 Schematic diagram of the experimental apparatus

surface, at a separation of 100μm with a 2.5μm polymer (Mylar) membrane. They were, however, larger than previously, in that both source and receiver were fitted with a 50mm diameter aperture (with a band width of 2MHz and sensitivity about 2X greater then the transducers used in chapter 3). These specially-made transducers were necessary, as the theory assumed that a plane wave was incident onto the sample. By making the aperture large, the receiver will be in the near field and thus would not be too sensitive to edge waves. The source was driven by a pulser (which produced a 200V negative polarity transient) with a 40V d.c. bias (typically, for Mylar a d.c. bias limit of 20V/μm is used to stop the membrane from polarising). This was applied between the membrane and the backplate. The receiver was connected to a charge amplifier which also supplied a 40V bias to the receiver. The amplified signal was digitised using an oscilloscope, while the data collection and the experimental equipment was controlled by a P.C. Note that, as the sample rotated, because of refraction the receiving transducer was displaced in a direction perpendicular to the axis of the emitted beam. This was to correct for displacement of the transmitted ultrasonic beam because of refraction at the two surfaces, and was calculated using Snell's law.

6.3.2 Results for a Glass-Epoxy Composite sample.

To determine the elastic constants using ultrasonic methods, no knowledge of the configuration of the layers within the samples is needed, but it is assumed that the layers are thin enough so as not to resonate at the highest frequency used (i.e. no multiple reflections within the thin layers will occur), and in the air-coupled system

used in these experiment this condition was satisfied. The only information needed was the density and thickness of the sample. For the series of experiments to follow, elastics constants were determined for the following four materials: a uni-directional 32 layer Glass-Epoxy, Epoxy with glass micro-spheres, green state injection moulded ceramic, and cardboard. Typically, apart from the Glass-Epoxy sample, to use liquid-coupled or contact methods would cause damage to the sample under test, making these materials ideally suited for air-coupled applications. The Glass-Epoxy sample was used as a means to validate the system using measurements from previous immersion experiments for the same sample.

The transmitted waveform (without the sample) is shown in Figure 6.3(a). Clearly, the transmitted signal has none of the ringing associated with piezo-electric devices and from the FFT shown in Figure 6.3(b), the useful bandwidth of the transducer system lies between 200kHz and 600kHz. This was used as the reference waveform in all of the experiments to follow. The sample was then placed between the transducers at normal incidence, and using signal averaging (1000 averages was typical), the received waveform was about 35mV as compared to the reference which was about 3V. The sample was rotated in 0.66° intervals, and at each incidence angle the through-transmitted waveform was recorded.

The transmitted waveform contained the quasi longitudinal (QL) and the quasishear (QT) components. Initially, at small angles of incidence, the quasi-longitudinal mode was dominant with the smaller quasi-shear mode following. As the angle of incidence increased, the amplitude of the quasi-shear mode also increased until it became was

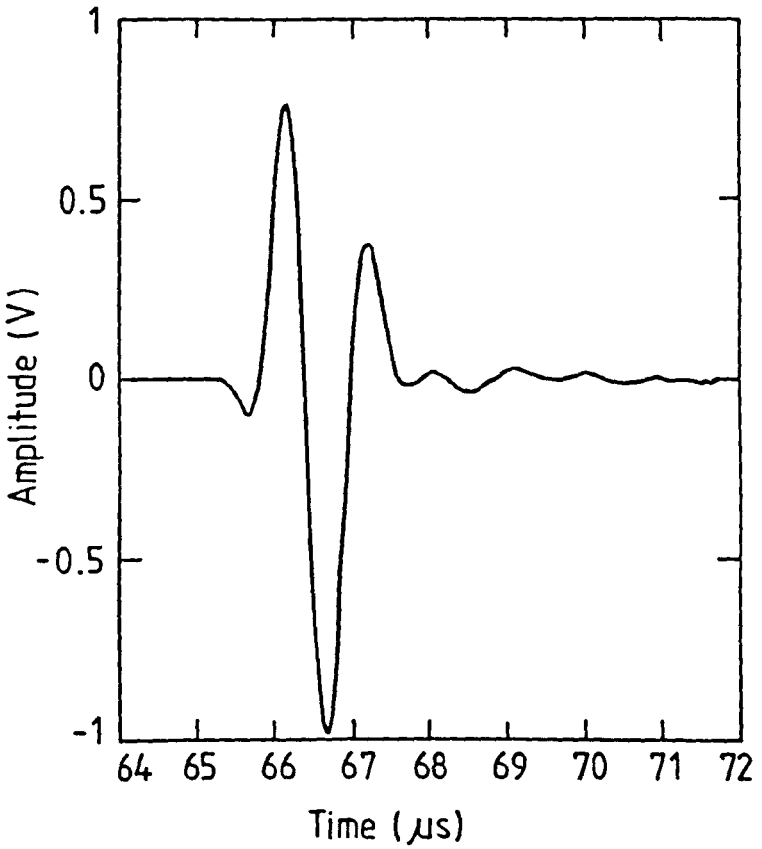

Figure 6.3(a) Transmitted waveform (without sample).

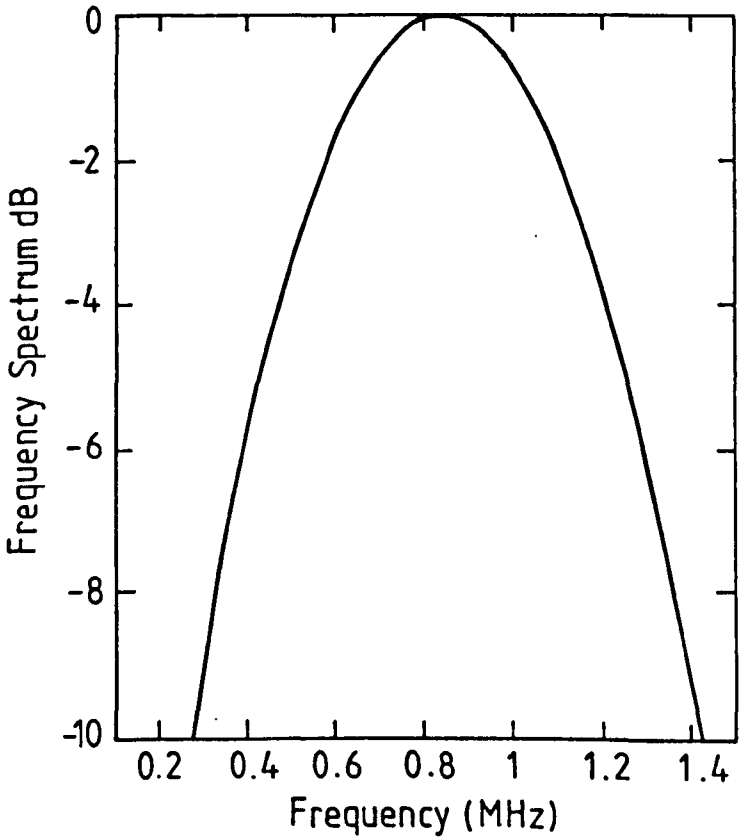

Figure 6.3(b) Frequency spectrum of transmitted waveform in 6.3(a).

dominant signal. It is important to know what modes are contained in the received signal. Before the experiment was performed, the angle of incidence of each sample was increased and the received signal monitored to determine a range of incidence angles where each mode can easily be identified and tracked. For the case of the Glass-Epoxy (UD-32 layer) sample the range was: 0-7° (P12 plane); 9-4° (P13 plane) for the QL mode and 9-15° (P12 plane); 4.5-12° (P13 plane) for the QT mode. Similarly, for the silicon nitride ceramic disk the range was: 0-6° (P12 and P13 plane) for the QL mode and 10-14° for the QT mode.

For each incidence angle, the time of flight of the received signal was measured for the QL and QT modes depending on the range, and cross-correlated with the reference signal. In this way the velocity could be reconstructed. For the Glass-Epoxy sample, a through transmission waveform incident onto the sample is shown in Figure 6.4(a), where the measured velocity with increasing incident angles for the P12 and P13 plane as shown in Figure 6.4(b) and 6.4(c) respectivley. Clearly, the QL mode has a higher velocity then the QT mode. By taking the reciprocal of the velocity (slowness) and resolving into the two planes, slowness (μs/mm) can be plotted for each direction in the P12 and P13 plane respectively. This is shown in Figure 6.4(d) and 6.4(e). An optimisation method was applied to the data, which determined the Cij values to give a best fit line through the QL and QT slowness data. The computed Cij values for the Glass-Epoxy sample are presented in Table 1:

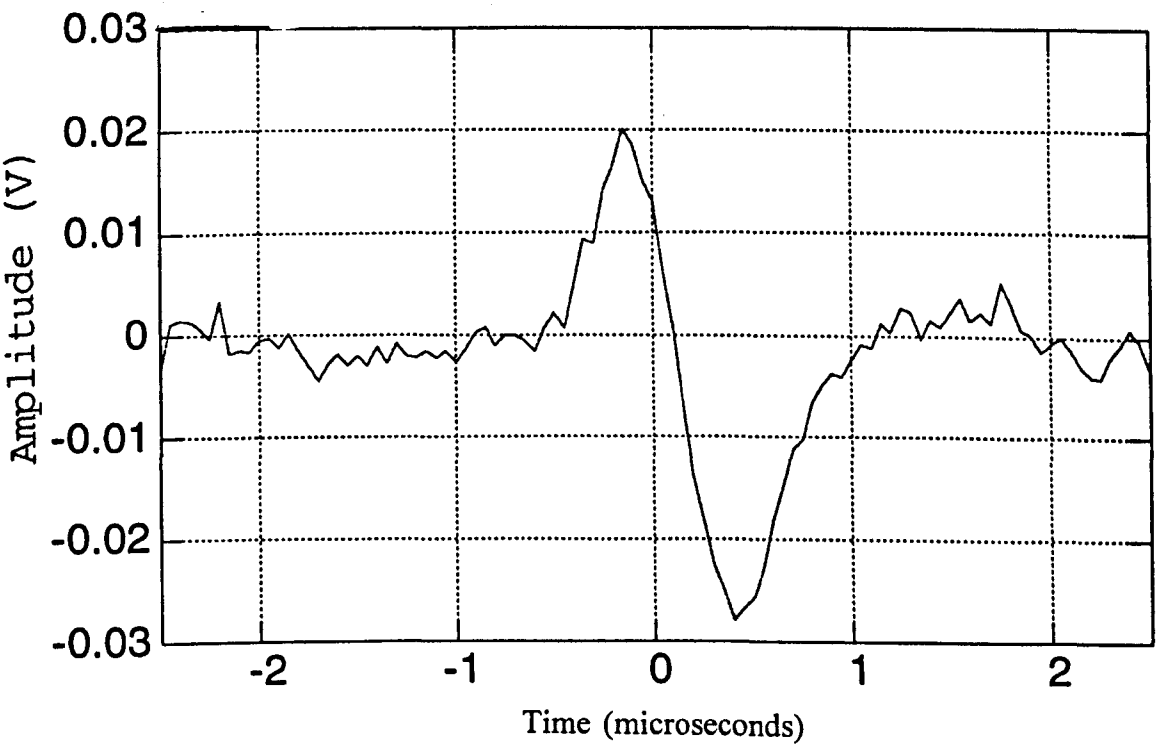

Figure 6.4(a) Through transmission waveform through a Glass-Epoxy (32 UD) sample in air.

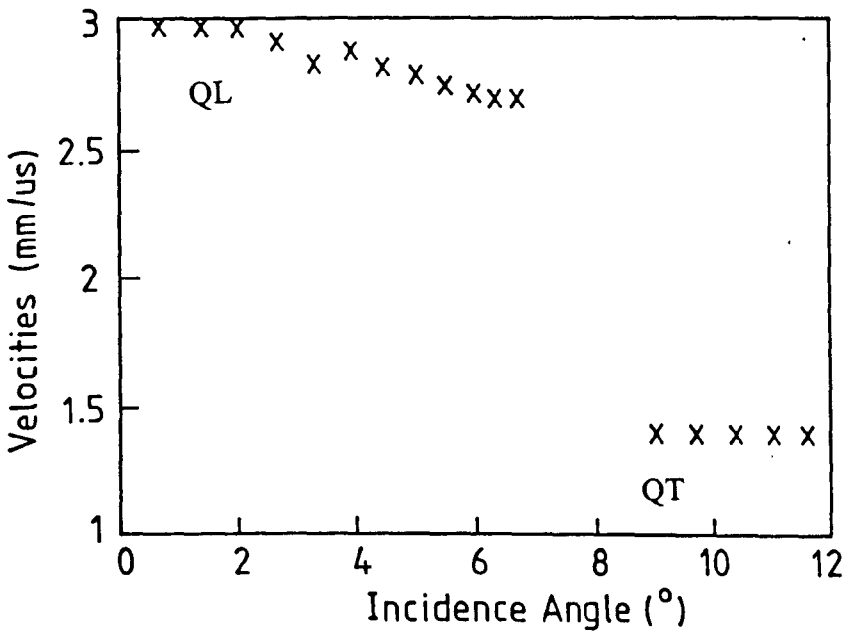

Figure 6.4(b) QL and QT velocity measurement for Glass-Epoxy sample in the P12 plane.

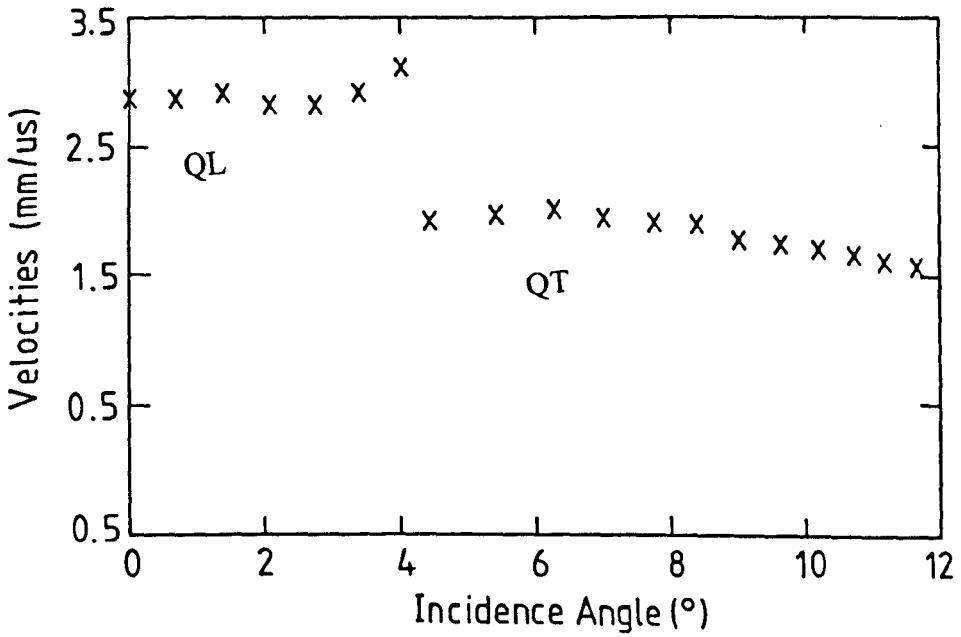

Figure 6.4(c) QL and QT velocity measurement for Glass-Epoxy sample in the P13 plane.

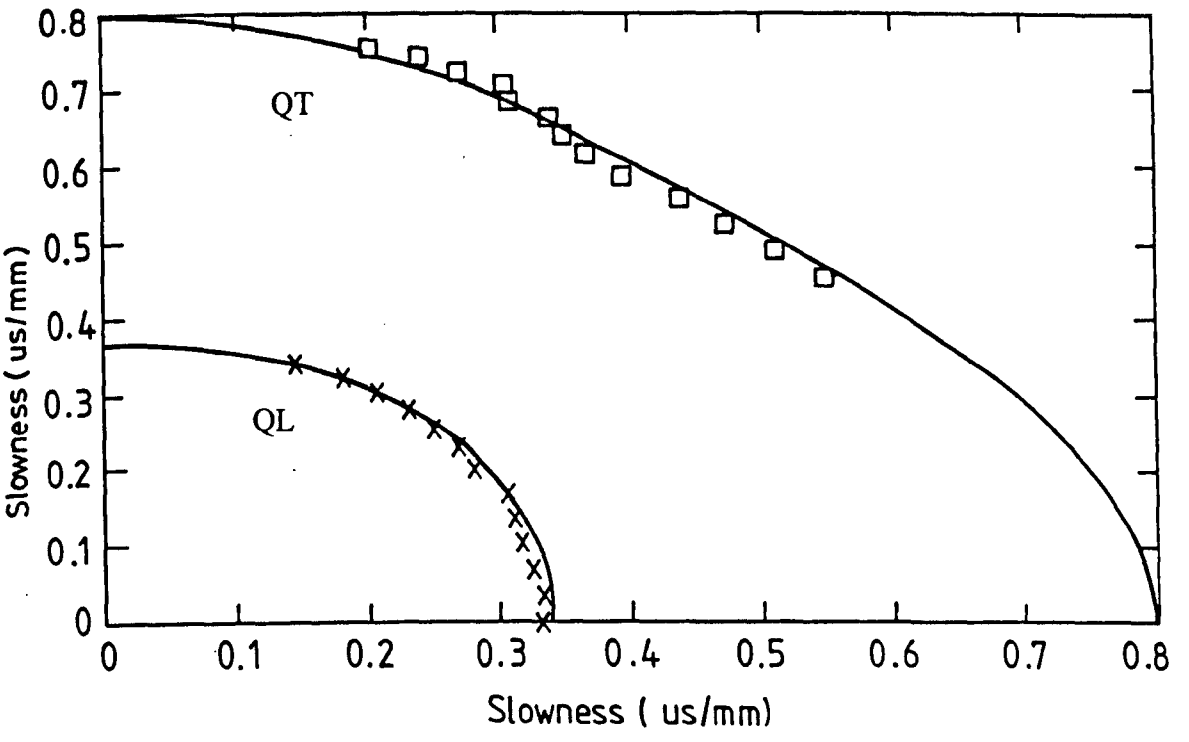

Figure 6.4(d) Slowness curve for Glass-Epoxy sample in the P12 plane.

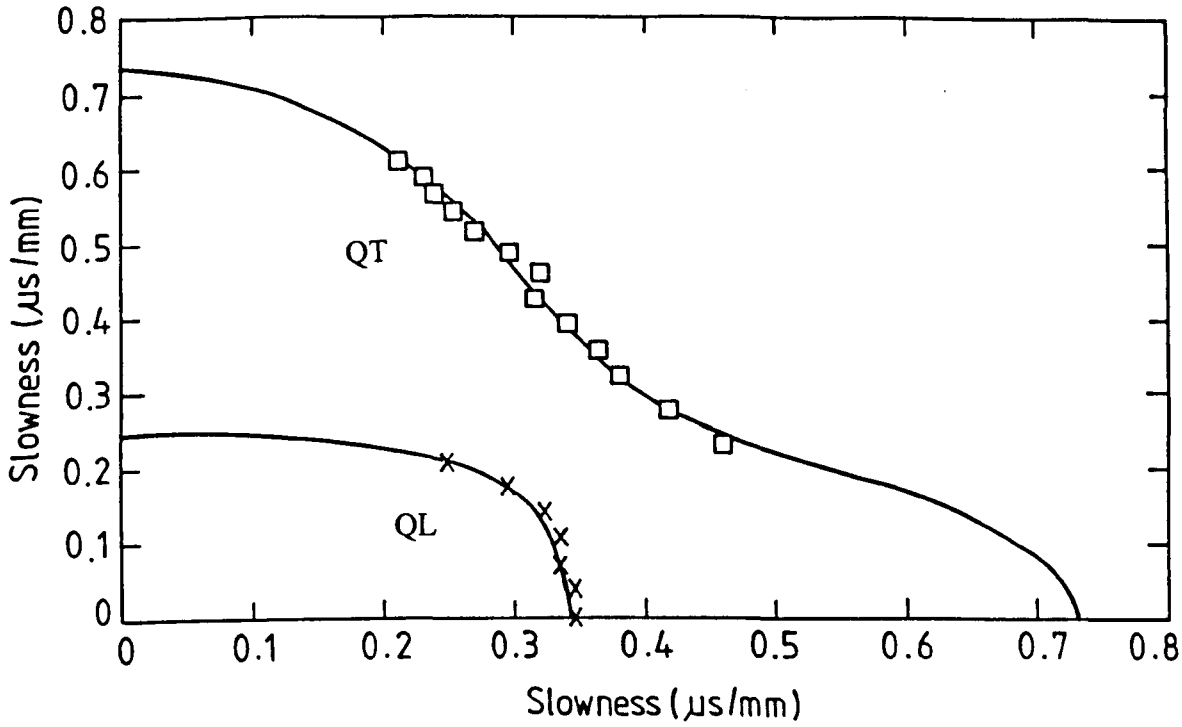

Figure 6.4(e) Slowness curve for Glass-Epoxy sample in the P13 plane.

Sample: Glass-Epoxy (UD 32)	Thickness mm	Density g/cm3	C_{11} GPa	C_{22} GPa	C_{66} GPa	C_{12} GPa	C_{33} GPa	C_{55} GPa	C_{13} GPa
Air	5.5	1.8	15.5	13.4	2.8	7.4	30.4	3.5	5.8
Water	-	-	15.0	15.0	3.5	8.0	44.8	3.9	8.5

Table 6.1

6.3.3 Results for two further samples

Again the same procedure was applied to determine Cij values for Resin-Epoxy with glass micro-spheres and green state injection moulded ceramic, with the QL and QT velocities shown in Figures 6.5(a) for the P12 plane, and 6.5(b) for the P13 plane, and the corresponding slowness curves shown in 6.5(c) and 6.5(d) respectively. Note: the P13 plane is identical to the P12 plane, because green state ceramic sample is isotropic (i.e. the properties are the same in all directions) Thus, only the velocities for the P12 plane are needed (that this applies to the resin-epoxy micro bubble sample), the slowness curve for which is shown in Figure 6.6. For all of the samples, the coupling medium was air at 20°C, and the real part of the elastic constants are given in Table 6.2

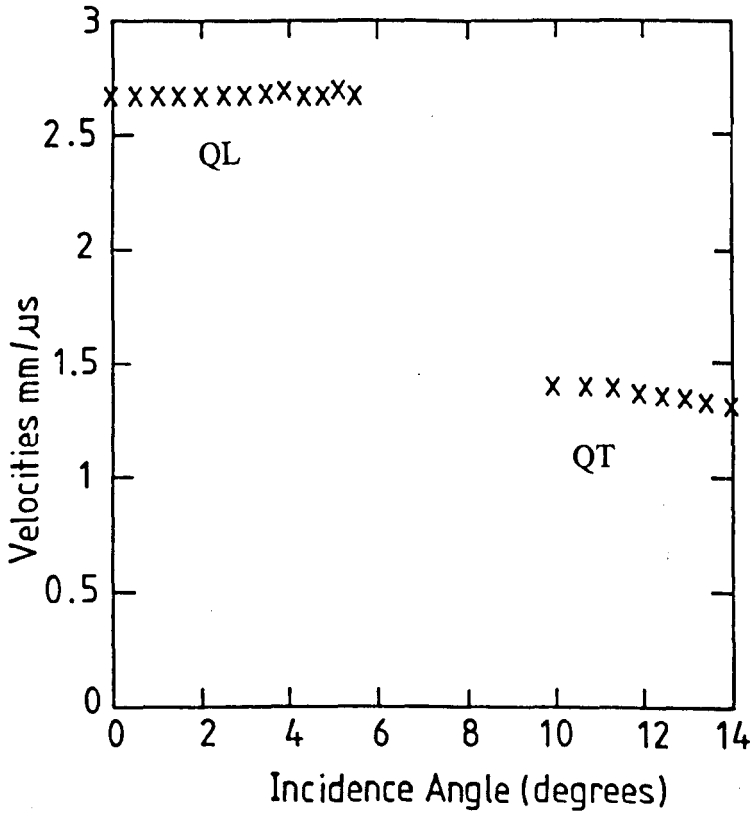

Figure 6.5(a) QL and QT velocity measurement for green state ceramic sample in P12 plane.

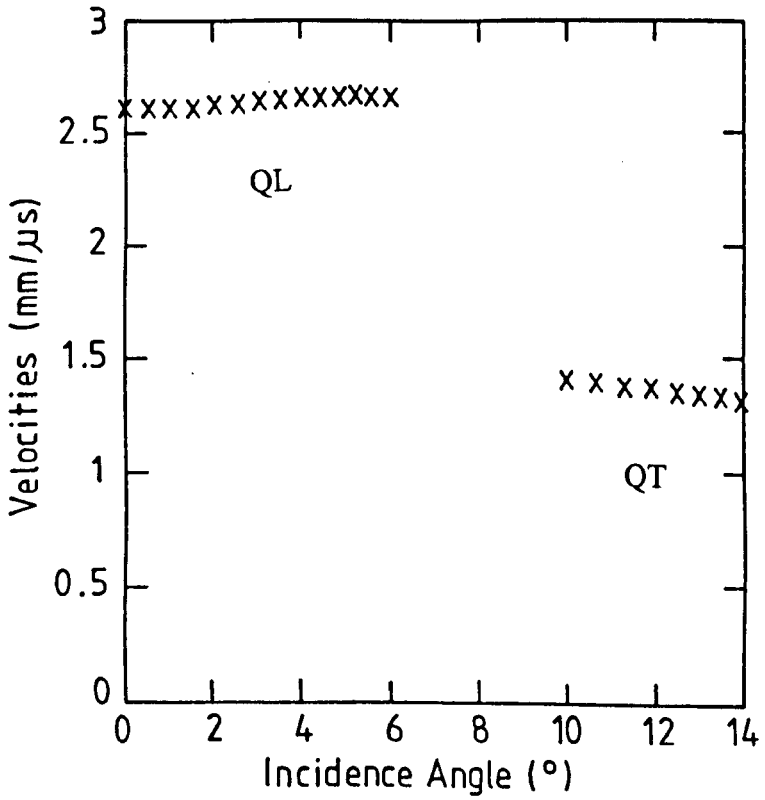

Figure 6.5(b) QL and QT velocity measurement for green state ceramic sample in P13 plane.

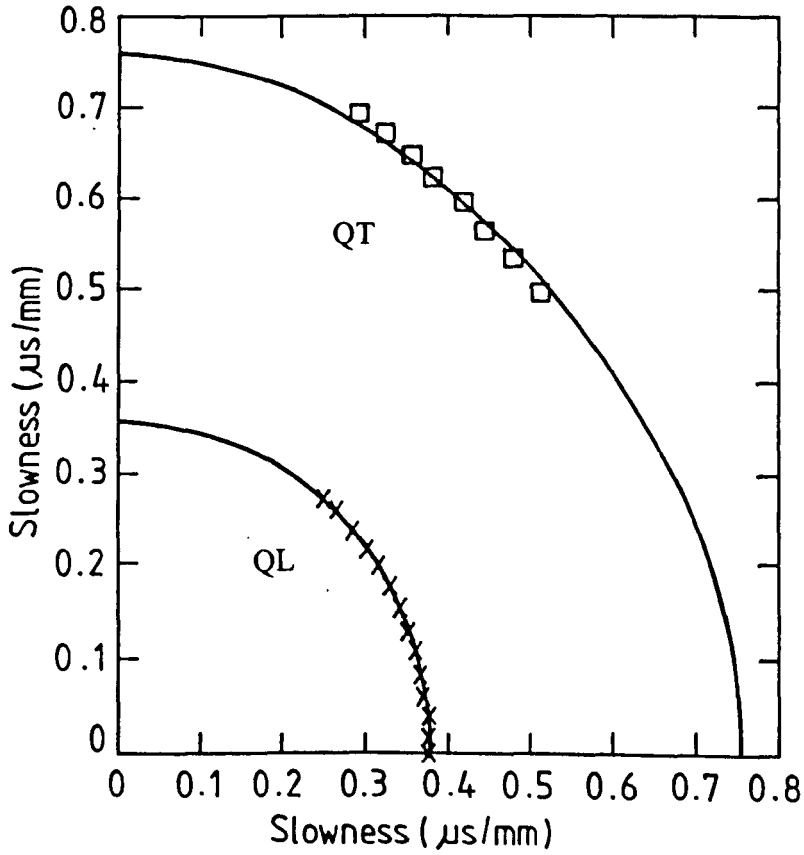

Figure 6.5(c) Slowness curve for green state ceramic sample in P12 plane

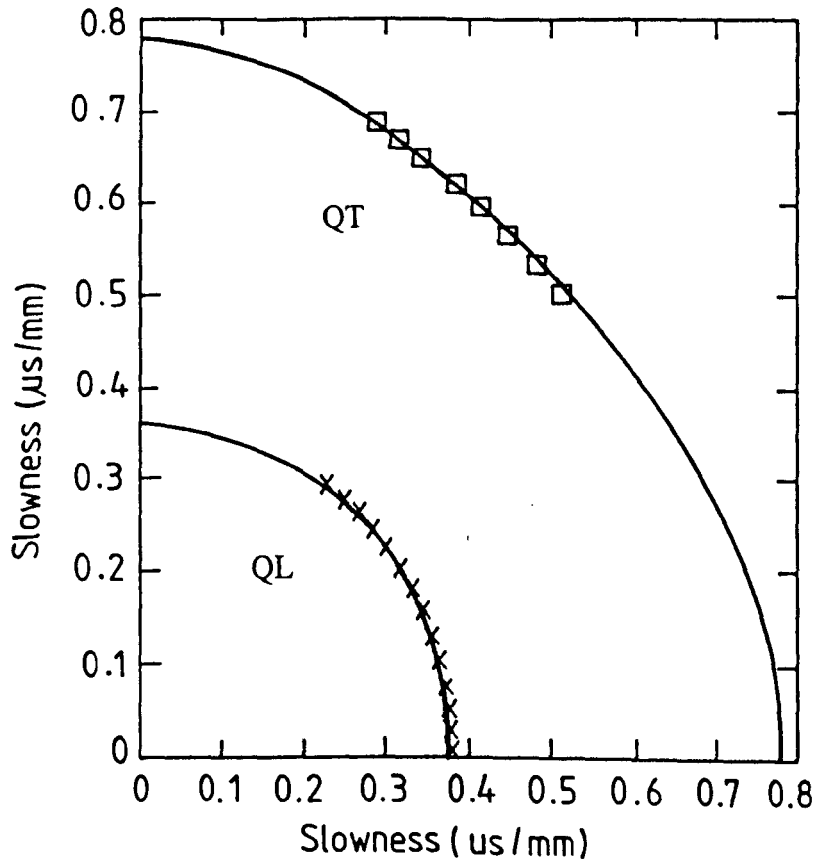

Figure 6.5(d) Slowness curve for green state ceramic sample in P13 plane

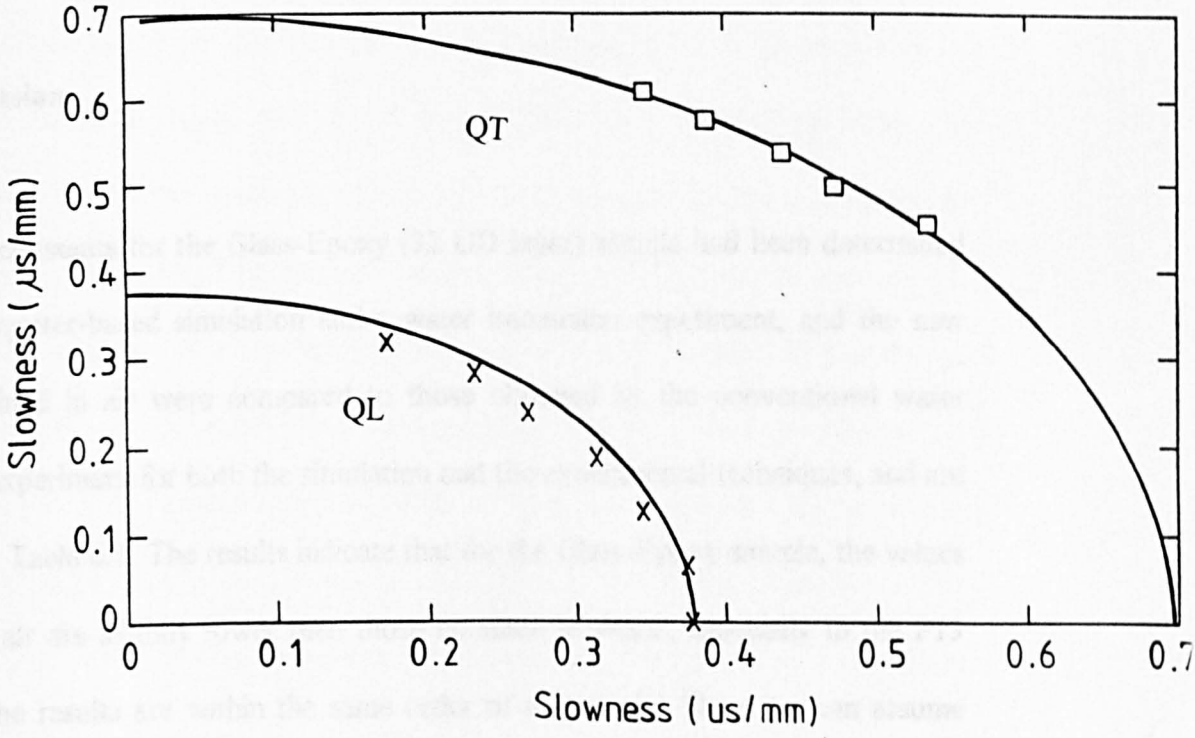

Figure 6.6 Slowness curve for resin-epoxy micro-bubble sample in the P12 and P13 plane (isotropic).

Sample	Thickness mm	Density g/cm3	C_{11} GPa	C_{22} GPa	C_{66} GPa	C_{12} GPa	C_{33} GPa	C_{55} GPa	C_{13} GPa
Resin-Epoxy /Glass μ bubbles	8.660	0.615	4.32	4.32	1.27	1.78	-	-	-
Green state Ceramic	2.92	1.76	12.3	14.0	3.1	6.4	-	-	-

Table 6.2

6.3.4 Discussion

The elastic constants for the Glass-Epoxy (32 UD layer) sample had been determined using a computer-based simulation and a water immersion experiment, and the new values obtained in air were compared to those obtained by the conventional water immersion experiment for both the simulation and the experimental techniques, and are presented in Table 6.1. The results indicate that for the Glass-Epoxy sample, the values obtained in air are slightly lower then those obtained in water, especially in the P13 plane, but the results are within the same order of magnitude. Thus, we can assume that the values obtained for the elastic constants of the Resin-Epoxy and the Green state ceramic samples in Table 6.2 can be treated as a good estimate. Possible systematic error which may occur when using the air-coupled technique is the measurement of the time of flight, two possible error are concerned here; the delay of the trigger from when time is zero, and when to determine the start of the received signal (as the pulse shape changes throughout the experiment). This is further

discussed in [11]. Also, this is further complicated by a low signal to noise ratio, and measurement of the velocity of the QL and QT modes may overlap. However, it is clear that the technique was succesful, and that the air-coupled capacitance transducers were able to provide good estimates of Cij for samples were water immersion would not be possible.

6.4 Eperimental determination of the elastic constants of thin samples using a transmission coefficient method.

To determine the elastic constants by the method described in 6.3.2, the sample under test needs to be thick enough for the QL and QT modes to be resolved within the working bandwidth of the transducer. However, when the samples are thin compared to the ultrasonic wavelength in the material, it is not possible to obtain separate QL and QT measurements. Thus, another approach has to be used. It might be possible to use other modes, such as lamb waves, but such measurements would be difficult. An alternative is to use the amplitude of the received through - transmitted signal instead of the time of flight data, as a function of angle [23] as a possible approach. In this section we will illustrate this by measuring the elastic constants of a 1mm thick cardboard sample.

6.4.1 Theory

By measuring the properties and characteristics of the through-transmitted waveform when using the air-coupled sample, and matching the result of a computed waveform

prediction, it is possible to estimate the elastic constants for cardboard by adjusting the values of the elastic constants in the transfer function. Typically, most commercial ultrasonic transducers have a limited beam section, and to satisfy the plane wave condition required by the theory [18], the source and receiver transducers were fitted with 50mm diameter aperture as before.

The transmitted waveform $s(t,\theta,\phi)$ is computed from the convolution product [7]:

$$s(t,\theta,\phi) = r(t) \otimes h(t,\theta,\phi), \tag{4}$$

Where $r(t)$ is the reference waveform and $h(t,\theta,\phi)$ is the transfer function (transmission coefficient).

6.4.2 Experiment

The cardboard was mounted onto the goniometer stage (Figure 6.1) and placed between the air-coupled transducers. Using the same apparatus set-up described in section 6.3.1, through transmission waveforms were recorded at normal incidence, 10°, and 20°. These time domain waveforms were Fourier transformed to give the frequency spectrum of the signals. Again, an optimisation method was used to simulate the frequency spectrum, by adjusting the transmission coefficient (i.e. elastic constants) to best match the received spectrum of the received through-transmitted waveform.

6.4.3 Results

Below, Table 6.3 shows the real Cij values needed to simulate the transmission coefficient of a cardboard sample, at 20°C.

Sample	Thickness mm	Density g/cm^3	C_{11} GPa	C_{22} GPa	C_{66} GPa	C_{12} GPa
Cardboard	1.7	0.281	0.020	0.020	0.013	0.002

Table 6.3

6.4.4 Discussion

The value obtained for C_{11} is near to that proposed in some scientific publications which analyse cardboards and papers with ultrasonic techniques [16]. The simulated and experimental frequency spectrums are shown in Figure 6.7(a) for normal incidence, 6.7(b) at 10°, and 6.7(c) at 20°. Clearly, the simulated spectrum is in agreement, however the amplitude is less than expected. By performing an inverse Fourier transform, the time domain through transmitted signals were obtained. The experimental and simulated waveforms are shown in Figure 6.8(a), and 6.8(b) respectively for normal incidence, which also are in agreement.

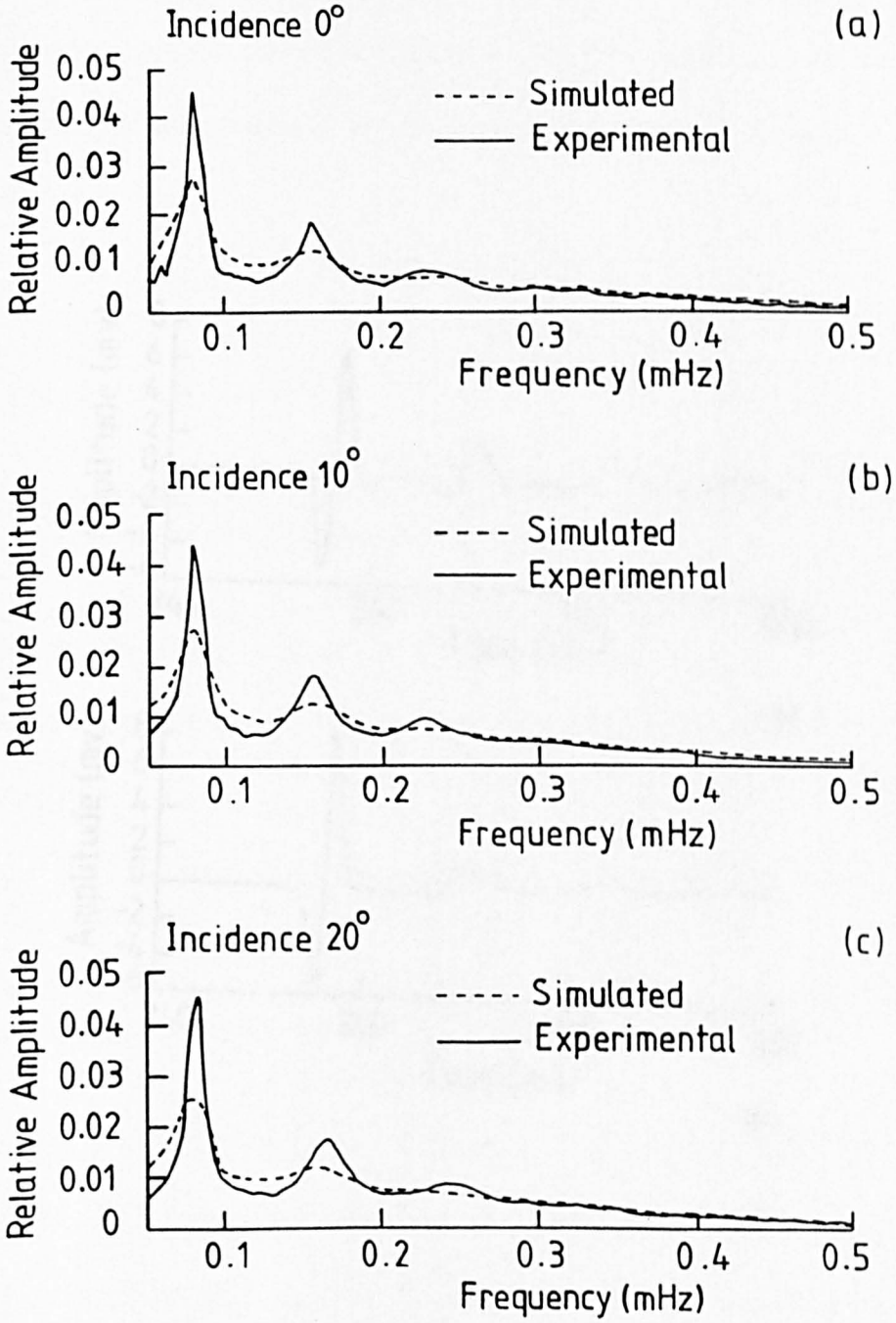

Figure 6.7 Simulated and experimental frequency spectrum at (a) normal, (b) 10° and (c) 20° incidence.

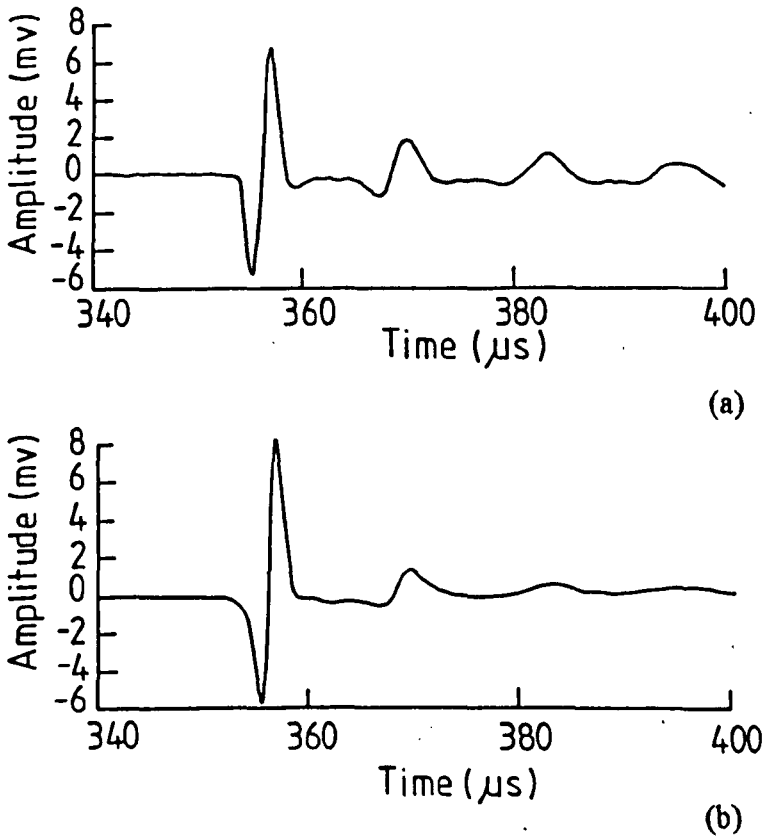

Figure 6.8 (a) Experimental, (b) Simulated waveform in the cardboard sample.

6.5 Conclusion

From the experiments described, it is evident that air-coupled capacitance transducers are ideal for non-contact material characterisation of a range of engineering materials. Also, the application was extended to cover materials which would be damaged if immersed in liquid.

6.6 References

[1] M. Hirao, H. Ogi, H. Fukuoka, "Resonance EMAT system for acoustoelectric stress measurement in sheet metals", *Rev. Sci Inst.* **64**, 1993, 3198-3205.

[2] J.P Monchalin and J.D. Aussel, "Precision laser-ultrasonic velocity measurement and elastic constant determination", *Ultrasonics*, **27**, 1989, 165-177.

[3] D.W. Schindel, D.A. Hutchins, L.Zou, and M Sayer, "The design and characterization of micro machined air-coupled capacitance transducers" IEEE Trans, UFFC, 1995, **42**, 51-58.

[4] D.W. Schindel, D.A. Hutchins, "Through thickness characterisation of solids by wideband air-coupled ultrasound", *Ultrasonics*, Jan 1995, **53** (1), 11-17.

[5] D.A. Hutchins, W.M.D. Wright, and D.W Schindel, "Ultrasonic measurements in Polymeric materials using air-coupled transducers", J. Acoust. Soc. Am. 99, 2116-2123.

[6] L.P. Scudder, D.A. Hutchins, N.Q. Guo "Laser generated ultrasonic guided waves in
fibre reinforced plates" *IEEE Trans. UFFC 1996*, **43**, No 5. 870 - 880.

[7] B. Hosten, D.A. Hutchins, D.W. Schindel "Measurement of elastic constants in composite materials using air-coupled ultrasonic bulk waves" *J.Acoust.Soc.Am* **99** (4) Pt. 1, April 1996.2116-2122.

[8] A. Safaeinili, O.I. Lobkis, and D.E. Chimenti, "Air-Coupled Ultrasonic Estimation of Viscoelastic Stiffnesses in Plates", *in press.*

[9] A.H. Nayfeh, and D.E. Chimenti, "Ultrasonicwave reflection from liquid-coupled orthotropic plates with application to fibrous composites" *J. Appl. Mech.* **55**, 1988, 863-870.

[10] B.Hosten, "Reflection and Transmission of acoustic plane waves on an imersed orthotropic and viscoelastic solid layer", *J.Acoust.Soc.Am.* **89** (6), June 1991, 2745-2752.

[11] H.J. Jeong, D.K. Hsu, R.E. Shannon, and P.K. Liaw "Characterization of anisotropic elastic-constants of silicon carbide particulate-reinforced Aluminium metal-matrix composites (Experiment)" *Metallurgical and Materials Transactions A-Physical Metallurgy and Materials Science*. **25**, No.4, 1994, 799-809.

[12] A. Minachi, D.K. Hsu, and R.B. Thompson, "Single sided determination of elastic constants of thick composites using acoustoultrasonic technique", *J. Acoust. Soc. Am*, **96** (1), 1994, 353-362.

[13] P.W.A. Stijnman, "Determination of the elastic-constants of some composites by using ultrasonic velocity measurements", *Composites*, **26** (8), 1995, 597-604.

[14] M. Orrhede, R. Tolani, and K. Salama, "Elastic constants and thermal-expansion of aluminium SIC metal-matrix composites", *Research in Nondestructive Evaluation*, **8** (1), 23-37.

[15] M.L. Dunn, H, Ledbetter, P.R. Heyliger, and C.S Choi, " Elastic constants of textured short-fiber composites", *J. Mech. and Physics of Solids*, **44**(9), 1996, 1509.

[16] B. Hosten ,"Bulk heterogeous plane waves propagation through viscoelastic plates and stratified media with large of frequency domain", *Ultrasonics.* **29**, November 1991, 445-450.

[17] B. Hosten, M.Castaings, "Transfer matrix of multilayered absorbing and anisotropic media. Measurements and simulations of ultrasonic wave propergation through composite materials" *J.Acoust. Soc. Am* **94** (3), pt 1, Sept. 1993, 1488-1494.

[18] M. Castaings, and B. Hosten, "Delta operator technique to improve the Thomson-Haskell-method stability for propagation in multi layered anisotropic absorbing plates" *J.Acoust. Soc. Am.* **95** (4), April 1994, 1931-1940.

[19] H.J. Jeong, D.K. Hsu, R.E. Shannon, and P.K. Liaw "Characterization of anisotropic elastic-constants of silicon carbide particulate-reinforced Aluminium metal-matrix composites (Theory)" *Metallurgical and Materials Transactions A-Physical Metallurgy and Materials Science*. **25**, No.4, 1994, pp 811-819.

[20] A.P Wilczynski, I.M. Ward, P.J. Hine, "Bounds for the elastic constants of reinforcing fibers in polymeric composites", *J. Mat. Sci.* **30** (23), 1995, 5879-5884.

[21] W.M.D. Wright, D.A. Hutchins, G. Hayward, A. Gachagan "Ultrasonic-imaging using laser generation and piezoelectric air-coupled detection", *Ultrasonics*, **34**,1996, 405-409.

[22] D. Hull and T.W Clyne, "An Introduction to Composite Materials", Cambridge Solid State Science Series, 2nd Edition, 1996, Cambridge Univeristy press.

[23] D.E. Chimenti, A.H. Nayfeh, "Ultrasonic wave reflection and guided waves in fluid-coupled composite laminates", *J. Nondestr. Eval.* **9**, 1990, 51-69

[24] T.D. Gerhardt, "External pressure loading of spiral tubes: Theory and Experiment",*J. Eng. Mat & Tech*, **112**, April 1990, 144-150.

CHAPTER 7

NON-DESTRUCTIVE EVALUATION OF GREEN-STATE CERAMICS USING MICROMACHINED AIR-COUPLED CAPACITANCE TRANSDUCERS

7.1 Introduction

Green-state ceramics are materials which have been formed into a pre-determined shape by slip-casting, injection moulding, or by some other method [1]. The ceramic particles are held together by various mechanisms, including the use of polymer-based binders, so that the material can be handled conveniently before the firing stage. In the case of slip-casting in particular, the result is often a material that can be easily damaged mechanically, and which would be contaminated by the application of any liquids that might be used as a fluid couplant. Thus, the availability of a non-contact inspection technique for the inspection of green-state ceramics during manufacture has distinct advantages, so that the use of contaminating couplant is eliminated. There have been several approaches to this problem described in the literature. The conventional method of testing is the C-scan, with the sample immersed in a fluid and the reflected signal analysed in terms of amplitude [2] or changes in acoustic velocity [3]. However, ceramics such as silicon nitride [4] cannot be tested using water immersion, and hence dry coupling methods have been attempted, e.g. by protecting the sample with a vacuum-sealed

polymer membrane [5], an adhesive tape [6] or a silicone gel couplant [7]. However, none of these methods could be used at elevated temperatures, which is a requirement if green-state samples are going to be monitored during subsequent processing, such as during the burn-out of polymer binder. There has been some work on wheel-contact transducers and oblique airborne waves [8], but these techniques could either not be used on fragile specimens, as is the case with green-state silicon nitride, or could not generate longitudinal waves.

An alternative approach is to use a method by which materials can be tested ultrasonically both without contact and at high temperatures. Laser irradiation and interferometric detection can be used on some ceramic samples with suitable surfaces [9], although ceramic surfaces are usually highly scattering, and not suitable for optical techniques. In addition, interferometry [10] can be very expensive and difficult to apply at elevated temperaures. Direct laser irradiation, as used in pulsed laser generation and high-intensity interferometers, can also damage surfaces, especially the low melting-point polymer binders used for green-state ceramics. Other methods such as the use of EMATs [11] require electrically conducting surfaces, and are not applicable to most polymer-based materials.

The approach used here is to utilise the low acoustic impedance of green-state ceramics, which makes them a suitable candidate for testing with air-coupled ultrasound. This low impedance is caused by the use of low melting point, wax-based polymers for binding purposes, especially in injection-moulded samples. For slip-casting, there is also a high porosity in the green-state, with a reduced

proportion of polymer binder, making their impedance even lower than for injection-moulding. There is thus good transmission acrosss the air/sample interfaces in comparison to other solid materials.

Previous investigations have shown that voids and cracks within injection-moulded ceramics are very much dependent on the fabrication process. It is found that the pressure used to force the ceramic into the mould is critical [12], as too little causes voids and too much causes internal residual stresses. An analytical method exists [13] which calculates the time taken for the pressure in the centre of the sample to reach zero, and this should be less than the time needed for the centre of the sample to solidify, hence avoiding the formation of voids. Also, thermal expansion measurements can be taken in different direction for an injection moulded green state ceramic to study the formation of voids and cracks [14]. Additionally, the influence of organic binders on the microstructures of silicon nitride have been discussed in [14,15]. As can be seen, there are many factors which affect the variability of an injection-moulded ceramic, and air-coupled ultrasonic nondestructive testing was thus chosen to study the problem.

7.2 Air-Coupled through transmission

The first experiments were designed to determine if air-coupled transducers can be used to determine any varability within the same manufacturing technique between the resonant frequencies of the disc-shaped samples, using a through-transmission arrangement which has been used in various other experiments for polymer-based

composites [16-19]. thus, providing a quick non-contact method to determine if a green state ceramic disk is sutible for firing. A schematic diagram of the experimental arrangement is shown in Figure 7.1. To perform these experiments, the transducers used were based on an existing micromachined capacitance design [18], but fitted with a 5 μm thick metallised Mylar membrane The transducers were driven by a pulser. A 100V d.c. bias was also supplied between the backplate and the membrane for both the source and receiver. With the receiver connected to a charge amplifier, the system had a bandwidth in excess of 500kHz, which was sufficient for the present measurements. Each sample (50mm diameter 3mm thick) was placed onto a 100mm square, 5mm thick perspex holder with a 47mm diameter hole drilled in the centre, as shown in Figure 7.2, thus allowing the through-transmitted signal to be easily distinguished from that caused by ultrasound travelling around the edge of the sample, with an air-coupled transducer placed on each side.

Through transmission waveforms were obtained for samples manufactured by injection moulding, slip-casting, and 6 &15 ton die-pressing. A typical through-transmitted wavefrom is shown in 7.3(a) for the injection moulded sample, with the corresponding frequency spectrum shown in 7.3(b). Again, for the slip-cast, and 6 & 15 ton die-pressed samples a typical waveform is shown in Figure 7.4(a), 7.5(a) and 7.6(a) respectively, with the corresponding frequency spectrums shown in 7.4(b), 7.5(b), and 7.6(b). Five samples were tested for each manufacturing technique, and the resonances obtained from the frequency spectrums are presented in Tables 7.1-7.3, where f_1 is the fundamental frequency and f_2,f_3 are the second and third harmonic respectively.

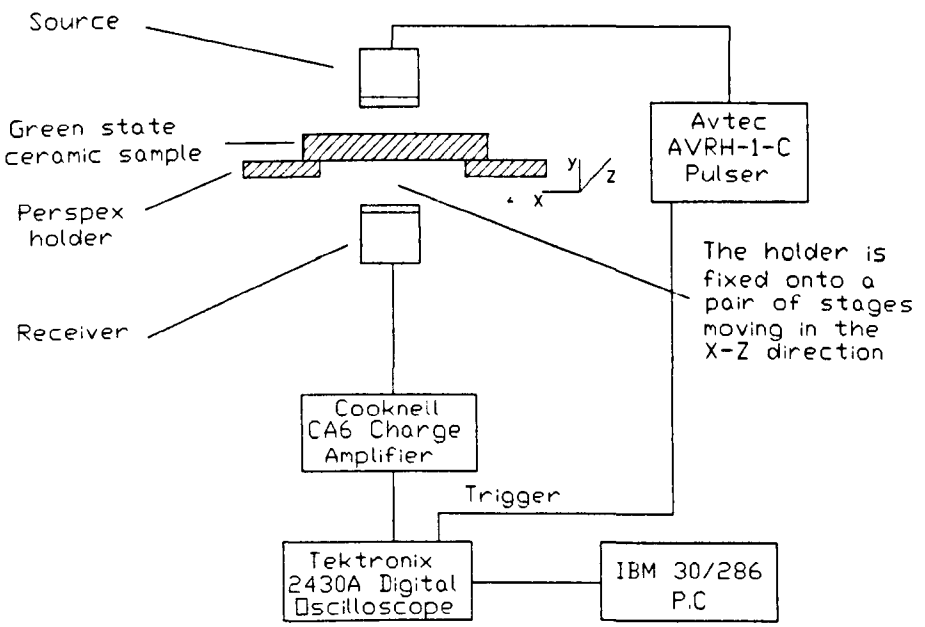

Figure 7.1. Schematic diagram of the experimental arrangement for through transmission and c-scan experiment

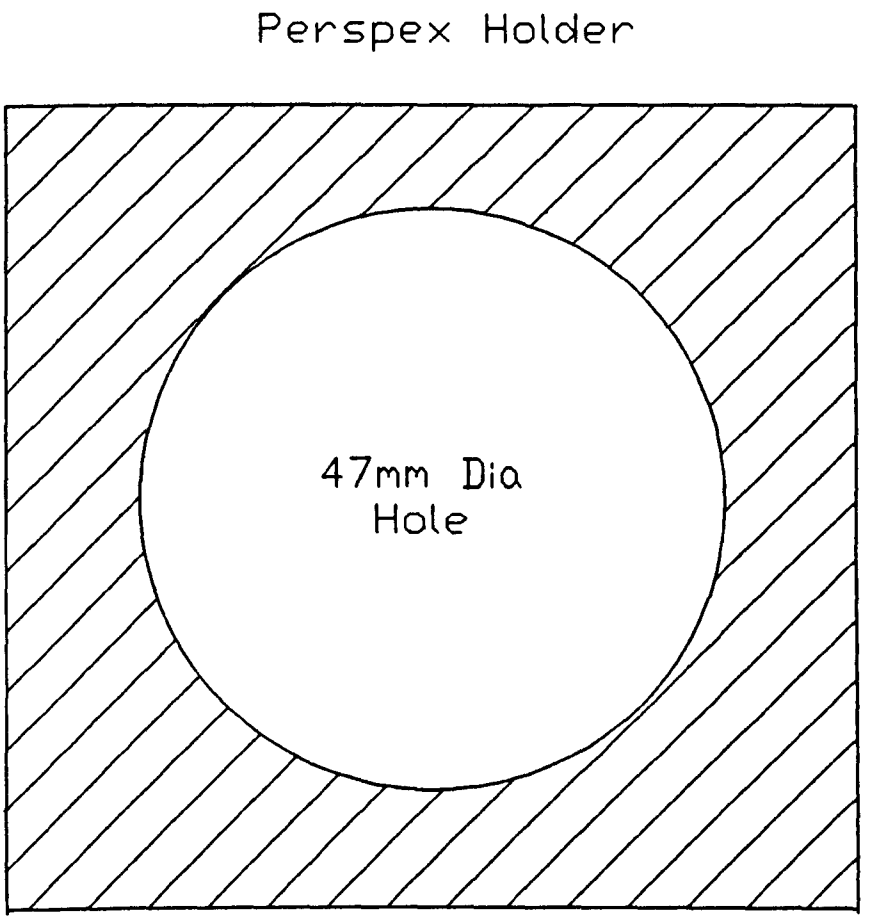

Figure 7.2. Perspex holder used to hold the ceramic samples

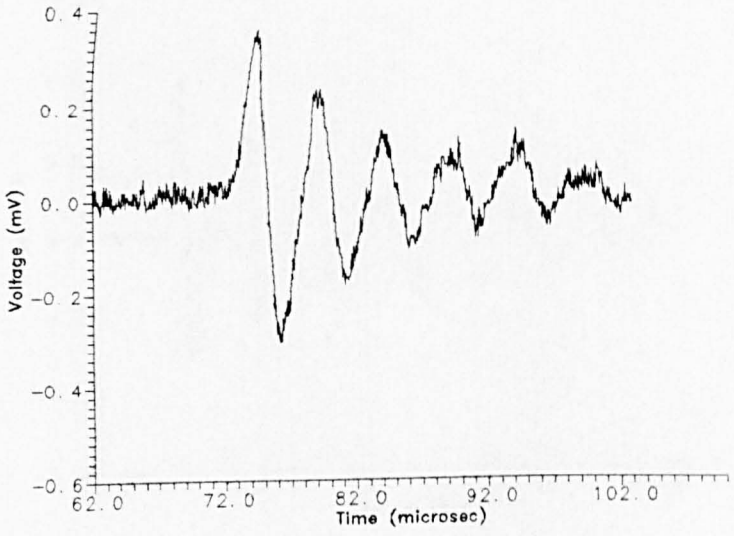

(a)

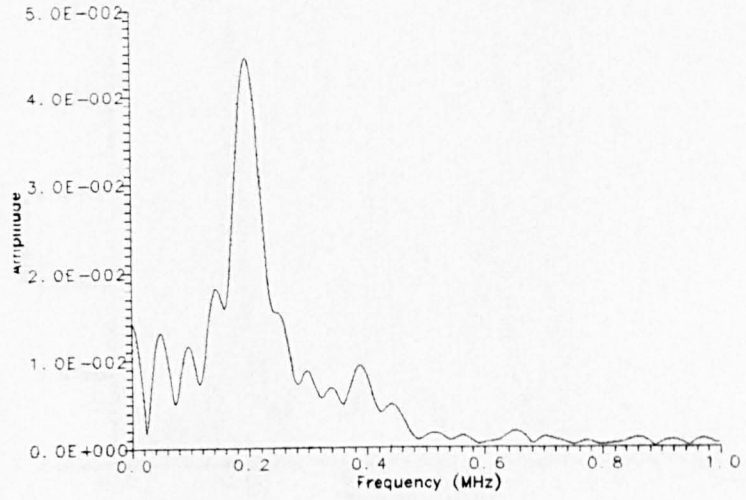

(b)

Figure 7.3. (a) Through transmitted waveform, (b) frequency spectrum, through an injection moulded green state ceramic.

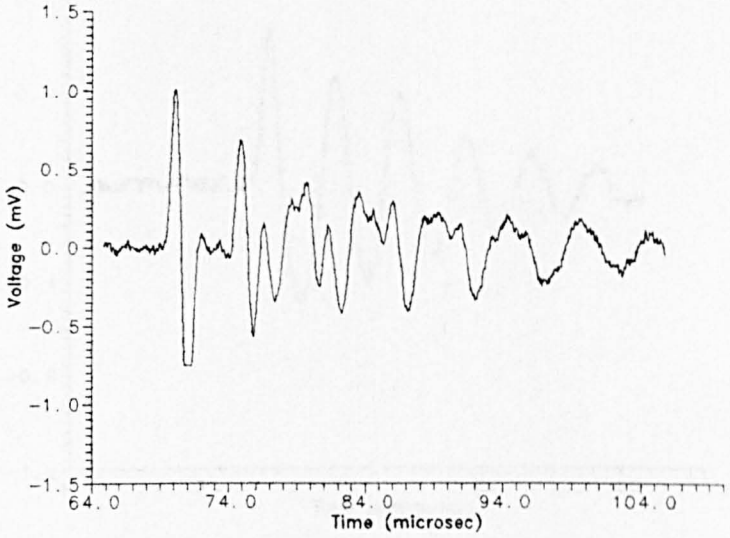

(a)

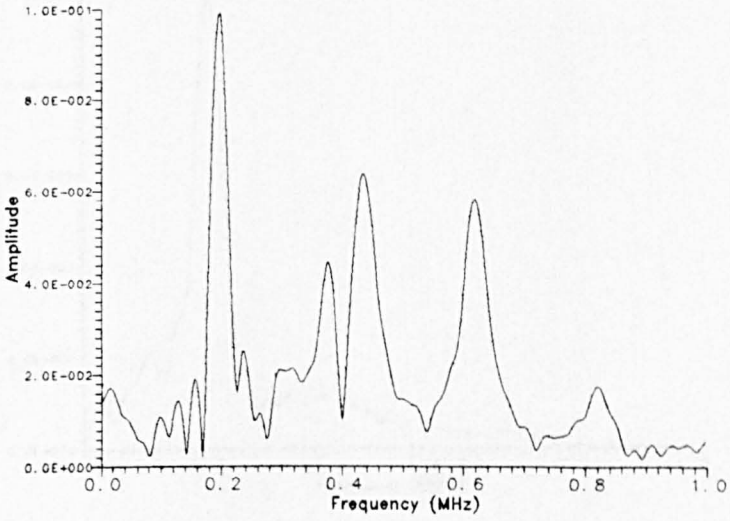

(b)

Figure 7.4. (a) Through transmission waveform, (b) frequency spectrum, through a slip-cast silicon nitride green state ceramic.

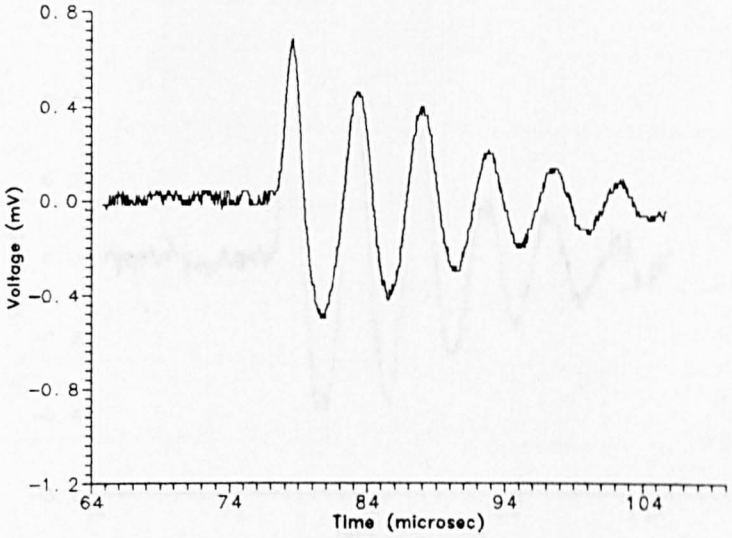

(a)

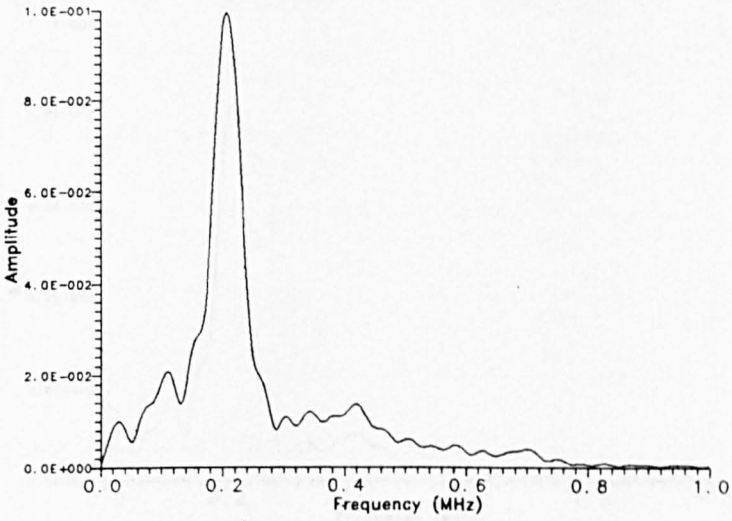

(b)

Figure 7.5. (a) Through transmitted waveform, (b) frequency spectrum, of a 6 ton die-pressed silicon nitride green state ceramic.

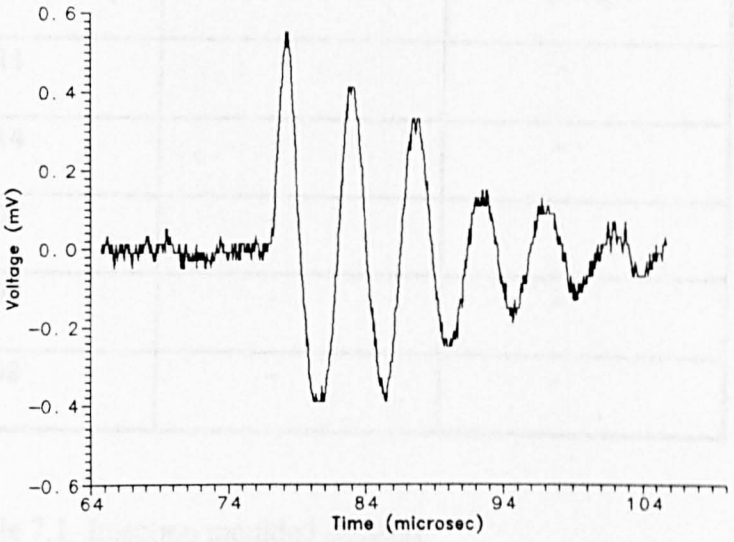

(a)

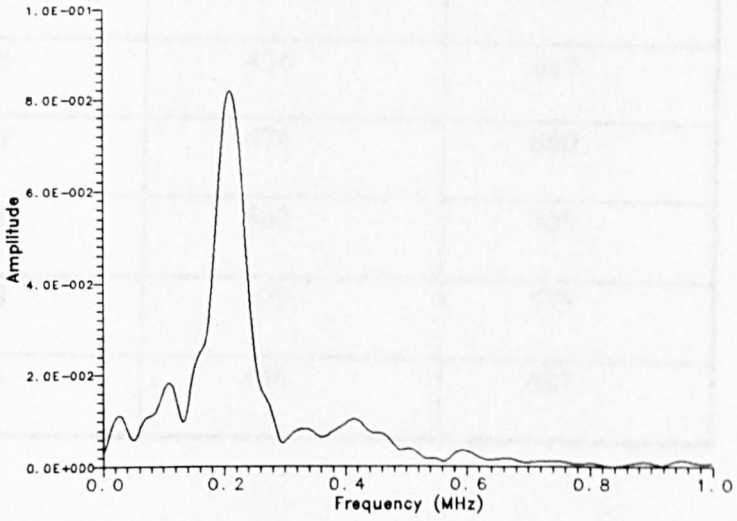

(b)

Figure 7.6. (a) Through transmitted waveform, (b) frequency spectrum, of a 15 ton die-pressed silicon nitride green state ceramic.

Sample	f1 (kHz)	f2 (kHz)	f3 (kHz)
1	211	-	-
2	214	-	-
3	207	-	-
4	198	-	-
5	108	-	-

Table 7.1. Injection moulded samples.

Sample	f1 (kHz)	f2 (kHz)	f3 (kHz)
1	198	436	619
2	204	476	680
3	213	500	705
4	198	399	573
5	183	446	637

Table 7.2 Slip-cast sampes.

Sample	f1 (kHz)	f2 (kHz)	f3 (kHz)
1	207	-	-
2	216	-	-
3	213	-	-
4	213	-	-
5	204	-	-

Table 7.3. 6 ton die-pressed sample.

Sample	f1 (kHz)	f2 (kHz)	f3 (kHz)
1	210	-	-
2	210	-	-
3	219	-	-
4	210	-	-
5	210	-	-

Table 7.4. 15 ton die-pressed sample.

Comparing the five samples tested for each production method, the injection moulded and slip-cast samples showed the greatest variability in resonant frequency. With these production methods the ceramic particles are not formed with a significant pressure, hence variability due to voids within the sample are most likely.

Clearly, from the slip-cast samples, there was information transmitted at frequencies in excess of 800kHz. This was mainly due to the low compression forces, so that the samples had a higher porosity which further reduced the impedance, as clearly shown from the frequency spectrum of Figure 7.4 in which the second and third harmonics are present..

The die-pressed samples produced the least amount of variability in the resonant frequency. This was expected, as again the higher die pressure (6 and 15 tons) reduced the variability of the voids. However, these samples did not contain any polymer binder and thus were extreamly fragile.

7.3 Air-Coupled C-Scan imaging

The bulk of the air-coupled C-scan imaging measurements were performed using silicon nitride injection-moulded samples, due to the difficulty in adding artificial defects to slip-cast samples. Each disc-shaped sample was 3mm thick, 50mm in diameter, and contained 10% by weight organic PMMA polymer binder. Additional samples of the same dimensions, manufactured by die pressing at 6 tons, were scanned, These contained similar amounts of binder.

For C-scanning, the injection-moulded green-state sample was placed one a perspex plate (see Figure 7.2). The perspex plate was placed horizontally between the source and receiver transducers, which were positioned vertically at a separation of approximately 50mm. The transducers were themselves attached to a pair of

translation stages, so that they could be scanned across the sample at a spatial resolution of 1mm in the X and Z directions, with the scan area being 50mm x 50mm. Scanning was achieved by using a computer controlled system which consisted of an IBM PC controlling a Tektronix 2430A digital oscilloscope and a scanning stage. Images were obtained by recording the peak amplitude in a time window, incorporating the through-transmitted signals. This was done off-line, after a waveform was recorded in each spatial location.

C-scan images are presented in Figure 7.7 for four green-state samples. The first was a 50mm diameter injection moulded green state ceramic sample, as received from the manufacturers (Ceram Research Ltd). As will be seen in Figure 7.7(a), the resultant image is reasonably uniform throughout the central section, but there is a region around the perimeter of the sample of a lower amplitude. This arises when the finite beam size, emitted by the10mm diameter transducer aperture, interacts with the edge of the sample. This could be improved by using a focussed device, which will be the subject of future development. This image can be compared to that resulting from scanning a second sample, shown in Figure 7.7(b), where a 5mm diameter recess has been machined into the back surface of the material. The machined region is clarly visible in the image, although the feature appears slightly larger in the image than is the case in reality. This again is mainly due to the finite beam size from the air-coupled devices.

Three further samples were investigated in the imaging experiments. The first is a sample in which widespread cracking had been induced by cooling quickly from

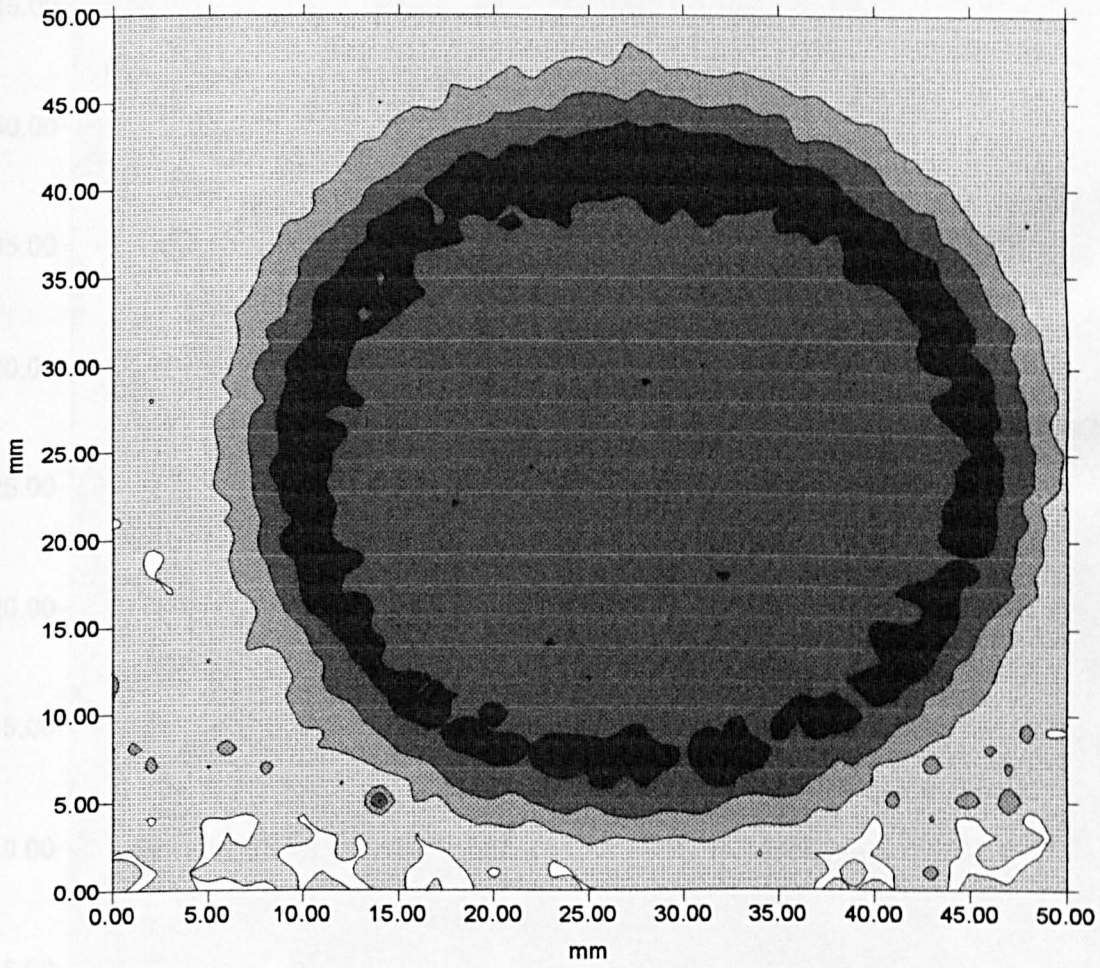

Figure 7.7(a). C-scan image of an imjection moulded green state ceramic disc, as received

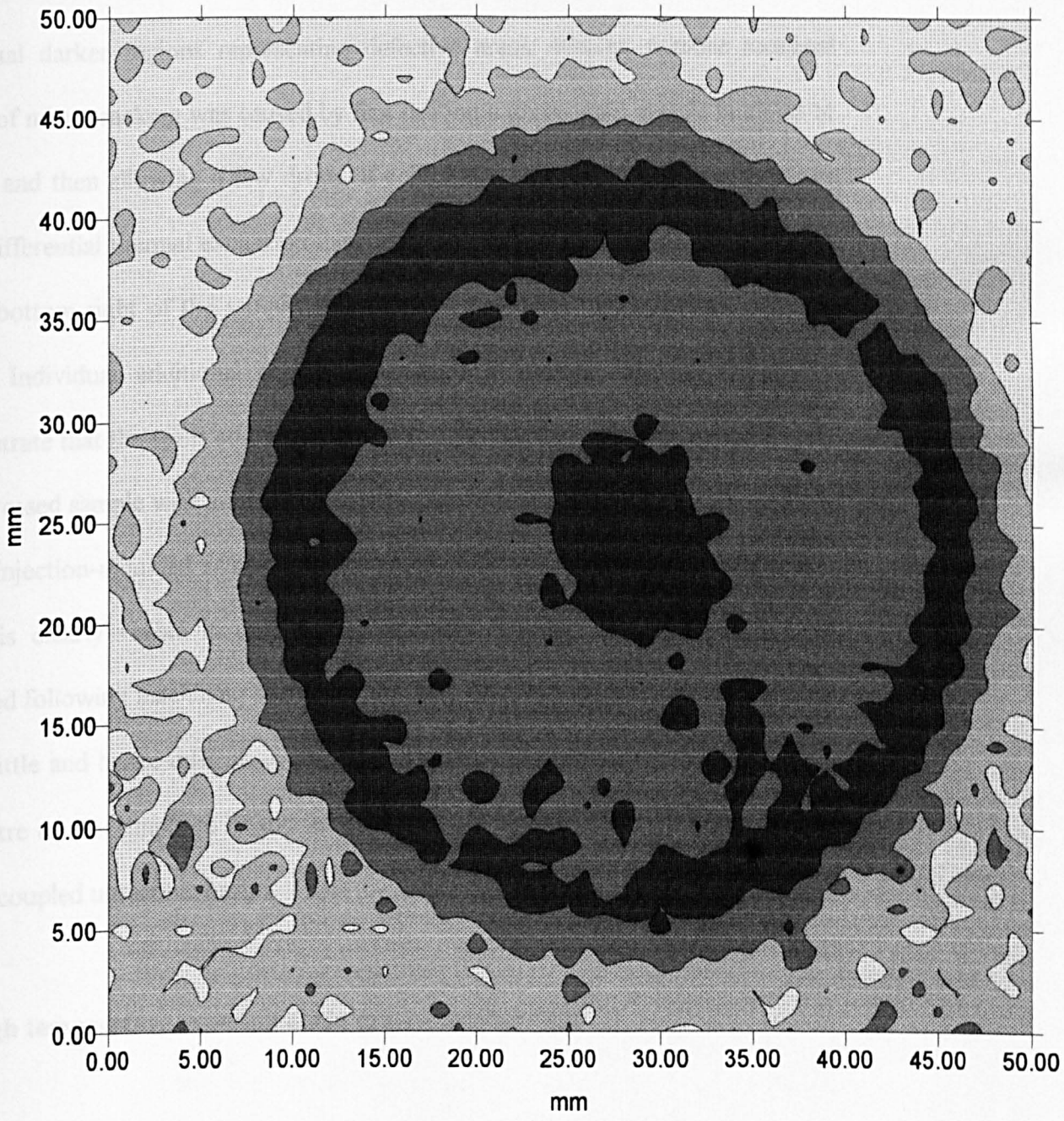

Figure 7.7 (b). C-scan image of an inection moulded green state ceramic sample, with a 5mm diameter, 1mm deep slot machined into the surface.

250°C in water. On inspection, this sample had a mixture of visible cracks, micocracking and delaminations. The resulting image is shown in Figure 7.7(c). A concentration of cracks is visible as an eliptical feature across the image, with individual darker regions representing defective areas. Finally, a more localised region of microcracking was caused by first heating a green-state sample in air up to 250°C, and then allowing a few drops of cold water to fall onto the centre of one face. Differential thermal expansion then caused a large crack to form, from the top left to bottom right of the sample, and this is clearly seen on the image of Figure 7.7(d). Individual additional regions of defect were not observed. Finally, to demonstrate that the scans could be performed on other types of sample, a C-scan of a die-pressed sample with a 5mm diameter recess in the centre, of similar dimensions to the injection-moulded samples, is presented in Figure 7.8. Again, the simulated defect is clearly visible in the image. Note that for this sample, cracking was observed following machining of the 5mm recess, as these samples in particular were very brittle and hence difficult to machine. This cracking, observed to radiate from the centre of the sample to its top left perimeter, is also evident as structure within the air-coupled ultrasonic image.

7.4 High temperature experiments in green-state ceramic

Typically, injection moulding green state ceramic (silicon nitride) samples are mixed with a thermoplastic polymer binder before injection and after moulding the binder is burnt out at elevated temperatures, before sintering is performed. For aerospace applications such as the production of ceramic turbine blades, where injection

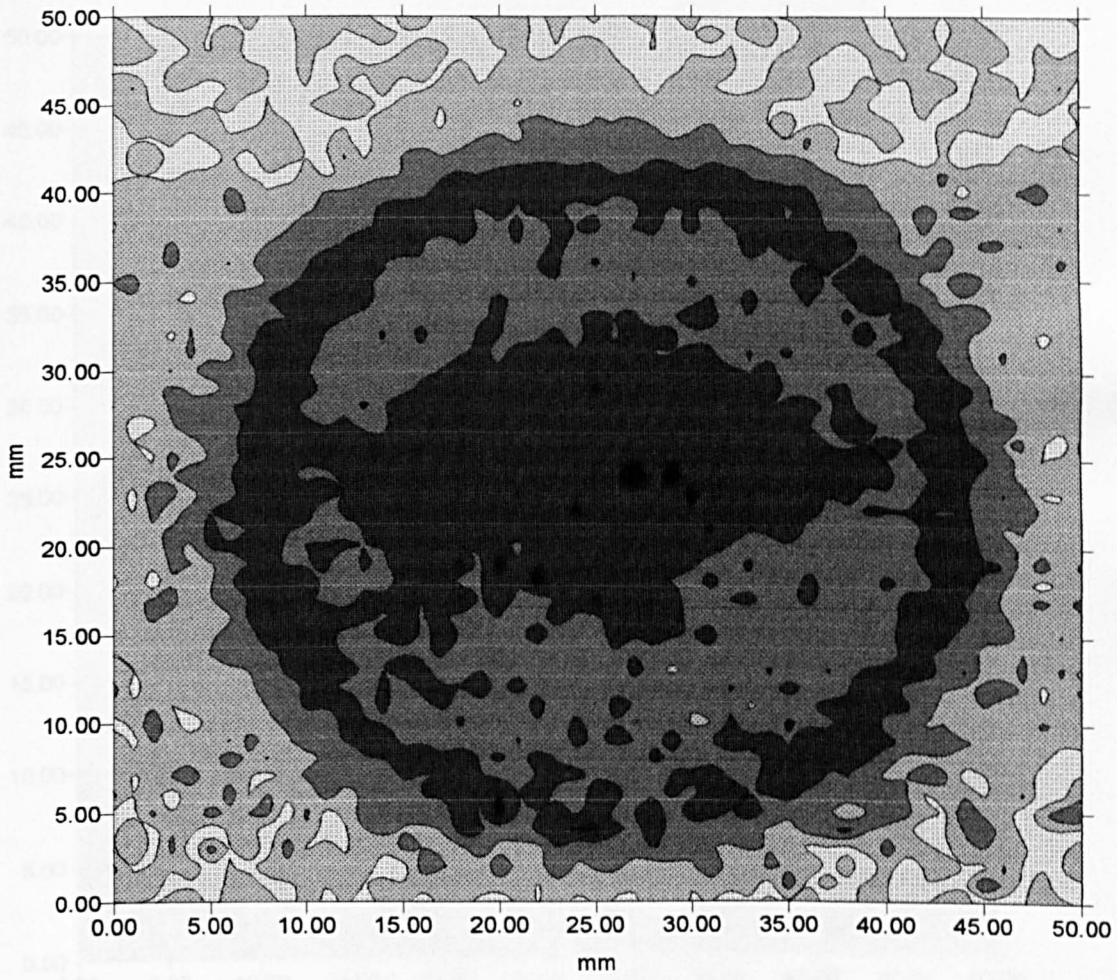

Figure 7.7(c). C-scan image of an imjection moulded green state ceramic disc, with cracks induced by cooling rapidly from high temperature.

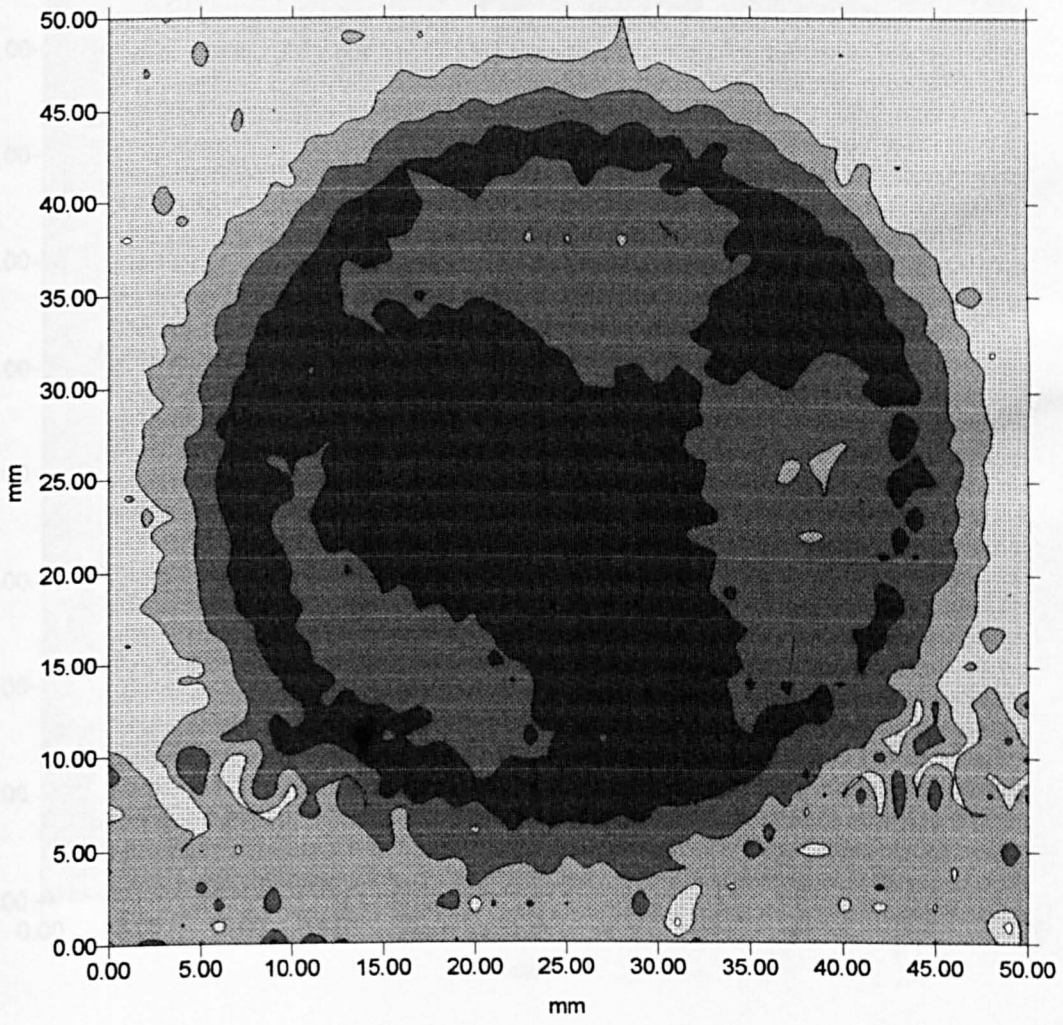

Figure7.7(d). C-scan image of an injection moulded green state ceramic sample, with cracks induced by radid cooling at the center region only.

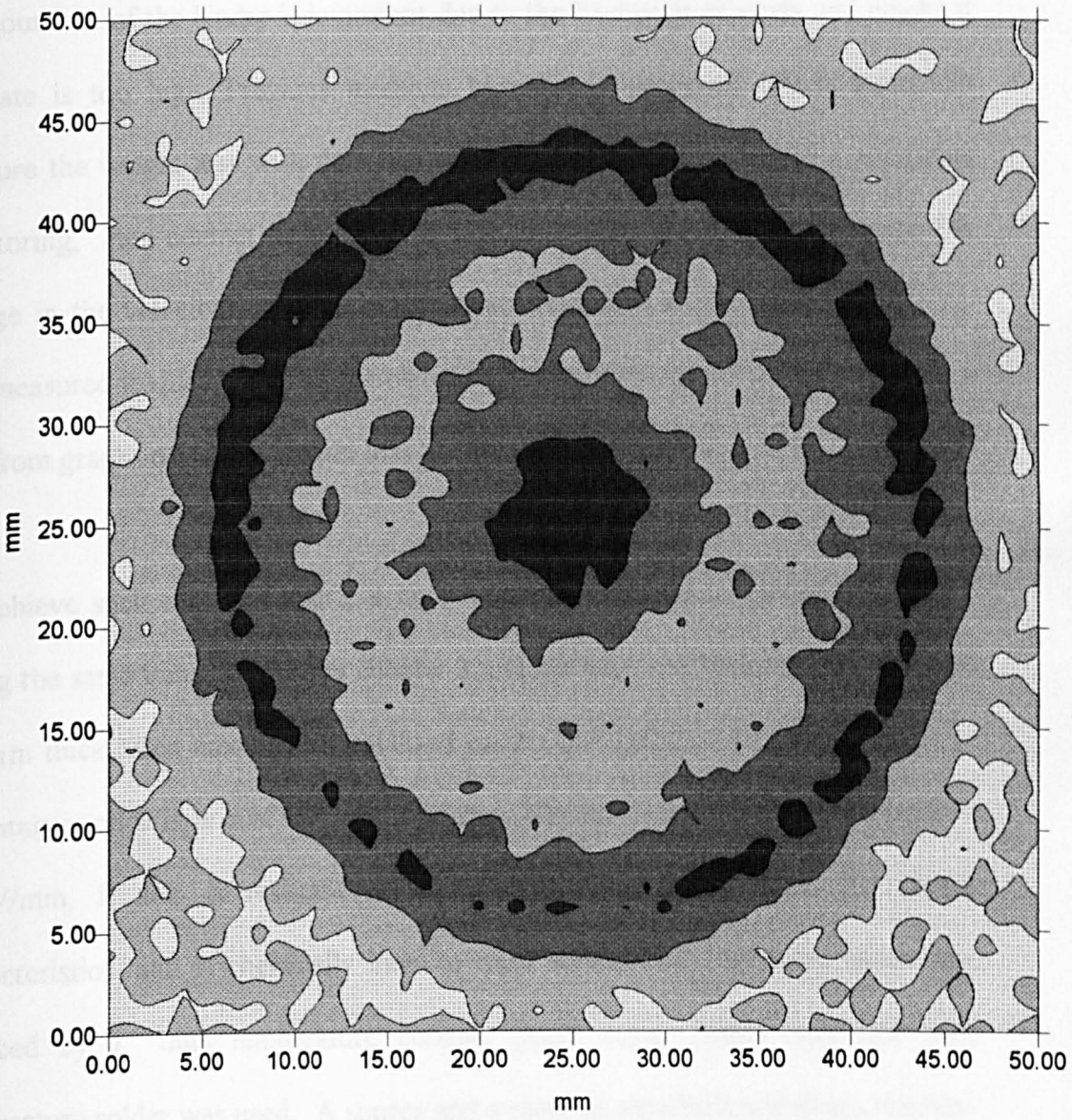

Figure 7.8. C-scan image of a 15 ton die-pressed green state ceramic sample, with a 5mm diameter, 1mm slot machined into the surface.

moulding is used for the complex shapes, much work has been reported on the fabrication process, including burn out of the polymer binder [12]. Monitoring the burn out rate of the binder is important due to the formation of voids and cracks if the rate is too high. Previous methods have been proposed which essentially measure the weight loss with time. An ideal solution would be to use a continous monitoring, non-contact air-coupled ultrasonic system which could measure the change in the velocity/frequency in through-transmission as the binder burns out. The measured frequency can be correlated to to a known amount of binder removed (i.e. from graphs of binder weight loss and transmitted frequency).

To achieve such a measurement, a high temperature transducer was designed by taking the same transducers as in chapter 3 and replacing the Mylar membrane with a 10μm thick Mica membrane (metalized on the top surface). This has a range of advantages: mica is one of the best insulators known, with a dielectric strength of 20KV/mm, It also is resistant to high temperatures (500-600°C), has stable characteristics, and is chemically inert to most substances. The nylon insert was replaced by a high temperature ceramic insert. Also, Telfon wire and high temperature solder was used. A source and a receiver were built which are identical in construction and when working together gave a bandwidth of about 300kHz, which was suitable for exciting through-thickness resonance frequency. A schematic diagram of the high temperature transducer is shown in Figure 7.9 and that of the experimental setup is shown in Figure 7.10. The measurements used a horizontal tube furnace, which could be programmed to perform temperature cycling. The ceramic samples were fixed rigidly in the furnace on one end of an arm which

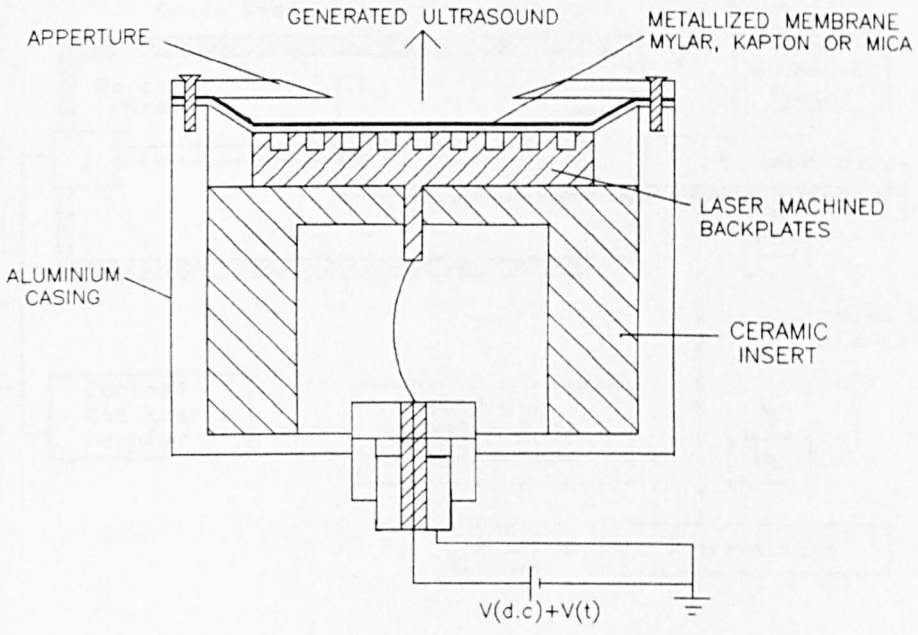

Figure 7.9. Schematic diagram of a high temperature Mica based capacitance transducer

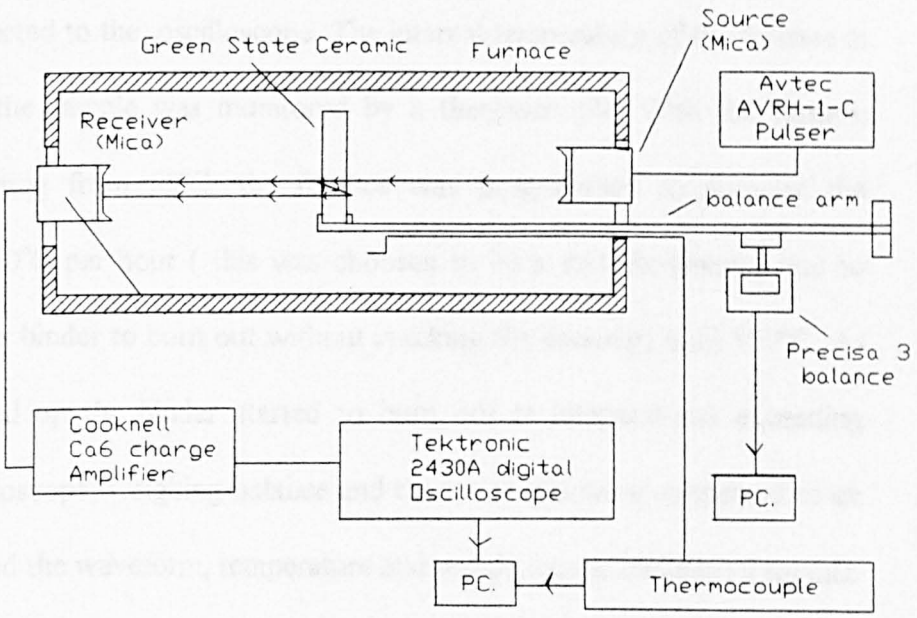

Figure 7.10. Experimental schematic diagam of the high temperature measurements in green state injection moulded ceramic.

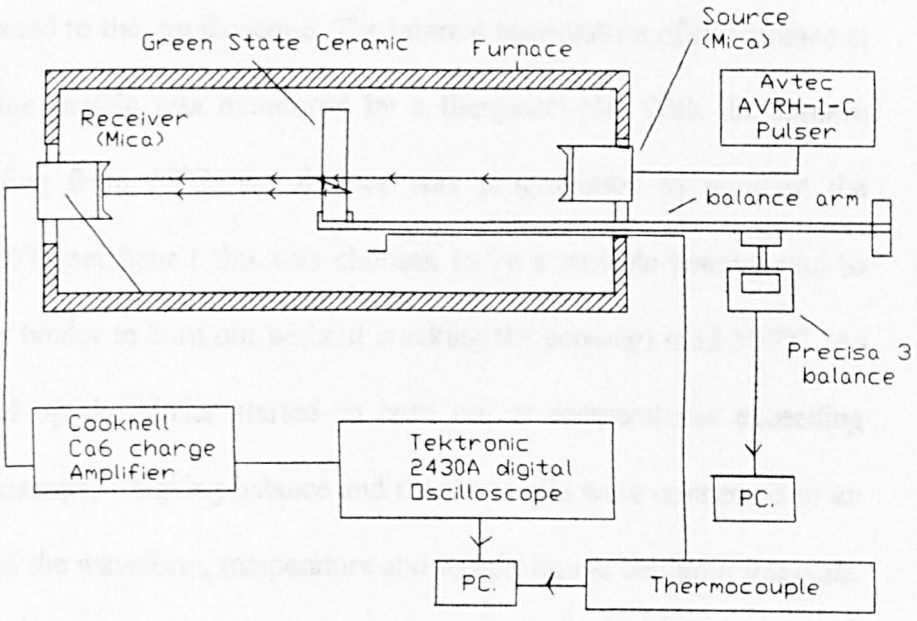

Figure 7.10. Experimental schematic diagam of the high temperature measurements in green state injection moulded ceramic.

extended from the furnace with counter balances on the other end. The arm was supported by a digital weighing balance. The transducers were positioned within the furnace on either side of the sample, to provide a through transmission arrangement. The ends of the furnace were insulated using fire wool to minimise the effects due to turbulence and temperature gradients along the furnace. Here, again, the source was driven by the pulser and the receiver was connected to the charge amplifier, which was connected to the oscilloscope. The internal temperature of the furnace at the position of the sample was monitored by a thermocouple. With the furnace temperature starting from 60°C, the furnace was programmed to increase the temperature by 10°C per hour (this was choosen to be a suitable heating rate to allow the polymer binder to burn out without cracking the ceramic) until 300°C. As the sample heated up the binder started to burn out at temperatures exceeding 120°C. The oscilloscope, weighing balance and thermocouple were connected to an PC which captured the waveform, temperature and weight loss at half hour intervals.

A through-transmitted waveform that was recorded at 120°C is shown in Figure 7.11, and it will be seen that the signal is of low amplitude, and complicated (because Mica is a stiff material). It is evident from Figure 7.11, that the first signal is a resonance corresponding to the signal that travelled through the sample. This is followed by a much larger signal, due to ultrasound that has travelled around the edge of the sample. The excellent through-transmitted resonant signal arises mainly because of the decreased acoustic velocity within the green-state ceramic once the binder has softened, decreasing the acoustic impedance of the sample to be more closely-matched to that of air, and hence increasing the transmission coefficient

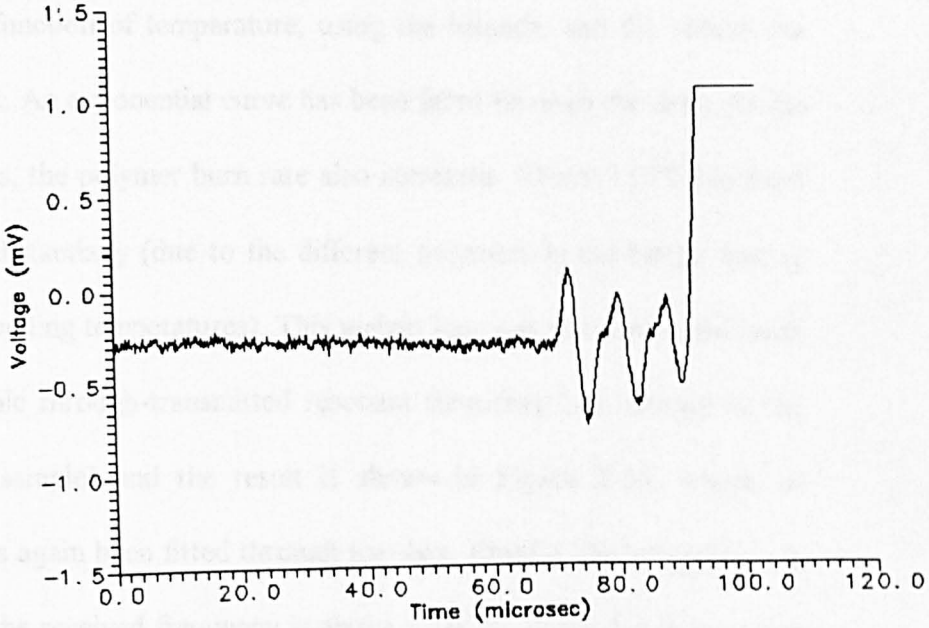

Figure 7.11. Received through-transmission at 120°C, through an injection moulded silicon nitride green state ceramic, using a Mica based capacitance transducer.

through the sample. It also has the effect of increasing the transit time across the sample thickness, reducing the frequency of the through-thickness resonance, and hence making the limited bandwidth of the capacitance transducers more useful for detecting individual multiple reflections.

A temperature run was conducted, in which the amount of polymer binder burnt out was measured as a function of temperature, using the balance, and the results are shown in Figure 7.12. An exponential curve has been fitted through the data. As the temperature increases, the polymer burn rate also increases. Above 150°C the burn out rate increases substantially (due to the different polymers in the binder having varying melting and boiling temperatures). This weight loss was now correlated with the received ultrasonic through-transmitted resonant frequency (i.e. change in the velocity within the sample) and the result is shown in Figure 7.13, where an exponential curve has again been fitted through the data. Clearly, the weight loss is insignificant in significant when the received frequency is above 170kHz. From this data, it can thus be stated that with a thickness of 3mm, the amount of binder burnt out can be determined by measuring the velocity / frequency within the sample, using a non-contact air-coupled ultrasonic method. Although the experiment was performed on a injection moulded silicon nitride sample, the method could be extended for any other green sate ceramic. By producing series of graphs as in Figure 7.13 for a particular green state ceramic, and having a system of high temperature air-coupled capacitance transducers to monitor the resonant frequency of the sample, the burn out rate could easily be monitored, without disturbing the ceramic during sintering.

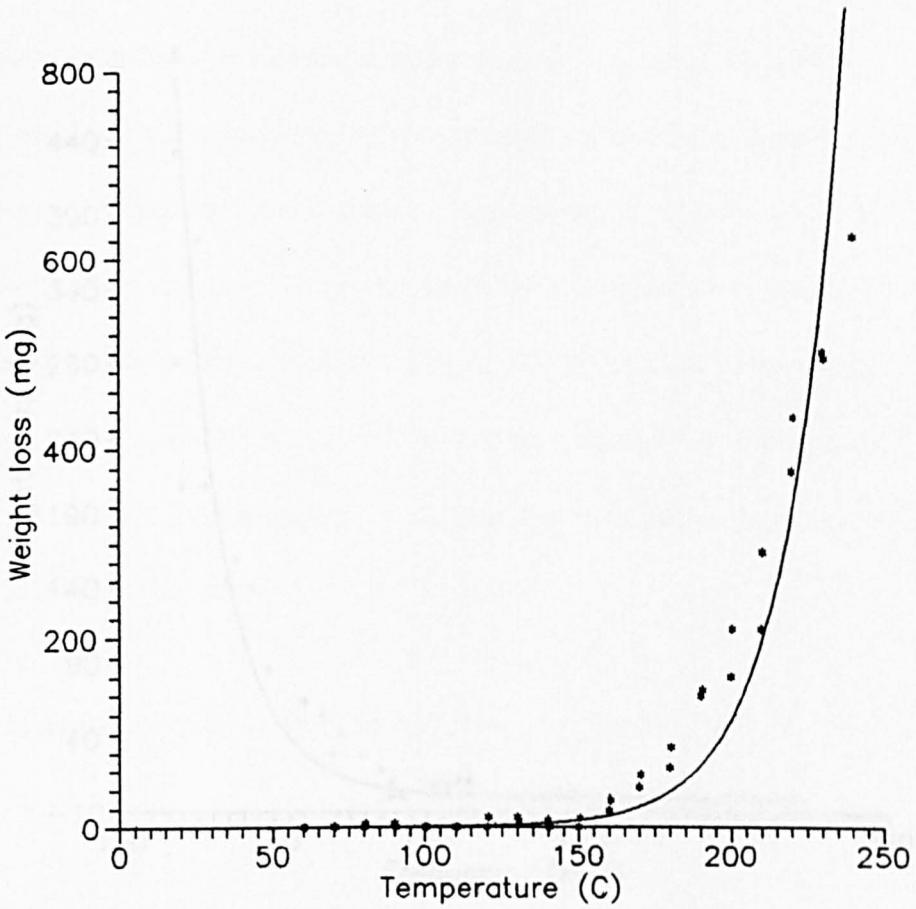

Figure 7.12. Binder loss as a function of temperature for a silicon nitride green state ceramic.

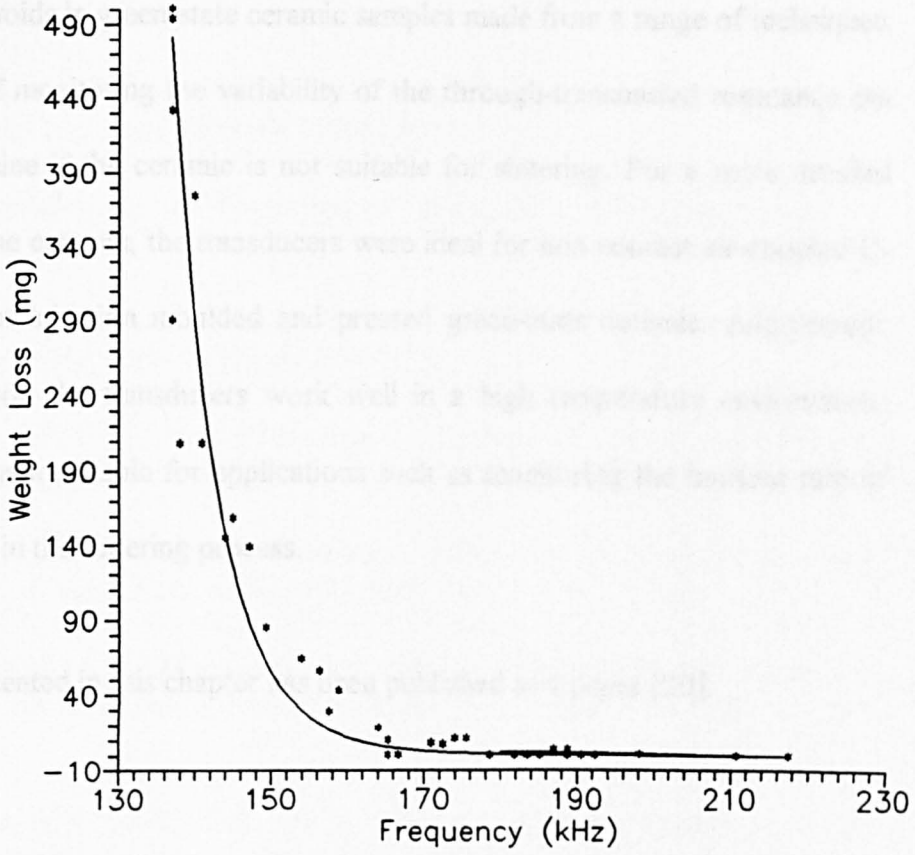

Figure 7.13. Binder loss as a function of the received frquency for a silicon nitride injection moulded green state ceramic.

7.5 Conclusions

Capacitance transducers have been shown to be able to detect possible defects such as cracks and voids in green-state ceramic samples made from a range of techniques. The method of monitoring the variability of the through-transmitted resonance can quickly determine if the ceramic is not suitable for sintering. For a more detailed inspection of the ceramic, the transducers were ideal for non contact air-coupled C-scan imaging of injection moulded and pressed green-state ceramic. Additionally, with modification the transducers work well in a high temperature environment, which makes them suitable for applications such as monitoring the burnout rate of polymer binder in the sintering process.

The results presented in this chapter has been published as a paper [20].

7.6 References

[1]. F.M. Tiller and C.D. Tsai, "Theory of filtration of ceramics" *J. Amer. Ceram. Soc.* **69** (1986) 882.

[2] T. Nonaka, Y. Hayakawa, S. Takeda and N. Nishimori, " Ultrasonic-imaging systems for composites and ceramic", *Mater. Eval.* **47** (1989) 542.

[3]. J.J. Gruber, J.M. Smith and R.H. Brockelman, " Ultrasonic velocity C-scans for ceramic and composite materials" *Mater. Eval.* **46** (1988) 90.

[4]. G. Zeigler, J. Heinrich and G. Wotting, "Relationship between processing microstructure and properties of dense and reaction-bonded silicon nitride" *J. Mater. Sci.* **22** (1987) 3041.

[5]. R.A. Roberts, "A dry-contact coupling technique for ultrasonic non-destructive evaluation of green state ceramics", *Mater. Eval.* **46** (1988) 758.

[6]. K. Yamanaka, C.K. Jen, C. Neron and J.F. Bussiere, " Improved ultrasonic evaluation of green-state ceramic with the use of a surface bonded adhesive tape", *Mater. Eval.* **47** (1989) 828.

[7]. W.M.D. Wright, D.A. Hutchins and M.H. Lewis, " Ultrasonic imaging of a silicon nitride ceramic before and after firing", *J. Mater. Sci. Lett.* **14** (1995) 366.

[8]. A.J. Rogovsky, " Development and application of ultrasonic dry-contact and air-contact C-scan systems for non-destructive evaluation of aerospace composites", *Mater. Eval.* **49** (1991) 1491.

[9]. K.L. Telshow, J.B. Walter and G.V. Garcia, " Laser ultrasonic monitoring of veramic sintering", *J. Appl. Phys.* **68** (1990) 6077.

[10]. J.P. Monchalin, Optical - detection of ultrasound", *IEEE Trans UFFC*, **33** (1986) 485.

[11]. H.M. Frost, Physical Acoustics **14** (W.P Mason and R.N. Thurston, eds, Acadamic Press, New York, 1979), pp 179-275.

[12]. T.Zhang, J.R.G. Evans, " Predicting the incidence of Voids in the injection moulding of thick ceramic sections", *J. Am. Ceram. Soc.* **76** (1993) 481.

[13]. T. Zhang, J.R.G. Evans, " Relaxation effects in large injection-moulded ceramic bodies", *J. Euro. Ceram. Soc.* **12** (1993) 51.

[14]. S.T. Schwab, C.R. Blanchard, R.C. Graff, "The influence of preceramic binders on the microstructural development of silicon-nitride", *J. Mat. Sci.* **29** (1994) 6320.

[15]. J.A. Lewis, M.J. Cima, W.E. Rhine, " Direct observation of preceramic and organic binder decomposition in 2-D model microstructures", *J. Am. Ceram. Soc.* **77** (1994) 1839.

[16]. D.A. Hutchins, W. M. D. Wright and D. W. Schindel, " Ultrasonic measurements in polymeric materials using air-coupled capacitance transducers", *J. Acoustic. Soc. Am.* **96** (1994) 1634.

[17]. B. Hosten, D. A. Hutchins and D. W. Schindel, " Measurement of elastic-constants in composite material using air-coupled ultrasonic bulk waves", *J. Acoust. Soc. Am.* **99** (1996) 2116

[18]. D.W. Schindel, D. A. Hutchins and W. Grandia, "Capacitive and piezoelectric air-coupled transducers for resonant ultrasonic inspection", *Ultrasonics* **34** (1996) 621.

[19]. D.W. Schindel and D. A. Hutchins, " Through thickness characterization of micromachined air-coupled capacitive transducers", *Ultrasonics* **33** (1995) 11.

[20] A.G.Bashford and D.A. Hutchins, "Air-Coupled ultrasonic transducers for measurement of green-state ceramic at elevated temperatures", *Proc. IEE.* (submitted).

CHAPTER 8

CONCLUSIONS AND FURTHER WORK

This thesis offers additional knowledge in the design and characterisation of micromachined air-coupled ultrasonic transducers, and with further modification, the transducers have been used in a variety of new and novel applications such as characterising materials, immersion testing, and high temperature measurements. Additionally other methods presented for NDE applications including laser-EMAT ultrasonic testing, and capacitance and strain gauge measurement.

Chapter 3 demonstrated how the characteristics of a micromachined air-coupled capacitance transducer can be controlled by the geometry of the holes machined into the backplate. Backplates were produced in either silicon or metal (copper and steel), which were chemical etched, ion beam and laser machined. The various techniques produced varying hole definition and surface finish, and were shown to have a large effect on the resonant frequency of the device when tested as a source in air. Typically, the chemical etched backplates produced rounded hole edges and rougher surface finish as compared to the ion-beam and laser machined backplates. Additionally, there was not a significant difference between using silicon or metal for the backplate (metal backplates generally require polishing but do not need to have an electrode placed on the surface). Laser machining in both metal and silicon produced well defined holes, good surface finish and the ability to vary the dimensions of the holes quickly and also are inexpensive to produce. With further testing using a Fabry-Perot interferometer the dimensions of the holes were found to affect the characteristics of the transducers. Typically, it was found

that the polished areas of the backplate contributed to the overall higher frequency characteristics, whereas the holes provide the lower frequency characteristics. Additionally, for shallow and small diameter holes, a large pitch provided an increased resonant frequency, with a reduced signal amplitude.

Chapter 4 demonstrates that micromachined air-coupled capacitance transducers show many of the characteristics of a plane piston radiator for both transient and toneburst excitation. Predictions of a theoretical model (which included frequency-dependent attenuation), had good agreement with the experimental peak pressure field variations. Also, with further modification to the aperture (use of an annulus and a zoneplate), the nature of the peak pressure field was altered to aid focusing between 300-800kHz. This covers much of the useful frequency range in air-coupled ultrasonics. Again, theoretical predictions of the peak pressure field for the modified apertures were made, which also agreed well with the experimental pressure field.

Chapter 5 dealt with the immersion of the micromachined capacitance transducers in water. Again, as with chapter 4, the same driving signals (i.e. transient and a toneburst) were applied. As compared to the theory for a plane piston, the agreement between the experimental peak pressure field and the theoretical field was good. Also, with the same aperture modifications as in chapter 4, there was reasonable agreement between the experimental and theoretical peak pressure fields. Additionally, with the significant increase in the bandwidth and resonant frequency (due to reduced attenuation in water of the higher frequencies) the transducers were shown to be useful for immersed pulse-echo imaging. Thus, the capacitance transducers have been shown be able to perform the same applications as with conventional piezo-electric based transducers, using the same pulsers and amplifiers. However, further investigation is needed to

improve the water resistance of the transducers for stable long term operation. This might involve coating the polymers, or using other membrane materials.

Chapter 6 demonstrated that micromachined capacitance transducers could be substituted for conventional piezo-electric immersion transducers to characterise materials in air by measuring the velocity of the quasi-longitudinal and quasi-shear modes as a function of angle, and thus obtaining a value for the elastic constants of the material. This used an established experimental system. Furthermore, a large diameter transducer of 50mm which more closely approximated the transducer to a plane wave source, was successfully used in through-transmission, to determine the transmission coefficient of cardboard. The transducers were successfully used for porous materials in air, which would be damaged if immersed in water.

Chapter 7 extended the design of the transducers to high temperature applications. Also studied was through-transmission, non-contact imaging of artificial defects in green state silicon nitride ceramics in air which had been were prepared by various techniques. With the use of high a high temperature mica membrane, the transducers were used at temperatures of up to 240°C, whilst maintaining the necessary bandwidth and amplitude to monitor the polymer binder burnout rate from an injection moulded green state ceramic sample. With further development, such as obtaining thinner mica membranes the signal amplitude and bandwidth of the traducers could increased significantly which would extend the technique to the possibility of performing NDE in hot environments (i.e. hot flow rate measurement in gas-filled pipes, for instance).

Finally, chapter 8 demonstrated the use of other new NDE measurements, some of which were based on capacitance techniques. The laser-EMAT and the capacitance gauge measurement

were in good agreement for the transition temperature, used to determine hydrogen content in zirconium. This was further supported by the strain gauge measurement, although strain gauges were limited to below 300°C. These techniques are ideal for continuous in service monitoring, and demonstrate further the usefulness of non-contact techniques for materials characterisation measurements.

APPENDIX 1

Equipment Specification

Avtec AVRII-1-C pulser

Output: 0-1KV positive square wave

Pulse width: 0-5μs

Cooknell CA/6C charge amplifier

Sensitivity: 5mv/Pc

Bias Voltage: 0-100V

Precision Acoustics minature hydrophone

Bandwidth: 0-40 MHz

Sensitivity: Not calibrated.

Computer controlled scanning stages

Two linear stages: Fitted with synchronous stepping motor

Motors: 400 steps per revolution

Accuracy of the system: ± 0.004mm / 50mm of travel

APPENDIX 2

PROGRAM LISTING FOR THE THEORETICAL PRESSURE FIELD VARIATION OF A PLANE PISTON TRANSDUCER.

```
00001 C      THE FOLOWING PROGRAM COMPUTES THE PEAK PRESSURE FIELD VARIATIONS
00002 C      FOR A PLANE PISTON TRANSDUCER OF ANY DIAMETER WITH EITHER A SINGL
00003 C      OR TONEBURST EXCITATION.

00004-
00005
00006
00007         PROGRAM ANDYCONV
00008         IMPLICIT NONE
00009
00010
00011         CHARACTER*20 MAX
00012         INTEGER It,UN
00013         REAL Mt(4096),Tt(4096),Bt(4096),Yt(4096),Ft,Jt,FR,Et(4096)
00014         INTEGER NMAX,NMAX2,NW,I,N,NP,NF,A
00015         REAL DT,XI,EI,AZ,Mtt(2048)
00016         PARAMETER(NMAX=4096)
00017         PARAMETER(NMAX2=4096)
00018         REAL F(NMAX2),V1
00019         REAL W(NMAX2)
00020         REAL Y(NMAX2)
00021         COMPLEX CONV(2*NMAX2)
00022         COMPLEX CF(2*NMAX2)
00023         COMPLEX CW(2*NMAX2)
00024         COMPLEX CY(2*NMAX2)
00025
00026         CHARACTER*20 FAME
00027         CHARACTER*20 GAME
00028         CHARACTER*20 FAME1
00029
00030
00031         REAL WJ,TJ,YJ(4096),U11,U22,U33,U44,U55,U66,U1,U2,U3,U4,U5,U6
00032         INTEGER MJ,OJ,PW
00033
00034
00035         REAL E,C,O,X,Z,D,R,S,T,T1,T2,T0,QW,CV1,C1,OP,FRR
00036         INTEGER B,G,L,CV
00037         REAL Q(4096),P(4096)
00038         CHARACTER*100 NAME
00039
00040 C     THE INTERVAL SHOULD BE THE SAME AS THE DATA IN THE FILE 'SINA'
00041
00042       QW=2E-8
00043
00044 C     INPUT DATA: SOUND VEL, DIAMETER, FIELD DIMENSIONS, NUMBER OF POINTS
00045
00046       PRINT*, 'INPUT THE SOUND VELOCITY  M/Sec   '
00047
00048       READ*, C
00049       C1=C
00050
00051
00052       PRINT*, ' DIAMETER OF THE APPERTURE (MM)  '
```

```
00053         READ*, OP
00054         O=OP/2000
00055
00056
00057         A=0
00058         L=0
00059         G=0
00060         CV=0
00061
00062         PRINT*, 'THE NUMBER OF POINTS IN THE INPUT WAVEFORM (SINA)  '
00063         READ*, MJ
00064
00065         PRINT*, 'THE FREQUENCY OF THE INPUT WAVEFORM (SINA) MHz '
00066         READ*, FRR
00067         FR=FR*1000000
00068
00069         PRINT*, 'STARTING RADIAL POSITION (MM) '
00070         READ*, U11
00071         U1=U11/1000
00072
00073         PRINT*, 'FINISHING RADIAL POSITION (MM) '
00074         READ*, U22
00075         U2=U22/1000
00076
00077         PRINT*, 'RADIAL INTERVAL (MM) '
00078         READ*, U33
00079         U3=U33/1000
00080
00081         PRINT*, 'STARTING AXIAL POSITION  (MM) '
00082         READ*, U44
00083         U4=U44/1000
00084
00085         PRINT*, 'FINISHING AXIAL POSITION (MM) '
00086         READ*, U55
00087         U5=U55/1000
00088
00089         PRINT*, 'AXIAL INTERVAL (MM) '
00090         READ*, U66
00091         U6=U66/1000
00092
00093         OPEN (UNIT=2,FILE='OUT.DAT', STATUS='NEW')
00094         FAME1='SINA'
00095
00096         OPEN(UNIT=3,FILE=FAME1,STATUS='OLD')
00097           DO 20 I=1,MJ
00098             READ(3,*) XI,F(I)
00099 *           PRINT*, F(I)
00100  20       CONTINUE
00101           CLOSE(3)
00102
00103
00104         UN=1
00105
```

```
00106 C     CALCULATE THE WAVEFORM AT EACH POSITION 'X' RADIAL, 'Z' AXIAL DISTA
00107 C     BY CONVOLVING THE SIMULATED SIGNAL (SINA) WITH THE IMPULSE RESPONSE
00108
00109       DO 19 X=U1,U2,U3
00110       DO 18 Z=U4,U5,U6
00111
00112 C       SETTING THE VARIABLES TO BE COMPLEX FOR THE CONVOLUTION
00113
00114         DO 3 I=1,NMAX2
00115         W(I)=0.0
00116         CW(I)=CMPLX(0.0,0.0)
00117         CW(NMAX2+I)=CMPLX(0.0,0.0)
00118         CF(I)=CMPLX(0.0,0.0)
00119         CF(NMAX2+I)=CMPLX(0.0,0.0)
00120         CY(I)=CMPLX(0.0,0.0)
00121         CY(NMAX2+I)=CMPLX(0.0,0.0)
00122         CONV(I)=CMPLX(0.0,0.0)
00123   3     CONTINUE
00124
00125       I=0
00126       Mtt(I)=0
00127
00128       I=1
00129
00130       T0 = Z/C1
00131       T1 = (SQRT((O-ABS(X)) * (O-ABS(X)) + Z**2))/C1
00132       T2 = (SQRT((O+ABS(X)) * (O+ABS(X)) + Z**2))/C1
00133
00134
00135
00136       IF (ABS(X).GT.O) THEN
00137       C=0
00138       ENDIF
00139
00140 *     OPEN (UNIT=2,FILE='ANDY',STATUS='NEW')
00141
00142
00143       DO 15 T=T0-2E-6,T0+15E-6,QW
00144
00145 C     CALCULATE THE IMPULSE RESPONSE AND SET THE BOUNDARY CONDITIONS
00146
00147       IF (T.LE.T0) THEN
00148       P(I)=0
00149       ENDIF
00150       IF (T.GT.T0.AND.T.LE.T1) THEN
00151       P(I)=C *1000
00152       ENDIF
00153       IF (T.GT.T1.AND.T.LE.T2) THEN
00154
00155
00156       D= (((C1*T)**2)-(Z*Z)+(ABS(X)*ABS(X))-(O*O))
00157       E = (SQRT(((C1*T)**2) - (Z*Z)))*ABS(X)*2
00158       R = D/E
```

```
00159         S = (1000*C1/3.14)*ACOS(R)
00160         P(I)=S
00161
00162         ENDIF
00163
00164         IF (T.GT.T2) THEN
00165         P(I)=0
00166
00167         ENDIF
00168
00169         IF (ABS(X).EQ.O) THEN
00170         P(I)= S/2
00171         ENDIF
00172
00173
00174
00175         W(I)=(P(I)-P(I-1))/QW
00176
00177
00178
00179
00180
00181 *       PRINT*,P(I)
00182 *       WRITE(2,*) T,W(I)
00183
00184         I = I+1
00185 15      CONTINUE
00186 *        PRINT*,I
00187 *        CLOSE(2)
00188
00189 C       CONVOLVING THE SIMULATED SIGNAL AND THE IMPULSE RESPONSE
00190
00191           NW=I-1
00192           DT=QW
00193           NF=MJ
00194             I=0
00195
00196           N=NF+NW-1
00197           NP=2*NMAX2
00198           DO 30 I=1,20
00199             IF(NP/2.LT.N) GOTO 40
00200             NP=NP/2
00201  30       CONTINUE
00202  40       CONTINUE
00203
00204
00205           DO 50 I=1,NF
00206             CF(I)=CMPLX(F(I),0.)
00207
00208  50       CONTINUE
00209           DO 60 I=1,NW
00210             CW(I)=CMPLX(W(I),0.)
00211
```

```
00212  60      CONTINUE
00213           I=1
00214
00215
00216           I=I+1
00217 61        CONTINUE
00218 *         CLOSE (1)
00219           I=0
00220           CALL FOUR1(CF,NP,1)
00221           CALL FOUR1(CW,NP,1)
00222
00223 C       MODIFY THE WAVEFORM TO INCLUDE ATTENUATION  AT FREQUENCY 'FR'
00224 C       AND AXIAL DISTANCE Z
00225
00226           DO 70 I=1,NP
00227
00228            AZ=15.895E-11*FR*FR
00229            CV1= (10**(AZ * Z / 20))
00230
00231           CONV(I)=CF(I)*CW(I) / CV1
00232
00233 *          CONV(I)=CF(I)*CW(I)
00234 *         PRINT*, CF(I), CV1
00235
00236
00237
00238  70       CONTINUE
00239
00240 C       RETURN THE CONVOLUTION BACK TO A TIME DOMAIN WAVEFORM
00241
00242           CALL FOUR1(CONV,NP,-1)
00243
00244 C
00245
00246 *           OPEN(UNIT=1,FILE='RES',STATUS='NEW')
00247            DO 80 I=1,N
00248            Tt(I)= FLOAT(I)*DT
00249            Mt(I)=REAL(CONV(I))/FLOAT(NP)
00250
00251
00252 *           PRINT*, Tt(I),Mt(I)
00253 *            WRITE(1,*) Tt(I), Mt(I)
00254
00255 80         CONTINUE
00256
00257 *           CLOSE(1)
00258
00259
00260 C       FIND THE PEAK TO PEAK AMPLITUDE OF THE WAVEFORM (PROPORTIONAL TO F
00261
00262
00263           Jt=0
00264           Ft=0
```

```
00265          Bt(I)=0
00266          DO 503 I=1,NW+NF-1,1
00267
00268
00269
00270          IF (Mt(I).GT.Ft) THEN
00271
00272
00273          Ft=Mt(I)
00274          ENDIF
00275          IF (Mt(I).LT.Jt) THEN
00276          Jt=Mt(I)
00277          ENDIF
00278
00279 503     CONTINUE
00280           Et(UN)=(Ft-Jt) / 1E10
00281 C      WRITE THE RESULTS TO THE FILE (OUT.DAT)
00282
00283        WRITE (2,*) X,Z,Et(UN)
00284        PRINT*, X,Z,Et(UN)
00285
00286        UN=UN+1
00287
00288
00289  18      CONTINUE
00290  19      CONTINUE
00291
00292        CLOSE (UNIT=2)
00293        STOP
00294          END

UMBER OF WARNINGS IN PROGRAM UNIT: 0
UMBER OF ERRORS   IN PROGRAM UNIT: 0

00295 CCCCCCCCCCCCCCCCCCCCCCCCCCCCCCCCCCCCCCCCCCCCCCCCCCCCCCCCCCCCCCCCCCCC
00296 C      CONVOLUTION SUBROUTINE
00297
00298        SUBROUTINE FOUR1(DATA,NN,ISIGN)
00299        REAL*8 WR,WI,WPR,WPI,WTEMP,THETA
00300        DIMENSION DATA(*)
00301        N=2*NN
00302        J=1
00303        DO 11 I=1,N,2
00304          IF(J.GT.I)THEN
00305            TEMPR=DATA(J)
00306            TEMPI=DATA(J+1)
00307            DATA(J)=DATA(I)
00308            DATA(J+1)=DATA(I+1)
00309            DATA(I)=TEMPR
00310            DATA(I+1)=TEMPI
00311          ENDIF
00312          M=N/2
00313 1        IF ((M.GE.2).AND.(J.GT.M)) THEN
```

```
00314             J=J-M
00315             M=M/2
00316           GO TO 1
00317           ENDIF
00318           J=J+M
00319 11      CONTINUE
00320         MMAX=2
00321 2       IF (N.GT.MMAX) THEN
00322           ISTEP=2*MMAX
00323           THETA=6.28318530717959D0/(ISIGN*MMAX)
00324           WPR=-2.D0*DSIN(0.5D0*THETA)**2
00325           WPI=DSIN(THETA)
00326           WR=1.D0
00327           WI=0.D0
00328           DO 13 M=1,MMAX,2
00329             DO 12 I=M,N,ISTEP
00330               J=I+MMAX
00331               TEMPR=SNGL(WR)*DATA(J)-SNGL(WI)*DATA(J+1)
00332               TEMPI=SNGL(WR)*DATA(J+1)+SNGL(WI)*DATA(J)
00333               DATA(J)=DATA(I)-TEMPR
00334               DATA(J+1)=DATA(I+1)-TEMPI
00335               DATA(I)=DATA(I)+TEMPR
00336               DATA(I+1)=DATA(I+1)+TEMPI
00337 12          CONTINUE
00338             WTEMP=WR
00339             WR=WR*WPR-WI*WPI+WR
00340             WI=WI*WPR+WTEMP*WPI+WI
00341 13        CONTINUE
00342           MMAX=ISTEP
00343         GO TO 2
00344         ENDIF
00345         RETURN
00346
00347
00348
00349
00350
00351
00352
00353         END
```

```
UMBER OF WARNINGS IN PROGRAM UNIT: 0
UMBER OF ERRORS   IN PROGRAM UNIT: 0

UMBER OF WARNINGS IN COMPILATION : 0
UMBER OF ERRORS   IN COMPILATION : 0
```

PUBLICATIONS AND CONFERENCES

Publications

1. D.A. Hutchins, A.G. Bashford, M.D.C Moles, and H.D. Mair, 'Temperature dependent NDE of zirconium alloy tubing' Insight **38**, 102-107 (1996).

2. A.G. Bashford, D.A. Hutchins, D.R. Billson, H.D. Mair and M.D.C. Moles, 'High temperature non-destructive evaluation of hydrided metal tubing', Proc 1994 QNDE Conf. (Colorado, USA), Vol 14B 1399-1406 (1995).

3. A.G. Bashford, D.A. Hutchins and D.W. Schindel 'The response of an air-coupled ultrasonic transducer for various backplates and apertures', Proc. 1995, QNDE Conf. (Seattle, USA), *in press.* (1996).

4. A.G. Bashford, D.A. Hutchins and D.W. Schindel 'Radiated fields of an air-coupled ultrasonic transducer', Ultrasonics **34**, 169-172 (1996).

5. D.A. Hutchins, A.G. Bashford, W.M.D. Wright and D.W. Schindel 'Advances in wide bandwidth air-coupled capacitance transducer' Proc. 1995 IEEE Ultrasonics symposium (Seattle, USA), 981-984.

6. A.G. Bashford, D.W. Schindel, D.A. Hutchins and W.M.D. Wright, 'Field characterisation of an air-coupled micromachined ultrasonic capacitance transducer', J. Acoust. Soc. Am. **101** (6), 315-322 (1997).

7. A.G. Bashford, D.W. Schindel, and D.A. Hutchins 'Characteristics of Ultrasonic Micromachined Capacitance Transducers in Water' Proc. 1996 IEEE Ultrasonics symposium (San Antonio, USA), 955-958.

8, A.G. Bashford, D.W. Schindel and D.A. Hutchins, "Micromachined ultrasonic capacitance transducers for immersion applications", *IEEE, Trans. Ultra. Ferro. Freq. Cont.*, **45 (2),** 367-375, (1998).

9. A.G. Bashford, D.W. Schindel and D.A. Hutchins 'Micromachined Ultrasonic Capacitance Immersion transducers' IEEE Transactions, *in press.*

10. D.W. Schindel, A.G. Bashford, D.A. Hutchins 'Focussing of ultrasonic waves in air using a micromachined Fresnel zone plate", *Ultrasonics* **35**, 275-286 (1997).

11. A.G. Bashford and D.A. Hutchins ' New Mica based capacitance immersion transducers' J. Acoust, Soc, Am, Abstract, Joint ASA & JSA meeting, (Wikiki, Hawaii, USA December 1996) 2730.